CRUSTAL STRUCTURE OF THE ISPARTA ANGLE AND SURROUNDING REGIONS USING P-RECEIVER FUNCTION ANALYSIS

by

Metin Kahraman

B.S., Geophysical Engineering, İstanbul University, 2004

Submitted to the Kandilli Observatory and Earthquake
Research Institute in partial fulfillment of
the requirements for the degree of
Master of Science

Graduate Program in Geophysics Department

Boğaziçi University

2008

CRUSTAL STRUCTURE OF THE ISPARTA ANGLE AND
SURROUNDING REGIONS USING
P-RECEIVER FUNCTION ANALYSIS

APPROVED BY:

Prof. Niyazi Türkelli (Thesis Supervisor)	. . . . .
Prof. Ali Pınar	. . . . .
Assoc. Prof. Nurcan Özel	. . . . .

DATE OF APPROVAL: 15.August.2008

This Thesis is dedicated to my family.

ACKNOWLEDGEMENTS

I would like to thank Professor Niyazi Turkelli for his guidance, enlightening support and useful suggestions during my thesis. I would not able to complete this study without his help.

I also would like to thank Rengin Gök for providing me the joint inversion and H-K stacking codes and practical scripts. I am grateful to Michael Pasyanos for sharing his surface wave data with me. I am appreciated to Robert Mellors for supporting useful scripts with me.

Also, I would like thank my friends at B.U. Kandilli Observatory and Earthquake Research Institute: Department of Geophysics for supporting me their help whenever I need.

I would like to acknowledge my family who never left me alone when I come across a difficulty.

This research is supported by Bogaziçi University Research Fund (Grant No. 07T203).

ABSTRACT

CRUSTAL STRUCTURE OF THE ISPARTA ANGLE AND SURROUNDING REGIONS USING P-RECEIVER FUNCTION ANALYSIS

Isparta Angle is located on southwestern Turkey and has a complex structure which is a consequence of collision between African and Anatolian plates. In order to further understand this complexity, we deployed a temporary network consisting of nineteen broad band instruments in addition to KOERI's permanent seismic stations in the region. Crustal velocity and Moho depth variation were figured out along north – south and east – west profiles formed by fourteen temporary and permanent stations.

We implemented two different receiver function methods to the recorded events. Firstly, we applied joint inversion of receiver functions and surface wave group velocities in order to model lithospheric velocity structure of the region. Receiver functions are sensitive to shear wave velocity contrast and vertical travel times, however surface wave dispersion curves are sensitive to shear wave velocity averages. Combining these different properties of shear waves may bridge resolution gaps associated with each individual data set. Secondly, Moho depth was calculated by applying H-K stacking algorithm.

We found that the shear velocities for crustal and upper mantle thicknesses vary between 1.95-4.05 and 4.09-4.14 km/s, respectively, and in addition to this, Moho depth is varying between 30.5 and 40.7 km. beneath stations on the east – west profile. On the other hand, the shear velocities for crustal and upper mantle thicknesses vary between 1.41-4.05 and 3.97-4.23 km/s respectively, and the calculated Moho depth is between 35.5 and 47.0 km. beneath stations located on the north – south profile. Compared to the other geophysical studies done in the same region, this is the first study to understand unusual aspect of Isparta Angle.

ÖZET

P-ALICI FONKSİYONU KULLANILARAK ISPARTA BÜKLÜMÜ VE ÇEVRESİNİN KABUK YAPISININ BULUNMASI

Afrika ve Anadolu levhalarının çakışması sonucu karmaşık bir yapıya sahip olan Isparta büklümü, Türkiye'nin güney-batısındadır. Karmaşık olan bu yapıyı daha iyi anlamak için bölgeye KRDAE' nün sabit istasyonlarına ek olarak on dokuz adet geçici geniş bant aletler kurulmuştur. Kabuk yapısı ve Moho derinliği kuzey-güney ve doğu-batı profillerini oluşturan on dört adet geçici ve sabit istasyonlar boyunca çözümlenmiştir.

Bu çalışmada kayıt edilmiş depremlere iki farklı alıcı fonksiyon yöntemi uygulanmıştır. Birincil olarak, bölgedeki litosfer'in hız yapısını modellemek için alıcı fonksiyonların ve yüzey dalgası grup hızlarının birleşik ters çözümü uygulanmıştır. Alıcı fonksiyonlar kesme dalgası farklılığına ve düşey seyahat zamanına duyarlıdırlar, ancak yüzey dalgaları ortalama kesme dalgasına duyarlıdır. Kesme dalgasının bu iki farklı özelliğini bir araya getirerek tek bir yöntemden kaynaklanacak çözümleme eksikliklerine karşı bir bağlantı kurulabilir. İkincil olarak, Moho derinliği H-K yığma tekniği uygulanılarak hesaplanmıştır.

Doğu-batı profili üzerindeki istasyonların altındaki kabuk ve üst manto kalınlıkları için bulmuş olduğumuz kesme dalgası değerleri 1.95-4.05 ile 4.09-4.14 km/s sırası ile değişmektedir. Buna ek olarak, Moho derinliği 30.5 ve 40.7 km. aralığında bir değişim göstermektedir. Öte yandan, kuzey-güney profili üzerindeki istasyonların altındaki kabuk ve üst manto kalınlıkları için kesme dalgası değerleri 1.41-4.05 ve 3.97-4.23 km/s arasındadır. Moho derinliği ise 35.5 ile 47.0 km arasında değişmektedir. Bölgede yapılan diğer çalışmalarla karşılaştırıldığında, Isparta büklümünün karmaşık yapısını anlamak için yapılan ilk çalışma özelliğini taşımaktadır.

TABLE OF CONTENTS

LIST OF FIGURES

LIST OF TABLES

LIST OF SYMBOLS

H	Thickness of the velocity discontinuity
K	Poisson's ratio
p	Ray parameter
Ps	Converted Ps phase
Ppphs	Converted PpPhs phase
PsPhs+PpShs	Converted multiples PsPhs+PpShs phase
PsPhs	Converted multiples PsPhs phase
Vp	P-wave velocity
Vs	S-wave velocity
RFs	Receiver functions
SWs	Surface wave dispersion curves

1. INTRODUCTION

The ultimate aim of a seismologist is to explore earth's interior through examining seismic wave recordings that are created by natural or artificial sources. In this point of view, Lehman found the inner core, a zone of solid material, in early 1930s. In addition to this, Andrija Mohorovičić discovered an interface, studying recordings of Kupa valley earthquake in 8 October 1909 (Mohorovičić, 1910a) called the Moho discontinuity. Since Moho depth is varying depending on the type of crust, we can classify the structure of crust and find out tectonic evolution of continents.

Determination of Moho depth variation beneath a seismic station using teleseismic events started with Phinney, (1964) and Burdick and Langston, (1977). They tried to separate earth's response in frequency and time domain, respectively. A few years later, Langston, (1979) introduced the source equalization procedure to isolate the response of the crust and upper mantle beneath the station using P and S waves as recorded at the World-Wide Standard Seismograph Network station LON (Longmire, Washington). In addition to this, Owens *et al.,* (1984) described a time domain inverse modeling technique analyzing teleseismic P wave forms recorded on the mid-period pass band of Regional Seismic Test Network station RSCP. Although single-station receiver function analyses are usually limited to simple 1-D velocity modeling, the method is most sensitive to the details of the vertical shear velocity distribution in the crust (Owens *et al.,* 1984), the increased availability of three component, digital data and the simplicity of the technique combined to make receiver function modeling an attractive source of crustal structure information (Ammon *et al.,* 1993).

On the other hand, in the mid-1990s the receiver function method was improved by adding surface waves in to calculation. Özalaybey, (1997) present the joint inversion of receiver function and surface wave phase velocities. The basic difference from the other receiver function inversion techniques is to reduce the nonunique inversion results by adding surface wave phase velocity. Julia, (2000) extended the method of Özalaybey, (1997) to joint inversion of receiver functions and surface wave group and phase velocities to estimate the earth structure.

In this thesis, our study area is Isparta Angle located in south – western Turkey. The fourteen broadband seismic stations are chosen among thirty-nine seismic stations to create north – south and east – west profiles on the Isparta Angle. We applied the joint inversion of receiver functions and surface wave group velocities to find out the shear velocity structure. Also, we calculated crustal thickness utilizing H-K stacking algorithm. Our aim is to reveal complete crustal structure of the region by combining the result of these two different receiver function methods with the other geophysical studies.

1.1. Previous Geophysical Studies

Aegean region and south western Anatolia have been studied by many researchers and by using various methods. With the help of tomographic and earthquake location studies (Wortel and Spakman, 2000) and the GPS velocity vector study of Nyst and Thatcher, (2004), we have an idea about the movement of plates in the region. However, we do not have an idea about crustal structure of Aegean or south western Anatolia. Therefore, geophysical studies explained below, will provide us helpful information about the crustal structure of Aegean and south western Anatolia.

To begin with the receiver function studies, Kalyoncuoğlu and Özer, (2003) processed data downloaded from ISP station that is located close to the Isparta Angle to find out crustal structure beneath the station. They applied Haskell propagator matrix technique and Grid search method in order to calculate synthetic receiver functions and found mainly three distinct layers for crustal model. The surface layer has 2 km thickness and 2 km/s S wave velocity. The second layer is 15 km thick and it has 3.35 km/s S wave velocity. The third layer has 14 km thickness and it has 3.8 km/s S wave velocity. According to these results the depth of Moho is 31 +/-1 km. In addition to this, Yelkenci, (2006) applied H-K stacking method to receiver functions that were obtained from the same seismic station and Bolvadin seismic station which were located on the north of ISP station. She calculated 39.1 +/-1 km Moho depth with Vp/Vs = 1.75 for ISP and 34.3 +/-1.4 km Moho depth with Vp/Vs = 1.86 for Bolvadin station.

To continue with, the other receiver function study was done by Zhu *et al.*, (2006). They installed totally 50 seismic stations throughout the Menderes Massif in north – south

direction. In addition to their temporary stations, they process the data downloaded from 7 permanent stations. They used both H-K stacking method and common conversion point stacking method in order to calculate crustal thickness. The results show that crustal thickness in the central Anatolia is 36 km; 28 – 30 km in the central Menderes massif and 25 km beneath the Aegean Sea. More recently, Özakın, (2008) find out the crustal structure of south western Anatolia especially around the Gökova Bay. Including some permanent stations of KOERI, he used the data obtained from 12 seismic stations. He applied a new method by improving modified method of H-K stacking to RFs. His results indicate that the depth of Moho vary between 20 and 29.4 km from south to north respectively.

In order to see more extended picture of crustal structure of the Aegean region, Sodoudi *et al.*, (2006) applied P and S receiver function method with using 65 temporary and permanent seismic stations which cover whole Aegean region. The results of the study indicate that the southern part of the Aegean region has 20 – 22 km whereas the northern Aegean sea has 25 – 28 km crustal thickness. In addition to these, Moho depth vary between 32 – 40 km for Western Greece, 25 – 28 km for Peloponnesus, 25 – 33 km for Crete and lastly 26 – 30 km for Cyclades.

Except from the receiver function studies, Erduran *et al.,* (2007) studied surface waves with the data that was collected from ISP station. They found that the shear wave velocities are 2.2 – 3.6 km/s for depth of 0 – 10 km. The mid-crustal depth has low shear velocity which is 3.55 km/s with respect to shallow depth. Also their results indicate that the depth of Moho is changing between 25 and 45 km. They estimated 4.27 km/s shear wave velocity below the Moho.

The following two chapters include; the tectonic structure of the Isparta Angle and mainly two different hypotheses. The explanation of receiver function methods which the joint inversion of receiver function and surface wave group velocities including H-K stacking technique is described in Chapter 3. Chapter 4 includes the results of this study and lastly Chapter 5 contains conclusion and discussion of the results in comparison to other geophysical studies that were done in the same region.

2. EVOLUTION OF THE ISPARTA ANGLE

The Isparta Angle (IA) is located in south – western Turkey; its complex and enigmatic structure makes IA an ideal study area for many researchers. Evolution of IA is resulted by the affect of the interaction between the Arabian, African plates with Eurasia on the western Turkey. The Arabian plate is moving in a north-northwest direction relative to Eurasia at the rate of about 25 mm/yr (DeMets *et al.,* 1990, 1994). The movement of the Arabian plate is concluded with collision that caused westward displacement and counterclockwise rotation of the Anatolian block (McKenzie, 1972) that could be related to extension of Aegean.

On the other hand, the African plate is also moving in a northward direction relative to Eurasia at a rate of about 10 mm/yr (DeMets *et al.,* 1990) so that the displacement of the African plate is resulted in subduction of African plate underneath the Aegean plate and therefore is related to the slab pull which is the other debate about the extension of the Aegean (McKenzie, 1978; LePichon and Angelier, 1979). Within this tectonic framework, IA constitutes the junction between the Cyprus and Hellenic arcs and is a tectonic assembles which has a complex tectonic history (Barka *et al.,* 1997).

The unusual shape of the Isparta Angle (IA) is characterized by the Hellenic arc to the west and the Cyprus arc to the east as shown in Figure 2.1. The Hellenic arc seems to have a high deep angle and thus the Hellenic trench has a retreating nature with regard to Cyprus arc (Le Pichon and Angelier, 1979, 1981; Royden, 1993) and extension behind the Hellenic arc is arc-normal. On the other hand, Cyprus arc appears to involve a shallower subduction with two major seamounts - the Eratosthenes and Anixamander - impinging on the trench (Kempler and Ben-Avraham, 1987) and extension behind the Cyprus arc appears to be arc-parallel.

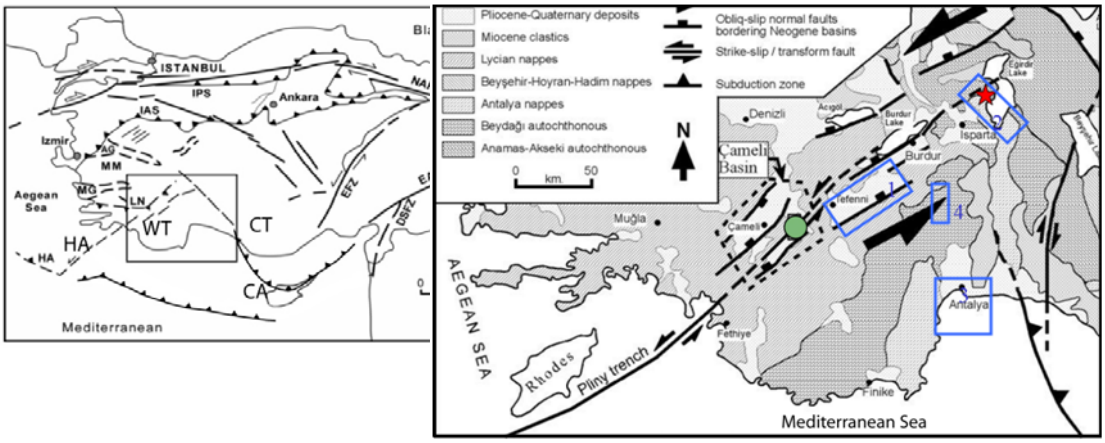

Figure 2.1. Tectonic map of western and central Turkey (left panel) and the Isparta Angle (right panel) showing major structural boundaries (modified from Cemen *et al.,* 1999 and Alcicek *et al.,* 2006). WT-Western Taurides; CT-Central Taurides; AG- Alasehir Graben; EAFZ-East Anatolian Fault Zone; EFZ-Ecemis Fault Zone; DSFZ-Dead Sea Fault Zone; IAS-Izmir-Ankara Suture Zone; IPS- Intra-Pontide Suture Zone; HA-Hellenic Arc; LN-Lycian Nappe Front; MM-Menderes Massif; MG-Menderes Graben. Box 1- Burdur Fault; Box 2- Sultandag near Aksehir; Box 3- Aksu Fault; Box 4- Kovada Graben.

There are two fundamentally different hypotheses for the tectonic framework of the IA. Firstly, Glover and Robertson, (1998) suggest that the IA is dominated by right lateral strike slip fault systems. The western side of the IA is dominated by strike-slip movement along the Burdur fault which indicates oblique fault mechanism with right lateral and normal displacements. They also believe that the major faults bounding the eastern side of the IA show right lateral fault mechanism with normal slip. Within these fault systems, the IA is an extensional system between the rotating blocks of western and eastern Anatolia. According to this view, a slab tear might localize the weak zone between the western and eastern Anatolia in North – South direction.

Secondly, Barka and Reilinger, (1997) suggest that faulting in the region is predominantly left-lateral so that the Burdur fault is left-lateral and acts as an accommodation zone between the Hellenic and Cyprus arc systems. In addition to this, the Sultandag and Aksu faults are thrust faults that accommodate present-day crustal shortening since Anatolia is over-riding the Cyprus arc. With respect to this view, the left-lateral Burdur fault is mainly responsible for slab tearing between the Hellenic and Cyprus

subduction systems. Extensional faulting within the Antalya basin is related to the strike-slip tectonism of the accommodation zone.

We have mainly two opposite views about IA whereas both of ideas have a common point which is slab tearing as shown in Figure 2.2.

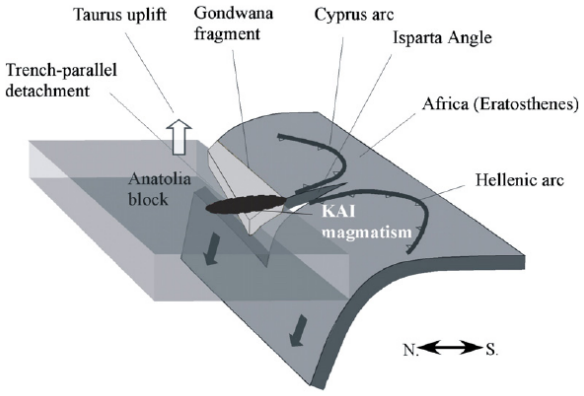

Figure 2.2. Cartoon illustrating a hypothetical slab-tear developing beneath the Taurus Mountains in response to the collision of one or more Gondwana indentors (indicated but not shown) with Anatolia. Hypothetical geometry of subducting African lithosphere beneath the Cyprus and Hellenic arcs is also shown (modified after Barka and Reilinger, 1997; Sandvol *et al.,* 2001, 2003). KAI -Kirka-Afyon-Isparta volcanic Weld.

Although the Benioff zones and tomographic images do not yield a clear profile of subducting slab geometry along the Anatolian African plate boundary, intermediate depth seismicity and significant continental deformation support the idea of slab tearing and the subsequent breakoff around the IA as shown in Figure 2.2 (Davies and Blanckenburg, 1995; Piromallo and Morelli, 1997; Wortel and Spakman, 2000). In addition to seismicity, existing Pn velocity maps of the region suggest that the central and western Taurus mountains are underlain by relatively slow and presumably hot uppermost mantle (Al-Lazki *et al.,* 2003), which would suggest that the lithosphere is thin and the topography is dynamically supported.

The direction of subducting slab geometries is obtained by the intermediate depth seismicity patterns which suggest that the Hellenic slab is subducting toward the northwest

and the Cyprian slab is subducting toward the northeast. Although global velocity models show very clear evidence of a high velocity slab along much of the Hellenic arc, the subducting slab along the Cyprian arc is much less clear (Bijwaard *et al.,* 1998; Wortel and Spakman, 2000).

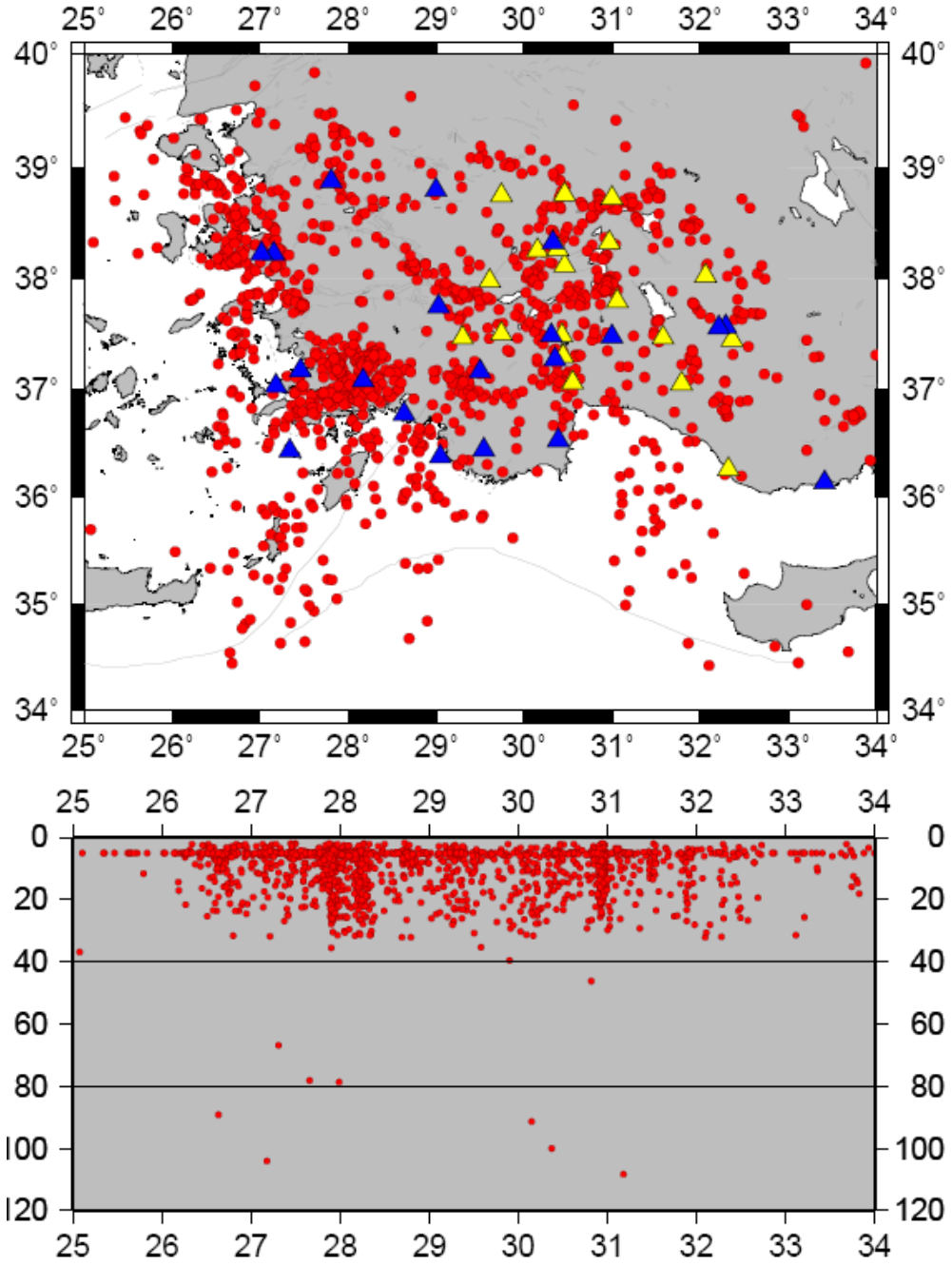

Figure 2.3. Seismic activity in the region (modified from Şahin *et al.*, 2008)

Figure 2.3 indicates that the location distribution of earthquakes in the region. Magnitudes are varying between 2.0 and 5.2. Location of earthquakes were obtained using permanent station of National Earthquake Monitoring Center in addition to temporary stations of the study.

3. RECEIVER FUNCTION ANALYSIS

3.1. Development of Receiver Function Analysis

The first crustal studies using teleseismic receiver functions were done by Phinney, (1964). He proposed that the spectral ratio of horizontal and vertical component seismograms could be used to find out crustal layering. The main advantage of this technique is that it does not require the knowledge of the incident waveform whereas the main disadvantage is the lack of the stability (Burdick and Langston, 1977).

Burdick and Langston, (1977) investigated kind of S phases within the P waveform by comparing records of the radial component and vertical component of teleseismic records. They believed that S phases can be related to P to S conversion at discontinuities beneath the receiver and they also tried to model the crustal structure by comparing synthetic seismograms with the recorded data. After this application Langston introduced the source equalization procedure in 1979 to isolate the response of the crust and upper mantle which is called receiver function beneath the station by deconvolving radial response from vertical response in frequency domain.

Owens, (1984) developed a time domain inversion technique which utilizes receiver functions obtained by source equalization procedure of Langston, (1979) in order to find out crustal structure of his study area. This inversion technique utilized radial receiver function with the assumption of a crust parameterized by many thin, flat and homogeneous layers.

In addition to frequency domain deconvolution, Ligorria and Ammon, (1999) described an iterative time domain deconvolution approach to estimate receiver function. Although the both, time and frequency domain, types of deconvolution method indicate good results for the data downloaded from permanent stations, iterative time domain deconvolution shows more reliable results for the data downloaded from temporary stations.

Zhu and Kanamori, (2000) developed H-K stacking technique to estimate crustal thickness. This stacking technique is converting time domain receiver function in to depth (H) and Vp/Vs domain. The advantages and disadvantages of this technique will be described in 3.3.1.

More recently Julia, (2000) introduced the joint inversion method by using both receiver function and surface waves. This is very different than the other techniques since it uses basically different types of data. Receiver functions are sensitive to shear wave velocity contrasts but they contain no absolute velocity information. On the other hand surface waves are sensitive to vertical shear wave averages, whereas they do not include any information about the shear velocity contrast. Therefore, combining the information of both receiver function and surface waves together will reduce the problem, that is the non-uniqueness of receiver function inversions (Ammon, 1990) and produce more reliable solutions for crustal structure. This property of joint inversion of receiver functions and surface waves makes it superior with respect to the other receiver function methods.

Fundamentally, there are two types of receiver function techniques. The former is the P – receiver function; the initial receiver function technique as explained above. The latter is the S – receiver function technique. The main difference between these two techniques is the first one uses P to S converted phases whereas the second one uses S to P converted phases. The advantage of S receiver function is that the converted S to P phases arrives earlier than the main S phase so that conversions from upper mantle do not mix with crustal multiples (Li *et al.,* 2004; Sodoudi *et al.,* 2006). This provides us an advantage for upper mantle studies.

In this thesis, P – receiver functions were used to find out the crustal structure of the Isparta Angle (IA).

3.2. Basics of Receiver Function Analysis

Teleseismic receiver functions are often used to determine crustal and upper-mantle discontinuities beneath a seismic station (Langston, 1977; Owens *et al.*, 1984; Li *et al.,* 2000; Yuan *et al.*, 2000). Teleseismic P waveforms recorded at a three-component seismic

station include significant information about the earthquake source, the Earth structure in the vicinity of both the source and the receiver, and mantle propagation effects. It is the most important for the receiver function studies that the Earth structure beneath and near the receiver among these information. In order to gain this, the response of crust and upper mantle should be isolated from the other factors which interact with the observed seismograms recorded at teleseismic distances.

The main idea in the receiver function studies is that the teleseismic incident P wave will be converted to S wave when the incident P wave come across a relatively sharp velocity discontinuities in the crust and upper mantle. The ray paths of converted P wave and corresponding phases are shown in Figure 3.1 and Figure 3.2.

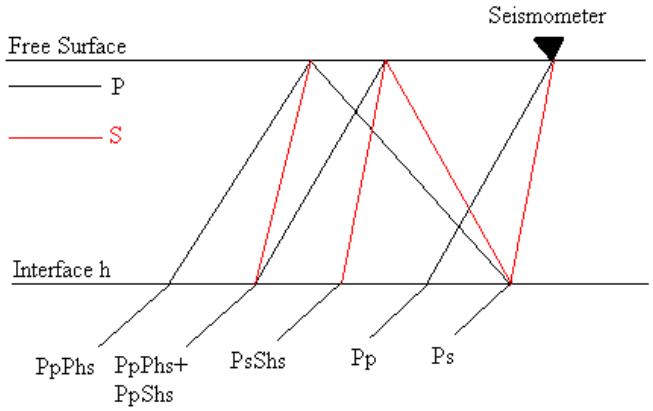

Figure 3.1. Phase arrivals of teleseismic incident P wave at a seismic station in a homogeneous isotropic medium (modified from Ammon, 1991).

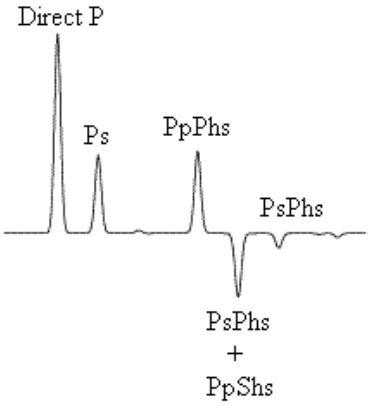

Figure 3.2. Receiver function traces that show direct, converted, and multiples direct P, Ps, PpPhs, PsPhs+PpShs, PsPhs respectively (modified from Ammon, 1991).

The amplitude of converted phases and multiples depend on the P wave incidence angle and the size of the velocity contrast that generates the Ps and multiples PpPhs and PsPhs+PpShs. In addition to this, the arrival times of the converted phases and multiples depend on the depth of the velocity contrast and P wave incidence angle.

In receiver function studies, selecting the appropriate teleseismic events is very important before isolating the receiver functions. In order to do this, the basic criteria, generally, is that the magnitudes of teleseismic events should be greater than 5.5 since teleseismic events below this magnitude could not be recorded clearly. The other basic criteria is that the epicentral distances of teleseismic events should be between 30 and 90 degrees P waves are steeply incident and dominate on the vertical component of ground motion, whereas Ps converted phase are contained almost exclusively on the horizontal components of ground motion in this epicentral distances (Cassidy, 1992). A significant note in here is the azimuthal coverage of teleseismic events. This is simply because the structure of the Earth could vary with azimuth and distance and therefore the instrument response will be different depending on the azimuth and distance. In order to gain a reliable receiver functions for the study area, a good azimuthal coverage is needed. In addition to azimuthal coverage, the seismometer type used in the receiver function analysis could affect the results also. Generally, three component broad-band seismometers are preferred to use since they have a flat velocity response throughout most of the lower frequency bands in contrast to the spectrum of short period stations, which has a better coverage of seismic energy.

The selected teleseismic events with properties given above need to be filtered. Since the receiver function studies utilize teleseismic events, high frequency content in the teleseismic recording could affect result in an unexpected way. By applying 0.05 Hz to 1 Hz or 0.1 Hz to 1 Hz band pass filter, the high frequency content are eliminated which are affected by small-scale heterogeneities and site effects in the waveform. Also filtering makes it easier to see first P wave arrival in recordings of teleseismic events which will help windowing the data. Filtered teleseismic events should window long enough including converted phases and multiples. Therefore, it is common to window teleseismic events are generally windowed 60 seconds before the first P wave arrival to see pre-signal noise and 60 seconds after the first P arrival. This is because, converted and reverberated phases from

crust and upper mantle discontinuities are generally expected within the 60 seconds after the first P wave arrival time. However, the window length could vary depending on the thickness of crust.

In receiver function analysis, the last step before deconvolution procedure is rotating the filtered and windowed teleseismic events. Broadband three component seismometers record teleseismic events on vertical (Z) and horizontal (N-S), (E-W) components. However, the radial (R) and tangential (T) components of the records need to be rotated to separate Ps converted waves from direct P waves. Horizontal components, in other words (N-S) and (E-W) components will be R and T components respectively. The reason of using ray based coordinate systems is that radial component is more sensitive to SV and transverse component is more sensitive to SH. In addition to this, P to SV converted phases which have primary importance in receiver function studies are radially polarized and observed on radial component. On the other hand P to SH components are transversally polarized so that it should be on the transverse component. Back-azimuth (BAZ) was used to rotate events to R and T components. Back-azimuth could be calculated if we know the coordinates of station and hypocenter of event. It is the angle measured between the vector pointing seismic station to source and seismic station to north (Scherbaum and Johnson, 1992), simplified model of BAZ given in Figure 3.3.

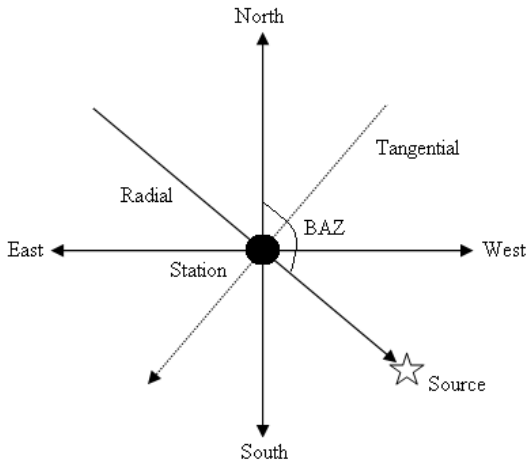

Figure 3.3. The back-azimuth (BAZ) (modified from Zor, 2002).

The effects of filtering, windowing and rotating can be seen in the following Figure 3.4.a and Figure 3.4.b. The first one shows row data downloaded from Akören (AKRN)

station. The second figure shows the result of filtering, windowing and rotating which belongs to the same teleseismic event.

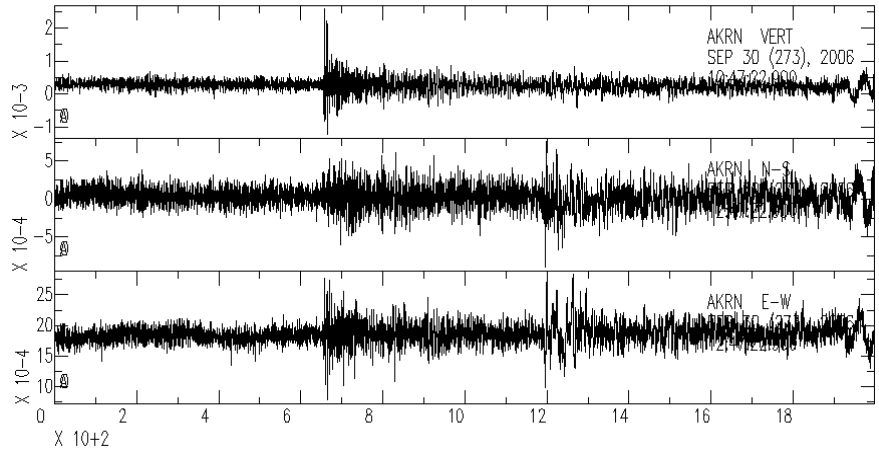

(a)

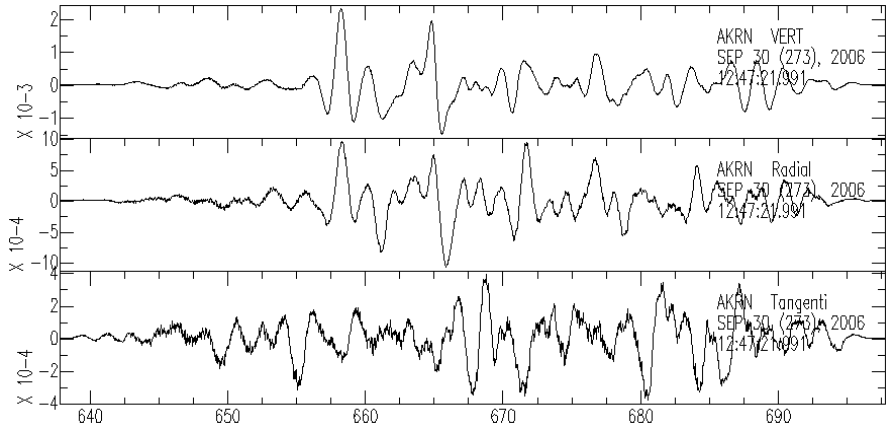

(b)

Figure 3.4. The teleseismic event that recorded at Akören station on julian date of 273, 2006, with magnitude 5.6 Mb. a) Raw data. b) The data after filtering, windowing, rotating.

The preparation of raw data will result in the application of deconvolution procedure which is the gaining of radial and tangential receiver functions. In receiver function studies, the means of deconvolution is spectral division of the radial and transversal components to vertical component. By applying deconvolution, we are eliminating the effects of the source, ray path and instrument response so that we obtain the signal which

includes the first arriving P wave and later arriving S wave conversions and locally generated reverberations beneath the stations. The deconvolution can be done either in time or in frequency domain. In estimating receiver functions, the deconvolution technique in frequency domain was proposed by Langston, (1979) and in the time domain was proposed by Liggoria and Ammon, (1999).

3.2.1. Frequency Domain Deconvolution

According to Langston, (1979), in the time domain, the form of the theoretical displacement response for a P plane wave impinging under a stack of horizontal or dipping interfaces can be given by

$$D_V(t) = I(t) * S(t) * E_V(t) \tag{3.1}$$

$$D_R(t) = I(t) * S(t) * E_R(t) \tag{3.2}$$

$$D_T(t) = I(t) * S(t) * E_T(t) \tag{3.3}$$

As we see on the equations, the theoretically calculated displacement response is equal to convolution of $I(t)$ that is the impulse response of the recording instrument, $S(t)$ that is the seismic source function and $E_V(t), E_R(t)$ $E_T(t)$ that are the vertical radial and tangential impulse response of the earth structure.

In the recordings, the horizontal components of ground motion will generally be different from the vertical component since the earth structure beneath the seismic station will produce P to S type phase conversions. The advantage of this difference is that the vertical component is composed of a steeply incident P wave consists of a large direct arrival followed later by only minor arrivals because of crustal reverberations and phase conversions except there is no high velocity structure (> 2 km / sec) in the earth structure beneath the seismic station. Therefore, we can assume the vertical impulse response of the earth structure as a Dirac delta function $\delta(t)$.

$$E_V(t) \approx \delta(t) \tag{3.4}$$

Using the advantage of this assumption, the vertical component of the ground motion will be

$$D_V(t) \approx I(t) * S(t) \tag{3.5}$$

We can clearly see that the above equation is include the same parameters $I(t)$ and $S(t)$ as in equations 3.2 and 3.3 which mean the radial $D_R(t)$ and the transversal $D_T(t)$ displacement response. If we would like to gain the radial and transversal impulse response of the earth structure, it will be enough to deconvolve $D_V(t)$ from $D_R(t)$ and $D_T(t)$. In the frequency domain this process will be equal to division of radial component with vertical component,

$$E_R(\omega) = \frac{D_R(\omega)}{I(\omega)S(\omega)} \approx \frac{D_R(\omega)}{D_V(\omega)} \tag{3.6}$$

$$E_T(\omega) = \frac{D_T(\omega)}{I(\omega)S(\omega)} \approx \frac{D_T(\omega)}{D_V(\omega)} \tag{3.7}$$

$E_R(\omega)$ and $E_T(\omega)$ are our radial and tangential receiver functions and they can be retransformed back into the time domain. In order to make the denominator real we can multiply denominator with complex conjugate $D_V^*(\omega)$ so that the radial receiver function will equal to,

$$E_R(\omega) = \frac{D_R(\omega)D_V^*(\omega)}{D_V(\omega)D_V^*(\omega)} \tag{3.8}$$

By adding a complex conjugate to our calculation, $E_R(\omega)$ can be defined for the entire frequency band of spectrum. The same calculation could be done for $E_T(\omega)$.

In order to limit the final frequency band by excluding high frequency signals not obviously present in the original recording, equation 3.8 is multiplied by the Gaussian

filter. The reason of choosing low pass Gaussian filter is that its smooth symmetric shape, zero phase distortion and lack of side-lobes (Langston, 1979).

$$E_R(\omega) = \frac{D_R(\omega) D_V^{*}(\omega)}{D_V(\omega) D_V^{*}(\omega)} G(\omega) \tag{3.9}$$

In equation 3.9 $G(\omega)$ is low pass Gaussian filter and can be defined as

$$G(\omega) = e^{-\omega^2/4\alpha^2} \tag{3.10}$$

In equation 3.10 α controls the width of Gaussian pulse and it is used to remove high frequency content. The values of α and corresponding frequency is shown in Table 3.1.

Table 3.1. The α values with respect to frequencies at which $G(\omega)$ is equal to 1 (modified from Ammon,http://eqseis.geosc.psu.edu/~cammon/HTML/RftnDocs/seq01 .html)

α values	Frequency(Hz)
10	4.8
5	2.4
2.5	1.2
1.25	0.6
1.0	0.5
0.625	0.3
0.5	0.24
0.4	0.2
0.2	0.1

In equation 3.9, the divider term could take very small or zero values for certain sections of the frequency spectrum. Consequently, the division by very small or zero values could lead to numerical problems in the frequency domain. Therefore, equation 3.8 is not used to compute the radial response of the earth. In order to eliminate problems, a

technique suggested by Helmberger and Wiggins, (1971) and Dey-Sarkar and Wiggins, (1976b) called water level deconvolution technique is applied to equation 3.9.

$$E_R(\omega) = \frac{D_R(\omega)D_V{}^*(\omega)}{\Phi_{SS}(\omega)}G(\omega) \tag{3.11}$$

The divider term of equation 3.9 $D_V(\omega)D_V*(\omega)$ is replaced by $\Phi_{SS}(\omega)$ that is equal to,

$$\Phi_{SS}(\omega) = \max\{D_V(\omega)\,D_V*(\omega),\, c\,\max[D_V(\omega)\,D_V*(\omega)]\} \tag{3.12}$$

The function $\Phi_{SS}(\omega)$ can be thought of as simply being the autocorrelation of $D_V(\omega)$ with any spectral troughs filled to a level depending on the water level parameter, c (Langston, 1979). $\Phi_{SS}(\omega)$ is used to replace small values in equation 3.12 with a fraction of the maximum value of the denominator. The consequences of replacing small values with larger values in the denominator result in an attenuation of spectral energy at frequencies for which the vertical component has small amplitude (Ammon, 1991).

3.2.2. Iterative Time Domain Deconvolution

In some cases, which deconvolution method is superimposed the other one is not important. It has a direct relation with the kind of seismic data used in the study. According to Liggoria and Ammon, (1999), if the data has good signal to noise ratio and belongs to a permanent station that works for many years at the same place; both frequency and iterative time domain deconvolution method should give similar results. However, if the data is downloaded from a temporary station and has no good signal to noise ratio, deconvolution method to be used in the study should be chosen carefully since the results vary.

The basic aspect of iterative time domain approach is a least square minimization of the difference between the observed horizontal seismogram and a predicted signal generated by the convolution of an iteratively updated spike train with the vertical

component seismogram (Liggoria and Ammon, 1999). Iterative time domain deconvolution method can be applied to both radial and transverse components.

Let us look at now how this method works: first, the vertical component is cross correlated with the radial component to estimate the lag of the first and largest spike in the receiver function. Then the result is convolved with the vertical component seismogram and subtracted from radial component seismogram. The result will again be cross correlated with the vertical component. Therefore, the misfit between the correlated receiver function and radial component will be reduced by every iteration. This procedure will go on to estimate other spike lags and amplitudes until the misfit and additional spikes become unimportant (Liggoria and Ammon, 1999).

Although we can clearly observe direct P and converted Ps phases in figure 3.5, there is a difference on these radial receiver functions between 8 and 11 seconds. The source of the small difference could be the improper water level used in frequency domain deconvolution.

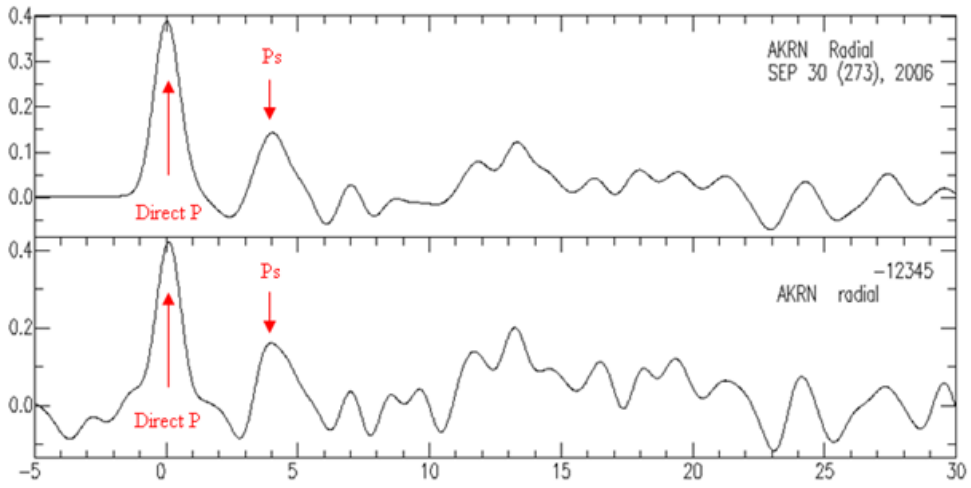

Figure 3.5. Radial receiver functions that are obtained from iterative time domain deconvolution (top) and frequency domain deconvolution (down) belong to the teleseismic event recorded at Akören seismic station as in Figure 3.4.

In the following paragraphs, receiver function techniques used in this thesis will be described.

3.3. Receiver Function Techniques

3.3.1. H-κ Stacking Technique

Teleseismic receiver functions can be used for estimating crustal thickness H and V_P/V_S ratios beneath a station since the $P-to-S$ converted phase at the Moho and the first multiply reverberated phases in the crust generally apparent in the receiver function waveforms and their relative travel times then can be employed to constrain the thickness and the V_P/V_S below the recording station (Zandt and Ammon, 1995).

In receiver function recording, the first phase at $t=0$ referred to as direct P wave arrivals is a measure of the zero lag correlation between the radial and vertical components. The next strong phase around $t \approx 5$ second represents the P_S converted phase due to the Moho (Eaton *et al.,* 2006). Crustal thickness can be calculated by using the time seperation between P and P_S for a given average crustal velocities,

$$H = \frac{t_{Ps}}{\sqrt{\frac{1}{V_S^{\,2}} - p^2} - \sqrt{\frac{1}{V_P^{\,2}} - p^2}} \tag{3.13}$$

In equation 3.13, p is the ray parameter of the incident wave, V_P and V_S are average crustal velocities, H is the thickness of the crust, t_{Ps} is the time separation between P and P_S.

Calculating crustal thickness using time separation between direct and converted phase with equation 3.13 will not produce reliable results due to trade off between depth and velocity. However, we can eliminate this difficulty with adding later converted phases that are P_PP_S and $P_PS_S + P_SP_S$.

The crustal thickness can be calculated using the arrival time of the P_PP_S,

$$H = \frac{t_{PpPs}}{\sqrt{\frac{1}{V_S^{\,2}} - p^2} + \sqrt{\frac{1}{V_P^{\,2}} - p^2}} \tag{3.14}$$

and for $P_P S_S + P_S P_S$,

$$H = \frac{t_{PpSs+PsPs}}{2\sqrt{\frac{1}{V_S^{\,2}} - p^2}} \tag{3.15}$$

By using equations 3.13, 3.14 and 3.15 both κ and H can be calculated (Zhu, 1993; Zandt *et al.,* 1995; Zandt and Ammon, 1995). The intersection of curves as in the Figure 3.6 will give the best values of H and κ.

However, it is not generally easy to identify converted P_S phases and other multiples $P_P P_S$ and $P_P S_S + P_S P_S$ due to background noise, scattering from crustal heterogeneities, and P to S conversions from other velocity discontinuities. In order to increase signal to noise ratio, stacking multiple events on the time domain will be helpful.

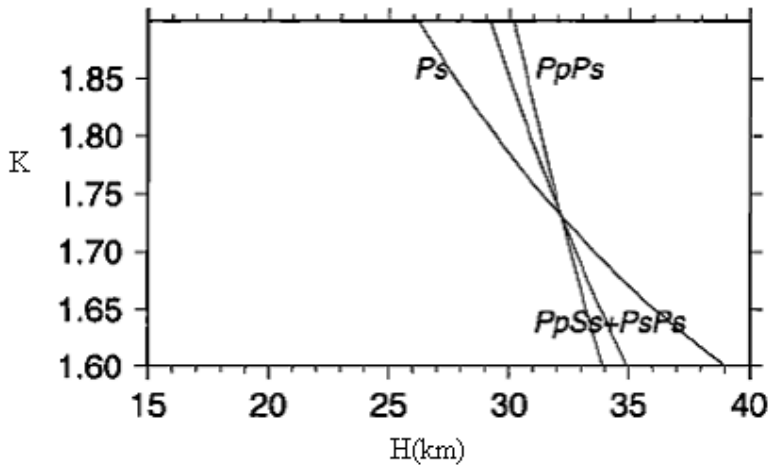

Figure 3.6. $H - \kappa$ relations, as given in equations 3.13, 3.14 and 3.15 for different Moho converted phases. (after Zhu and Kanamori, 2000).

Therefore, Zhu and Kanamori, (2000), have developed a $H-\kappa$ stacking technique that sums the amplitudes of receiver functions at the predicted arrival times of P_S, P_PP_S and $P_PS_S+P_SP_S$ for different crustal thicknesses H and κ. This transforms the time domain receiver functions directly into the depth and V_P/V_S domain without the need of identifying converted phases and multiples and to pick their arrival times with assuming a starting average P wave velocity model. $H-\kappa$ stacking can be defined as

$$s(H-\kappa)=\sum_j w_1 rf_j(t_1)+w_2 rf_j(t_2)-w_3 rf_j(t_3) \tag{3.16}$$

where H is the thickness κ is the V_P/V_S ratio, $rf_j(t)$ are the receiver functions, with j ranging from 1 to the total numbers of wave forms. t_1 ,t_2 and t_3 are the predicted P_S, P_PP_S and $P_PS_S+P_SP_S$ arrival times corresponding to crustal thickness H and V_P/V_S ratio (κ) as given in the 3.13 – 3.15, w_i are weighting factors and total of them will be equal to one.

$$\sum w_i = 1 \tag{3.17}$$

Among these weighting factors, the highest one (w_1) will belong to the delay time of P_S almost 60 – 70 % since P_S is converted from the Moho and it is most clearly observed receiver function recording. In addition to this, the weightening factor of P_PP_S (w_2) will have 20 – 30 % and the weightening factor of last multiple (w_3) which is $P_PS_S+P_SP_S$ will affect 0 – 10 % the calculation.

The best estimation of H and κ are found where there phases are stacked coherently. An example is shown in figure 3.7. The different weightening factors were applied the same receiver functions.

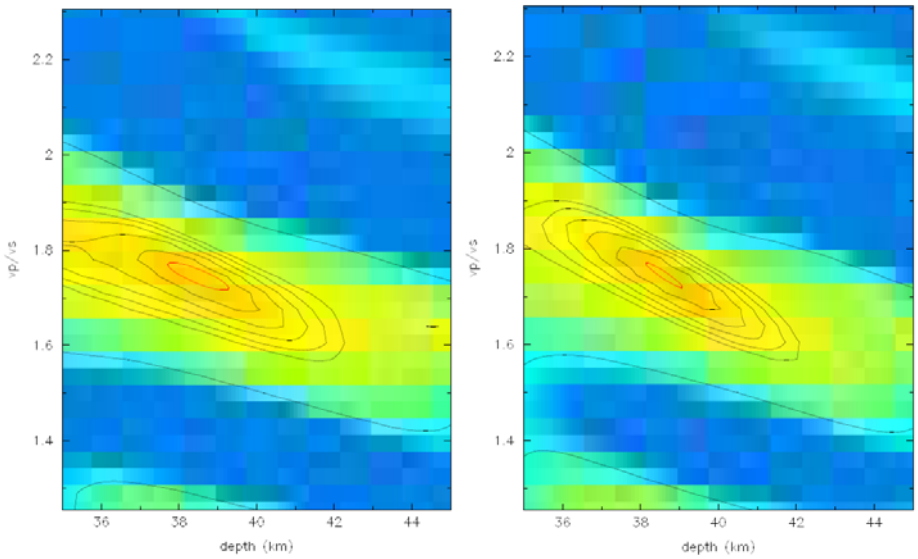

(a) (b)

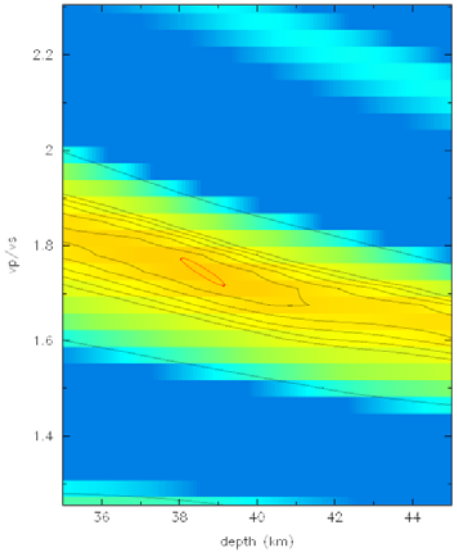

(c)

Figure 3.7. The result that obtained different weighting factors for ISP station. a) $w_1 = 5$, $w_2 = 2$, $w_3 = 1$ b) $w_1 = 5$, $w_2 = 5$, $w_3 = 0$ c) $w_1 = 9$, $w_2 = 1$, $w_3 = 0$. Even different weighting vales the results are very close to each other. $H = 38.6 \pm 0.1$ and $\kappa = 1.75$.

An advantage of this of method is that the differential arrival times of converted phases and multiples are less affected by lateral velocity variations since the conversion

point of P to S is close to the station. In addition to this, using of differential times in the calculations, crustal P velocity is not as strong as converted S velocity.

On the other hand, the disadvantage of this method is that we assume a planar, homogeneous Moho discontinuity and no lateral variation in our calculations. However, if Moho is dipping the V_P/V_S will be affected in the basis of longer travel times for multiples traveling up-dip with respect to those generated at a horizontal interface (Ligorria, 2000). Conversely, multiples travelling down-dip will travel shorter distances. This will lead the variation for V_P/V_S and depth. Another disadvantage is that the presence of gradational Moho discontinuity instead of sharp, well defined Moho discontinuity (Julia, 2004). This condition is the reason of the energy from the boundary interaction phases that spread in time so that the corresponding pulses decrease in amplitude and increase in width (Cassady, 1992; Liggoria, 2000). In addition to this, $H-\kappa$ stacking method has a difficulty in intra-crustal discontinuities. Converted phases and multiples from intra-crustal discontinuities could interfere with the real Moho Ps converted phase which will be resulted in time shift of the P_S peak. The variation in P_S time will lead to unrealistic thickness and V_P/V_S ratios.

3.3.2. The Method of Joint Inversion of Receiver Functions and Surface Waves

Obtaining crustal earth structure by combining surface wave dispersion observations and receiver functions can supply more reliable results when compared to methods that use single type of data. Ammon, (1990) showed that receiver functions are sensitive to shear velocity contrast of interfaces in the medium and relative travel times of converted and reverberated waves between those interfaces. Inversions of such teleseismic P wave receiver functions for shear wave structure are non-unique which means given various earth models observed and predicted receiver functions fit well. This is because, there is not enough absolute velocity information contained in the receiver functions (Özalaybey, 1997).

The problem of non-uniqueness could be reduced with the help of adding an independent data set such as surface wave dispersion curves into the inversion. The main

characteristics of surface wave dispersion are sensitive to the average shear velocity structure of the material within the depth ranges to which they penetrate (Özalaybey, 1997). This kind of information is not provided by receiver functions; therefore it is the biggest drawback. However, by combining these two independent data sets, we expect the inversion results to overcome all the missing parts that are related to both receiver function and surface wave dispersion.

To begin with linearized inversion procedure, our aim is to translate receiver function and surface wave dispersion observations into a model of subsurface shear velocity structure so that the forward problem can be expressed as Julia, (2000),

$$y = F[x] \tag{3.18}$$

In equation 3.18, y is N dimensional vector of data points, x is a M dimensional vector that describes the model and $F[\ ]$ is a nonlinear operator that maps vectors in the model space into vectors in the data space and for receiver functions it would represent the numerical computation of synthetic waveforms. On the other hand for dispersion curves, $F[\ ]$ would represent the numerical evaluation of dispersion velocities. x would be taken as a M dimensional vector of the shear wave velocities in fixed thickness layers of the lithosphere. Equation 3.18 is inverted by a linearized, iterative approach for the nonlinear problem (Menke, 1984),

$$\delta(y) = \nabla F\Big|_{x_n} \cdot \delta x_n \tag{3.19}$$

$$x_{n+1} = x_n + \delta x_n \tag{3.20}$$

$\delta x_n = x - x_n$ is the model correction vector and $\delta(y) = y - F[x_n]$ is the residual data vector. Equation 3.19 could be solved for δx_n using least squares techniques (Wiggins, 1972; Jackson, 1972). In order to start iterative procedure, an initial model required which is x_0.

Julia *et al.,* (2000), solved equation 3.20 in terms of a linear inverse operator, $\left(\nabla F\Big|_{x_n}\right)^{-g}$ with respect to generalized inversion theory (Menke, 1984; Tarantola, 1987), which can be written as,

$$\delta x_n = (\nabla F\Big|_{x_n})^{-g} \cdot \delta y \tag{3.21}$$

This inverse operator can be obtained by minimizing some functional such as in Russell, (1987) who used a differential damped least squares scheme that minimized to invert dispersion curves.

$$\phi = \left\| \delta y - \nabla F\Big|_{x_n} \cdot \delta x_n \right\|^2 + \theta^2 \left\| D \cdot \delta x_n \right\|^2 \tag{3.22}$$

In equation 3.22, is obtained by giving an *a priori* influence to the norm of a first difference solution vector during inversion process through a non negative parameter θ^2 that is smoothness given in order to eliminate rapid, physically untenable, velocity variations with depth. $D \cdot \delta x_n$ is a vector of the first differences between shear velocity perturbations in adjacent layers. In equation 3.22 the matrix D is

$$D = \begin{pmatrix} 1 & -1 & 0 & \cdots & 0 \\ 0 & 1 & -1 & \cdots & 0 \\ 0 & 0 & 1 & \cdots & 0 \\ \vdots & \vdots & \vdots & \ddots & \vdots \\ 0 & 0 & 0 & \cdots & 1 \end{pmatrix} \tag{3.23}$$

Julia *et al.,* (2000) developed a joint inversion technique which is a linearized shear velocity inversion that is solved using a damped least squares scheme in equation 3.22 to implement the joint inversion of receiver functions and dispersion curves using the joint prediction error E . The joint prediction error can be expressed as,

$$E_{y/z} = \frac{p}{N_y}\sum_{i=1}^{N_y}\left(\frac{y_i - \sum_{j=1}^{M} Y_{ij}x_j}{\sigma_{y_i}}\right)^2 + \frac{1-p}{N_z}\sum_{i=1}^{N_z}\left(\frac{z_i - \sum_{j=1}^{M} Z_{ij}x_j}{\sigma_{z_i}}\right)^2 \tag{3.24}$$

In equation 3.24, y could be the residual dispersion curve, Y could be the partial derivative matrix and x the shear velocities for a given set of plane layers with fixed thickness, and z could be the residual receiver function and Z could be the partial derivatives matrix. N_y and N_z are the number of data points for each data set and σ_{yi}^2 and σ_{zi}^2 are the corresponding variances. p is *a priori* value that trades off between the relative influences of each data set called the influence factor.

In order not to dominate one data set to another, both data sets are equalized for the number of data points and physical units in the inversion process. This is achieved by in equation 3.24 by dividing the individual prediction error for each data set by the number of data points and variance. For example, if we minimize one data set, it will produce estimation $x^{(y)}$ with a prediction error close to the value $N_y\overline{\sigma}_y^2$ and the similar way, minization the other data set will produce estimation $x^{(z)}$ with a prediction error close to $N_y\overline{\sigma}_z^2$. In here $\overline{\sigma}^2$ is the mean value of the variance of the data set.

Julia *et al.,* (2000), have implemented the minimization described in equation 3.24 through the following weighted system of equations,

$$\begin{pmatrix} \alpha_1 y_1 \\ \vdots \\ \alpha_{N_y} y_{N_y} \\ \beta_1 z_1 \\ \vdots \\ \alpha_{N_z} z_{N_z} \end{pmatrix} = \begin{pmatrix} \alpha_1 Y_{11} & \alpha_1 Y_{12} & \cdots & \alpha_1 Y_{1M} \\ \vdots & \vdots & \ddots & \vdots \\ \alpha_{N_y} y_{N_y 1} & \alpha_{N_y} y_{N_y 2} & \cdots & \alpha_{N_y} y_{N_y M} \\ \beta_1 z_{11} & \beta_1 z_{12} & \cdots & \beta_1 z_{1M} \\ \vdots & \vdots & \ddots & \vdots \\ \beta_{N_z} Y_{N_z 1} & \beta_{N_z} Y_{N_z 2} & \cdots & \beta_{N_z} Y_{N_z M} \end{pmatrix} \begin{pmatrix} x_1 \\ x_2 \\ \vdots \\ x_M \end{pmatrix} \tag{3.25}$$

where,

$$\alpha_1^{\,2} = \frac{p}{N_y \sigma_{yi}^2} \quad \text{and} \quad \beta_1 = \frac{1-p}{N_z \sigma_{zi}^2} \tag{3.26}$$

and minimizing ϕ in equation 3.22 in each iteration, the partial derivatives being recomputed as the model is updated. In equation 3.25 the a priori knowledge of the data variances $\overline{\sigma}_{yi}^2$ and $\overline{\sigma}_{zi}^2$ are assumed, if there is no a priori knowledge is available, the weights in equation 3.26 is can be approximated by,

$$\alpha_1^2 = \frac{p}{N_y \left(\sigma_y^a\right)^2} \text{ and } \beta_1^2 = \frac{1-p}{N_z (\sigma_z^a)^2} \tag{3.27}$$

In equation 3.27, $\left(\sigma_y^a\right)^2$ and $\left(\sigma_z^a\right)^2$ are values for the data variances. $\left(\sigma_z^a\right)^2$ for receiver functions can be estimated from the transverse component and $\left(\sigma_y^a\right)^2$ for dispersion curves the value depends on the data quality, path length.

In addition the equalization, an influence parameter p is added in equation 3.24. This is because, generally, shear velocities for both data sets are not equal to each other $x^{(y)} \neq x^{(z)}$ due to noise included in the data but they are close to each other. Therefore, to investigate the full range of solutions between these two cases, the influence parameter can take the values between 0 and 1 in which for $p = 0$ there will no effect of surface waves, in other words, y in the equation 3.24. The joint inversion error would be solved for receiver functions. In an opposite way the influence factor for $p = 1$, there will be no effect of receiver functions that is z in equation 3.24 so that the joint inversion error would be solved for only surface wave dispersion data. The other values for influence parameter p can be given and which value of it would affect in better way for the joint inversion error can be determinated.

In this thesis, iterative time domain deconvolution is applied to the teleseismic P wave recordings to obtain receiver functions. The teleseismic events were selected according to their magnitude and epicentral distances that should be equal or greater than

5.5 magnitude and between 30 and 90 degrees respectively. Firstly, the method of joint inversion of receiver functions and surface waves were applied to the receiver in order to obtain the crustal structure and shear wave velocity model of the study area which is absence in the H-K stagking procedure. However the method of joint inversion does not indicate any information about crustal thickness. In order to cope with this situation, secondly, H-K staking procedure was applied to the receiver functions to calculate the crustal thickness including proper H and K values. As a result, we find out the detailed crustal structure of study area including Moho depths and shear velocities.

4. DATA AND DATA ANALYSIS

4.1. Data

In south- eastern Aegean around Isparta Angle, a total of thirty-nine broad band three component seismic stations were used to determine the seismic properties of the region. 16 permanent stations belong to National Seismic Monitoring Center, 9 temporary stations were deployed by B.U. Kandilli Observatory and Earthquake Research Institute (KOERI): Department of Geophysics under Boğaziçi University Research Fund (BRF-07T203), 10 temporary seismic stations were deployed by University of Missouri, 3 permanent seismic stations belong to Süleyman Demirel University and lastly one seismic station belongs to IRIS. Station locations are shown in Figure 4.1. In this thesis, we processed the data of ten temporary and four permanent broadband seismic stations that create simply north – south and east – west profiles among thirty-nine stations to determine the Moho depth variation and velocity structure of crust and upper mantle for the region. Distribution of stations that were selected for the study is given in Figure 4.2 and the details about the stations were given in Table 4.1.

Table 4.1. Station parameters used in the study

Tmp and Prm indicate the temporary and the permanent stations, respectively.

Stations name & type	Latitute	Longitute	Altitute (m)	Seismometer	Data avaliability range	Recorded Data Format
Acıpayam (ACPY) / Tmp	37.471	29.301	921	Guralp-6TD	03/22/2007 - 11/14/2007	GCF
Yeşilova (SALD) / Tmp	37.495	29.735	1265	Trillium-120	11/29/2006 - 08/08/2007	Miniseed
Çeltikçi (CLTK) / Tmp	37.492	30.434	934	Guralp-6TD	03/14/2007 - 11/13/2007	GCF
Sütçüler (SUTC) / Prm	37.476	30.999	1180	Guralp-3T	01/29/2007 - 08/12/2007	GCF
Huğlu (HULU) / Tmp	37.471	31.58	1380	Trillium-120	08/19/2006 - 08/10/2007	Miniseed
Akören (AKRN) / Tmp	37.45	32.357	1150	Guralp-3T	08/17/2006 - 08/17/2007	Miniseed
Afyon (AFYN) / Tmp	38.762	30.464	1078	Guralp-6TD	03/14/2007 - 11/15/2007	GCF
Şuhut (SHUT) / Prm	38.33	30.33	1215	Guralp-3TD	11/02/2006 - 12/31/2007	GCF
Haydarlı (HYDR) Tmp	38.268	30.381	1267	Guralp-6TD	03/14/2007 - 11/12/2007	GCF
Uluborlu (ULUB) / Tmp	38.120	30.463	1135	Guralp-6TD	03/14/2007 - 11/12/2007	GCF
Isparta (ISP) / Prm	37.49	30.31	1000	STS-1	08/01/2006 - 06/30/2007	SAC
Kızılkaya (KZLK) / Tmp	37.298	30.44	830	Trillium-120	11/29/2006 - 05/10/2007	Miniseed
Döşemealtı (DSMA) / Tmp	37.060	30.550	341	Guralp-6TD	03/27/2007 - 11/12/2007	GCF
Antalya (ANTB) / Prm	36.89	30.65	20	Guralp-6TD	08/01/2006 - 08/01/2007	SAC

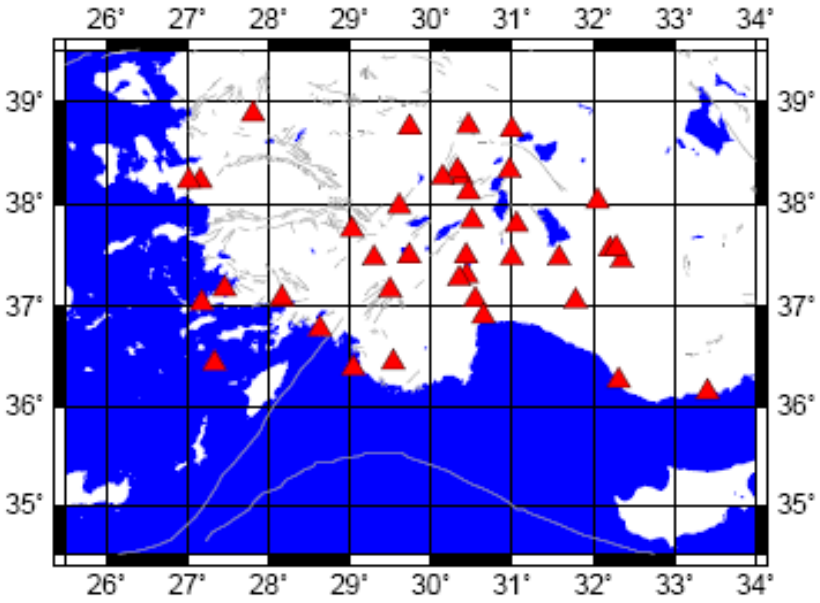

Figure 4.1. Location of all seismic stations.

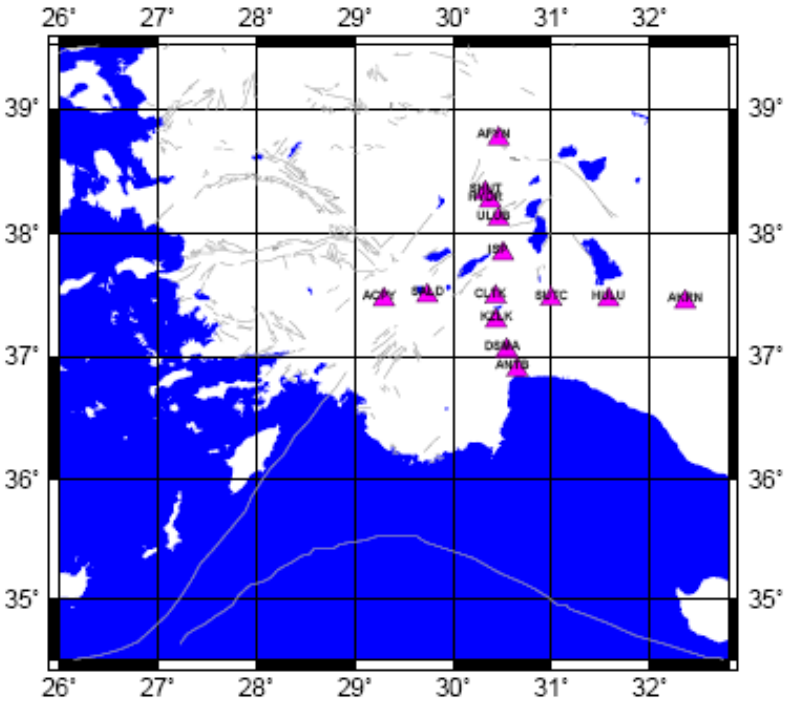

Figure 4.2. Distribution of seismic stations in this study.

299 events were chosen from the USGS earthquake catalog to obtain P - receiver functions, the distribution of events are given in Figure 4.3 and the list of the events will be given in Appendix A. The basic criteria while creating the event catalog is that the

magnitude should be greater than 5.5 and epicentral distances should be between 30 – 90 degrees. The reasons of criteria and more information about the data were given in section 3.2. Because of the different operation time of seismic stations and eliminating events that include high noisy content, we could not use the same events for all seismic stations. The data availability range for stations is shown on Table 4.1.

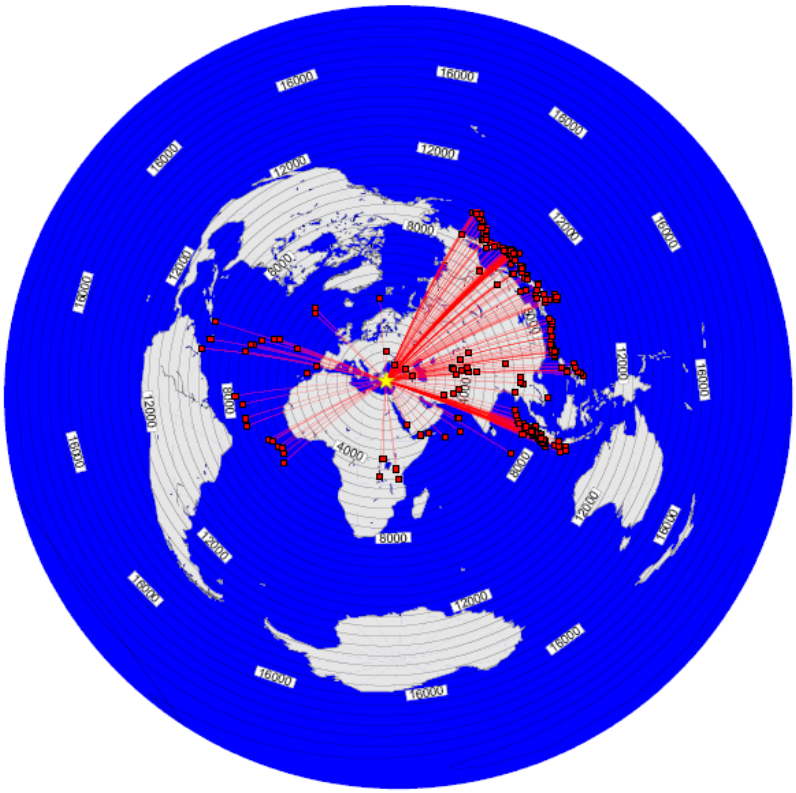

Figure 4.3. Azimuthal coverage of total events.

Since the data formats are different station to station, firstly, we converted all GCF data format to miniseed data format. The reason of doing this conversion is that we used a script which uses the miniseed data format in order to separate teleseismic events from the raw data as shown in Figure 4.4. The script uses miniseed data at the beginning but it converts the data for a given event list to segy data format. Using segy data, it cuts and merges the selected teleseismic events. The script produces sac data at the end of the process.

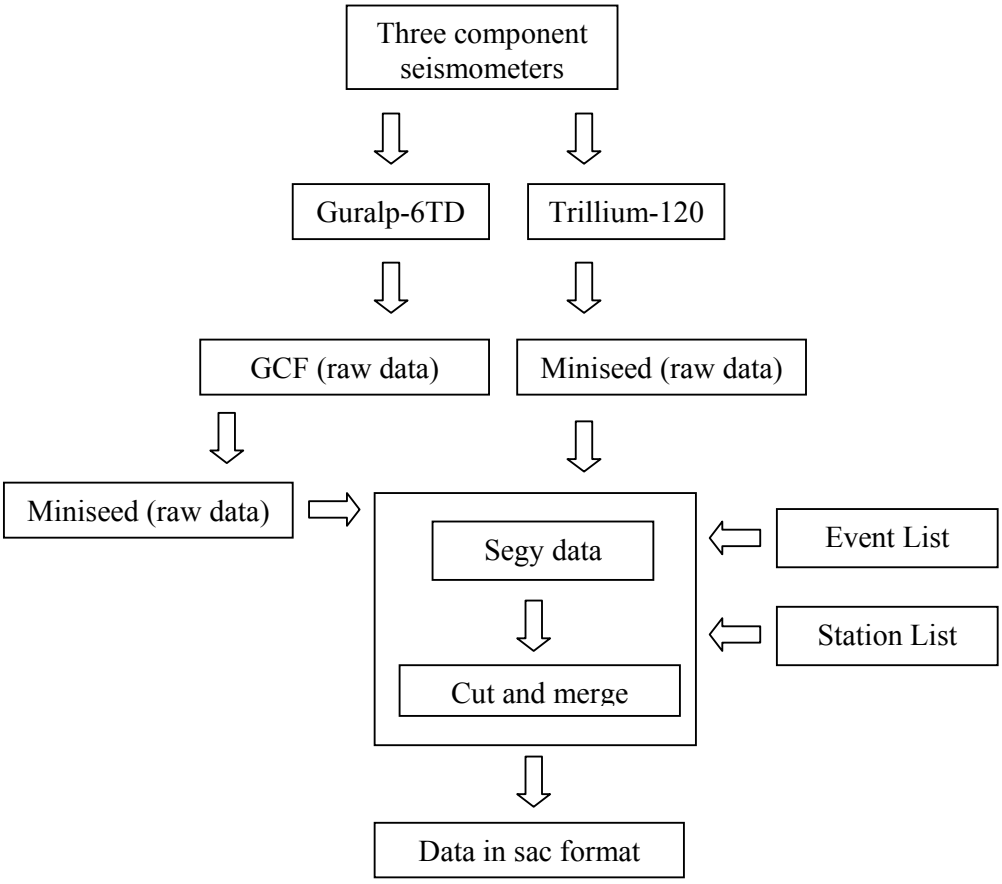

Figure 4.4. The flow chart of the data conversion.

However, we realized that there are undesired spikes with the cut teleseismic events that converted gcf to miniseed data format as shown in Figure 4.5. On the other hand, we had no undesired spikes the miniseed data that were downloaded from trillium seismometers with Taurus digitizers.

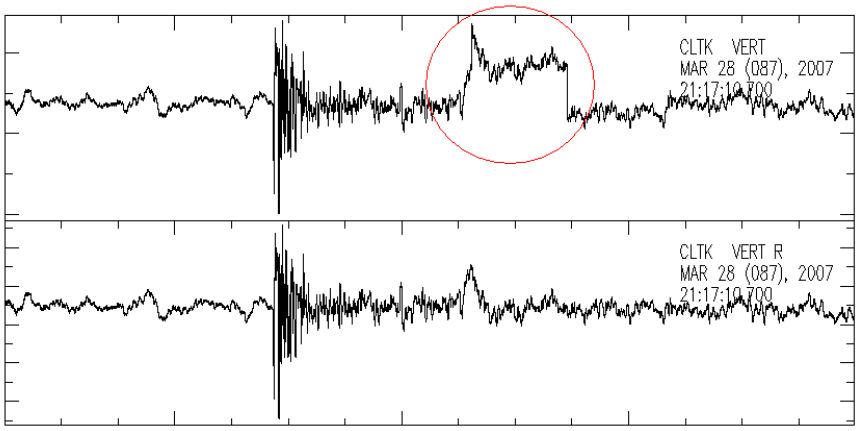

Figure 4.5. Shows the vertical components of teleseismic event recorded on CLTK station. At the top figure indicate the data that was converted miniseed to sac file and at down shows the data that were converted segy to sac file.

In order to solve this ambiguity, we made a modification to the script. After this modification, the script uses segy data format at the beginning and produces again sac files at the end of the process as given in the Figure 4.6. However, we had to convert all gcf files to segy format to use the script, and as a result of this we spent more time on the data conversion. After this modification there were no problems in selected teleseismic wave forms.

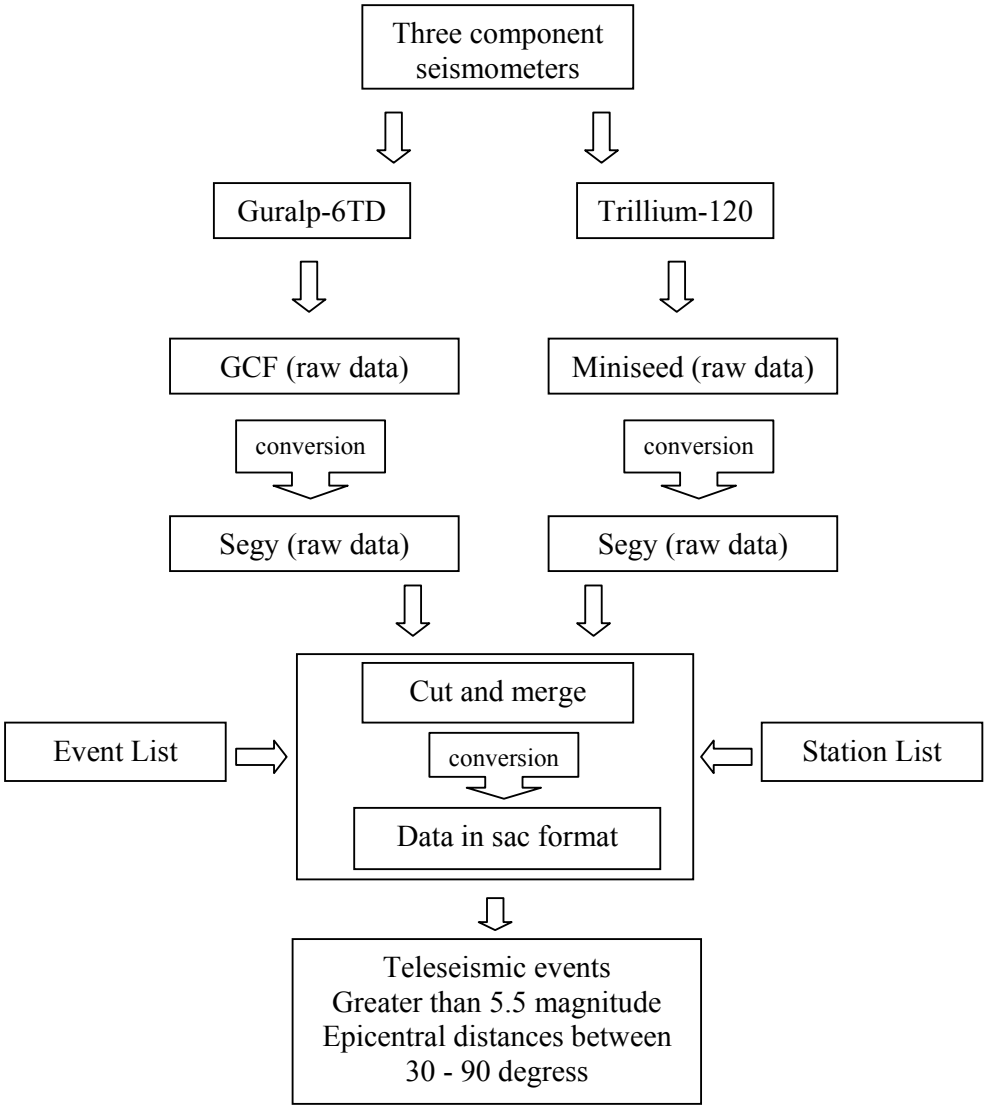

Figure 4.6. The flow chart of the data conversion after the modification.

Secondly, the data that were recorded in sac format which belongs to ISP and ANTB station are cut and merged by using sacmerge as shown in Figure 4.7.

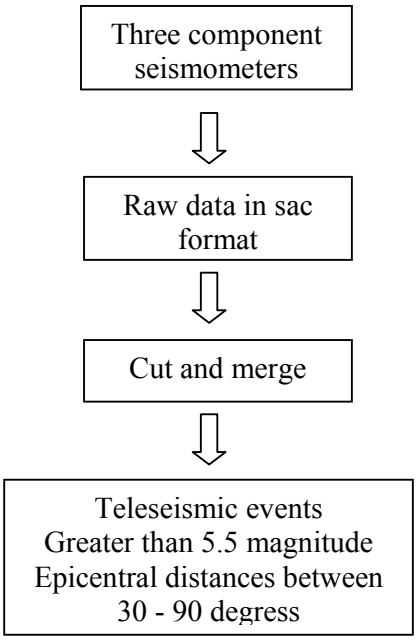

Figure 4.7. The flow chart for the data of ISP and ANBT station.

As a result, we had three component teleseismic event records in sac data format with magnitude greater than 5.5 and located between 30 and 90 degrees epicentral distances.

Since our initial aim is to study the structure of crust and upper mantle, it would be enough to cut the teleseismic events 20 sec before and 40 sec after. The reason of this windowing is that it is common to expect converted phases and multiple in 40 or 60 sec. from the P wave arrival. By applying 0.05 – 1 Hz band pass filter, we are eliminating high frequency noise content and are picking more precise P wave arrivals on the teleseismic recording. The P wave arrivals on the data were picked by hand and horizontal components (N-S and E-W) were rotated to radial (R) and tangential (T) components according to back-azimuth of teleseismic events. The reasons of doing these conversions are written in chapter 3.2.

Iterative time deconvolution was applied to rotated and windowed data by using 1.5 Gaussian with factor and 200 iterations. As a result of deconvolution, we obtained radial and tangential receiver functions as shown in Figure 4.8. We examined the obtained

receiver functions and realized that some of Ps converted phases are not clearly observed, and some of them were not compatible with the other receiver functions for the same receiver functions or some of them even did not like a receiver function. We eliminated these receiver functions by hand.

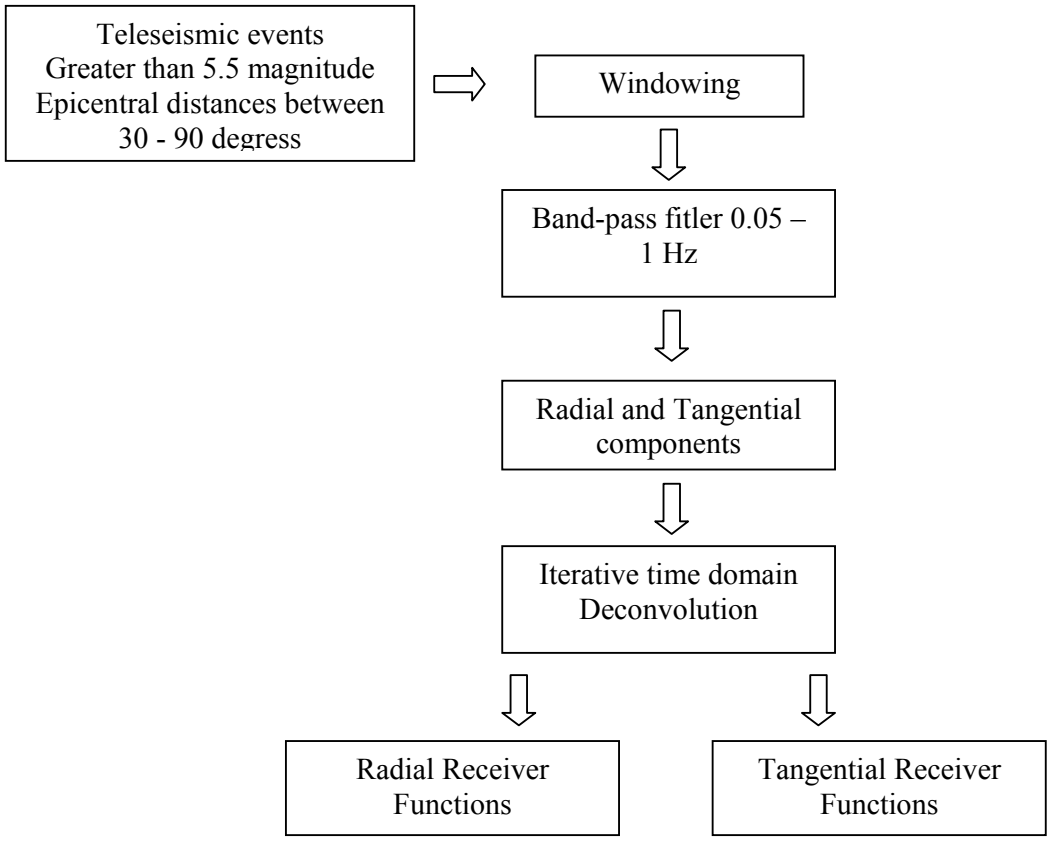

Figure 4.8. The derivation of radial and tangential receiver functions.

We applied the method of joint inversion of receiver functions and surface waves by using the computer codes developed by Julia *et al.,* (2000) to find out shear wave velocity structure of the crust. We have P – receiver functions (RFs) for now on so we need to surface wave (SW) dispersion curves to implement joint inversion with our data set.

In this thesis we tried to use basically two types of SW dispersion curves. The first group of SW dispersion curves were obtained by the study of Erduran *et al.*, (2007). He evaluated surface wave group velocities the period range of 5 and 25 sec. at ISP station. However, this period range is narrow for the joint inversion of RFs and SW when we

compare with the other studies that used joint inversion code (Julia *et al.,* 2003; Julia *et al.,* 2005; Gök *et al.,* 2007; Mulugeta *et al.,* 2007). On the other hand, the most important is that SW dispersion curves was obtained only for the ISP station in the study of Erduran *et al.,* (2007) but we have thirteen more seismic stations so that we need thirteen more SW dispersion curves at those stations. Therefore, surface waves dispersion curves obtained from the study of Erduran *et al.,* (2007) were not used in this study.

The second group of surface wave dispersion curves was provided by Michael Pasyanos. Pasyanos studied the region Eurasia, North Africa and surrounding regions in 2005 using 30.000 Rayleigh and 20.000 Love wave paths. He used a conjugate gradient method to perform group velocity between 7 and 100 sec. on 1^{O} x 1^{O} grid and at resolutions approaching 1^{O} under some condition. The Rayleigh wave dispersion curves for each of our fourteen stations were extracted from his tomography study and utilized in this study.

In addition to the Rayleigh wave dispersion curves, joint inversion of receiver functions and surface wave dispersion curves require a starting initial model. Firstly, we created an initial model by combining the study of Zor, (2002) and Kalafat, (1995). Also the model of Kalafat, (1995) is a reference model for south western Turkey and used by the National Earthquake Monitoring Center. We called this as initial velocity Model – 1 as given in Table 4.2. Secondly, we created another velocity model called initial velocity Model – 2 by using Kalyoncuoğlu *et al.,* (2003) that is about obtaining crustal structure under ISP seismic station by receiver function with using grid search method as given in Table 4.2.

Table 4.2. The initial velocity models.

a) Model – 1

Layers	Thickness (km)	Vp (km/s)	Vs (km/s)
1	2,00	3,50-4,40	2,00-2,57
2	13,00	4,40-5,80	2,57-3,31
3	14,00	5,80-6,60	3,31-3,77
4	8,00	6,60-6,92	3,77-3,95
5	6,00	6,92-7,78	3,95-4,45
6	57,50	7,78-8,10	4,45-4,62

b) Model -2

Layers	Thickness (km)	Vp (km/s)	Vs (km/s)
1	2	3.40-4.00	1.96-2.30
2	15	4.00-5.60	2.30-3.23
3	21	5.60-6.80	3.23-3.92
4	61.5	6.80-7.21	3.92-4.16

We used $Wd/r = 0.5$ value which is the relative influence value of each data set, 0.5 for smoothness value and p, the ray parameter, which is the averaged ray parameter value of RFs while running the joint inversion.

As a result, by using initial Model - 1 and initial Model – 2 with joint inversion of RFs and SW dispersion curves, we created average velocity model for study region as given in Figure 4.9. The results for each station will be given in section 4.2.

H-K stacking method of Zhu and Kanamori, (2000) was also applied to obtained P – receiver functions to calculate crustal thickness in the study region which is not indicated in the joint inversion. Combining the results of these two different methods, we present a detailed crustal structure around the Isparta Angle.

In the Data Analysis, section 4.2., below firstly the radial and tangential receiver functions are given. After that, the results of joint inversion of RFs and SW dispersion curves with average velocity models for two different initial models are shown. Also, the results of H-K stacking method with Vp/Vs ratio corresponding h (depth) value are shown.

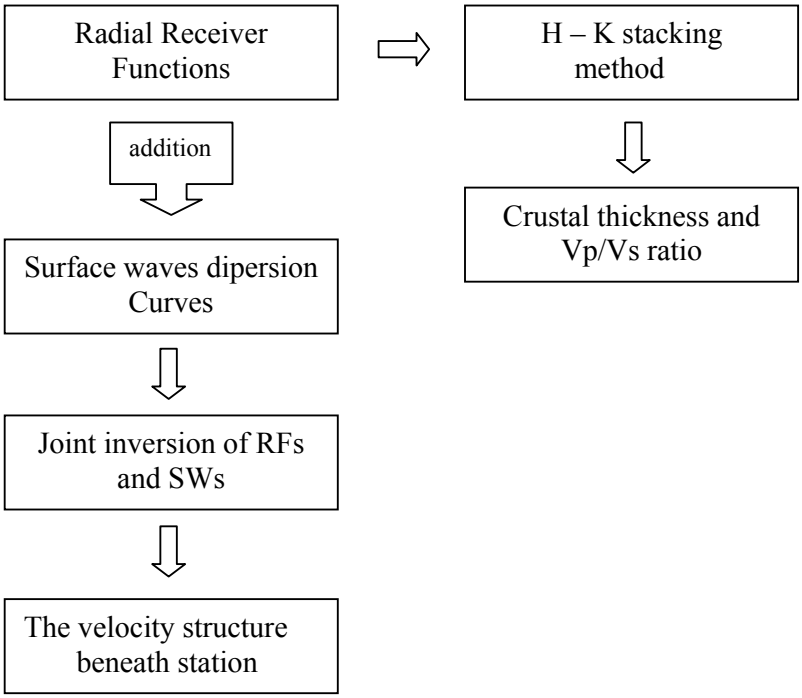

Figure 4.9. The work order of the two different methods.

4.2. Data Analysis

4.2.1. East – West profile: ACIPAYAM (ACPY) station

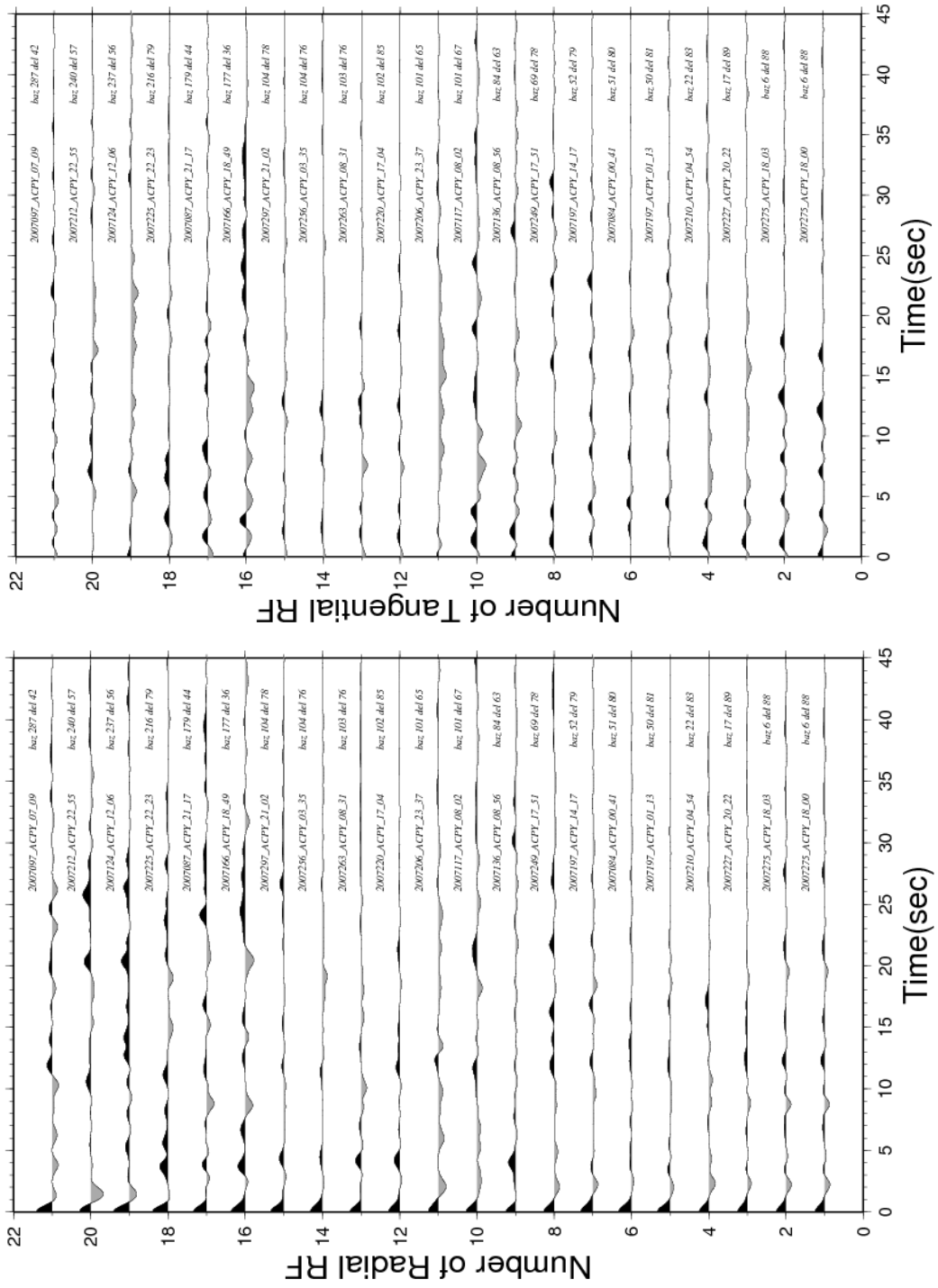

Figure 4.10. The radial and tangential RFs for ACPY station.

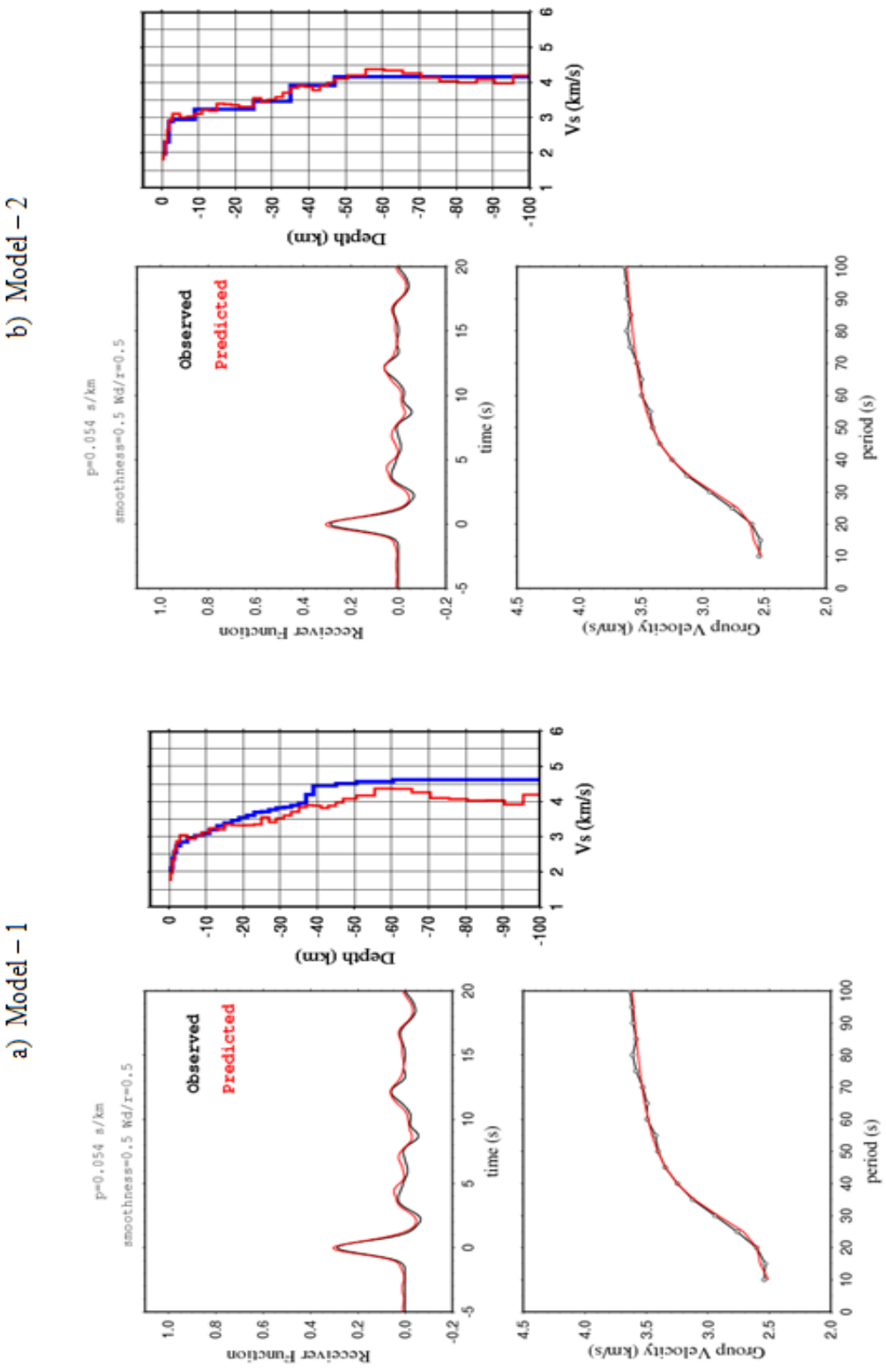

Figure 4.11. Joint inversion of RFs and surface waves with two different initial models beneath the ACPY station.

Table 4.3. Velocity structure beneath the ACPY station.

a) The average velocity results using Model – 1.

Layers	Thickness (km)	Vp (km/s)	Vs (km/s)	ρ (g/cm^3)
1	2,00	3,80	2,17	2,37
2	13,00	5,36	3,06	2,37
3	14,00	5,91	3,38	2,62
4	8,00	6,41	3,66	2,74
5	6,00	6,75	3,86	2,90
6	57,50	7,20	4,11	3,07

b) The average velocity results using Model – 2.

Layers	Thickness (km)	Vp (km/s)	Vs (km/s)	ρ (g/cm^3)
1	2,00	3,80	2,19	1,99
2	13,00	5,35	3,08	2,48
3	14,00	5,88	3,39	2,65
4	8,00	6,35	3,66	2,80
5	6,00	6,68	3,85	2,91
6	57,50	7,14	4,12	3,06

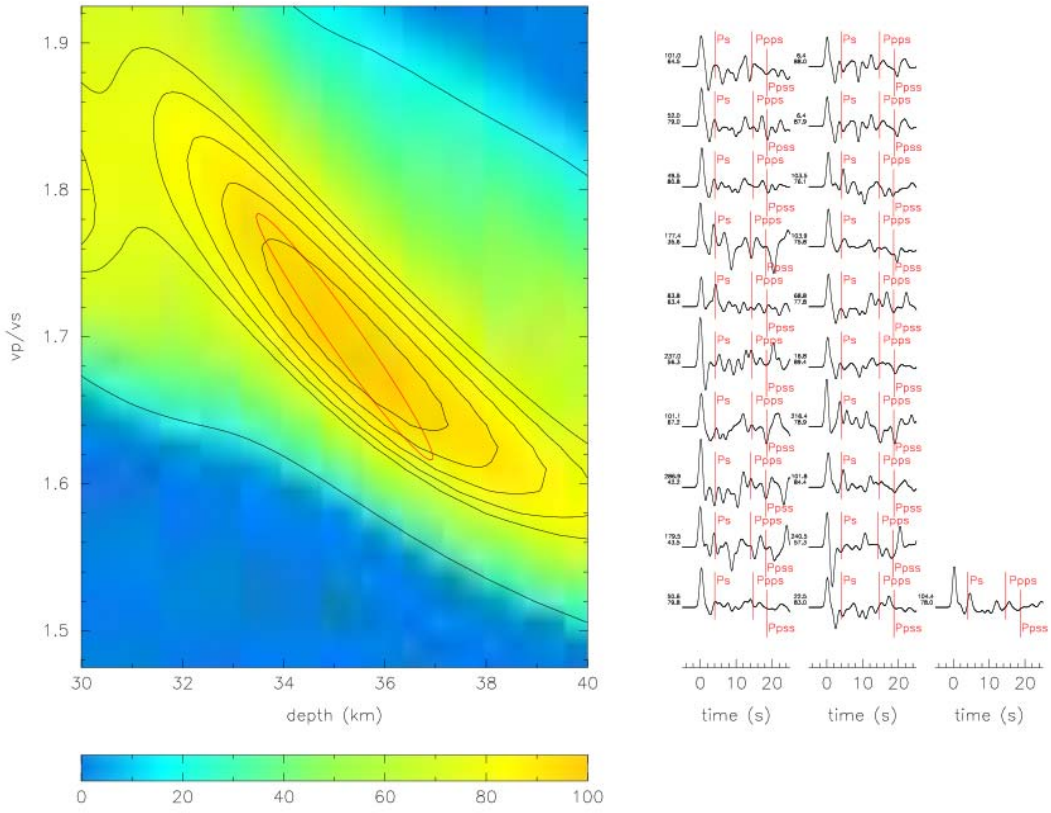

Figure 4.12. The $H-\kappa$ stacking result for ACPY station.

($V_P = 6.3$ Km/s $h = 35.2 \pm 3.5$ $V_P / V_S = 1.70 \pm 0.17$ $corr = -97.7\%$)

4.2.2. East – West profile: SALDA (SALD) station

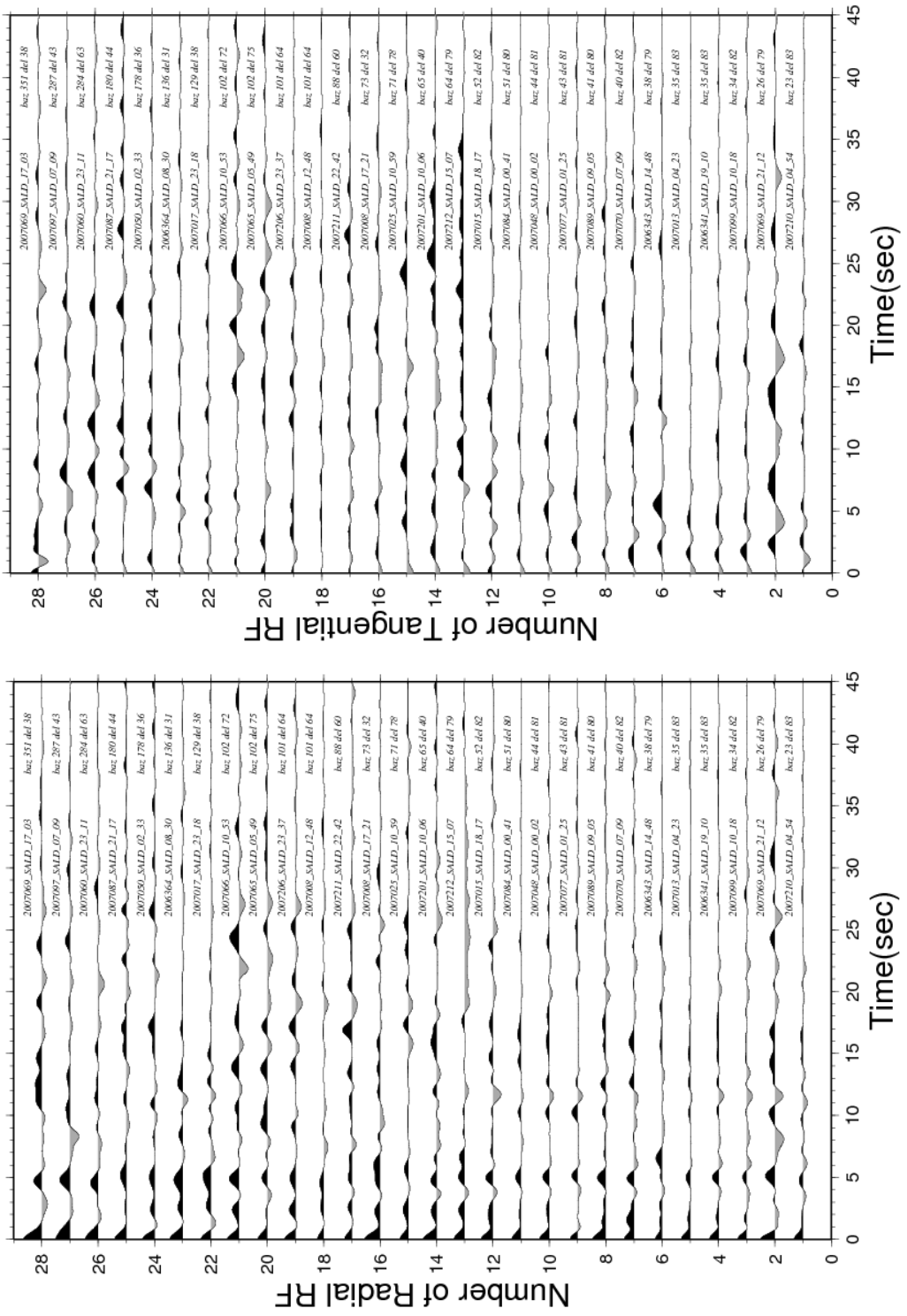

Figure 4.13. The radial and tangential RFs for SALD station.

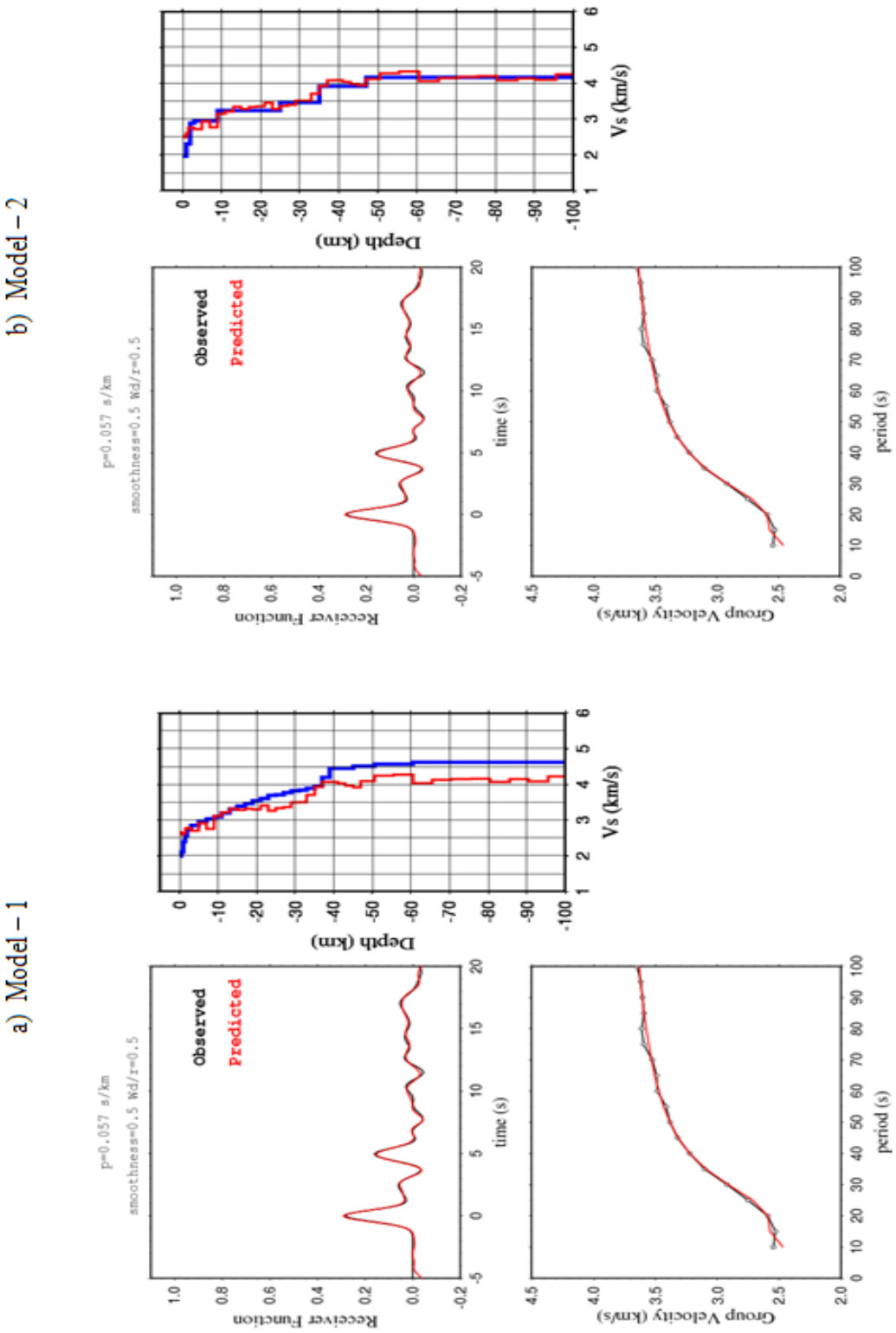

Figure 4.14. Joint inversion of RFs and surface waves with two different initial models beneath the SALD station.

Table 4.4. Velocity structure beneath the SALD station.

a) The average velocity results using Model – 1.

Layers	Thickness (km)	Vp (km/s)	Vs (km/s)	ρ (g/cm^3)
1	2,00	4,66	2,66	2,26
2	13,00	5,20	2,97	2,43
3	14,00	5,82	3,32	2,63
4	8,00	6,40	3,66	2,82
5	6,00	7,09	4,05	3,04
6	57,50	7,21	4,11	3,08

b) The average velocity results using Model – 2.

Layers	Thickness (km)	Vp (km/s)	Vs (km/s)	ρ (g/cm^3)
1	2,00	4,50	2,59	2,21
2	13,00	5,17	2,98	2,42
3	14,00	5,81	3,35	2,63
4	8,00	6,35	3,66	2,80
5	6,00	7,05	4,06	3,02
6	57,50	7,17	4,13	3,06

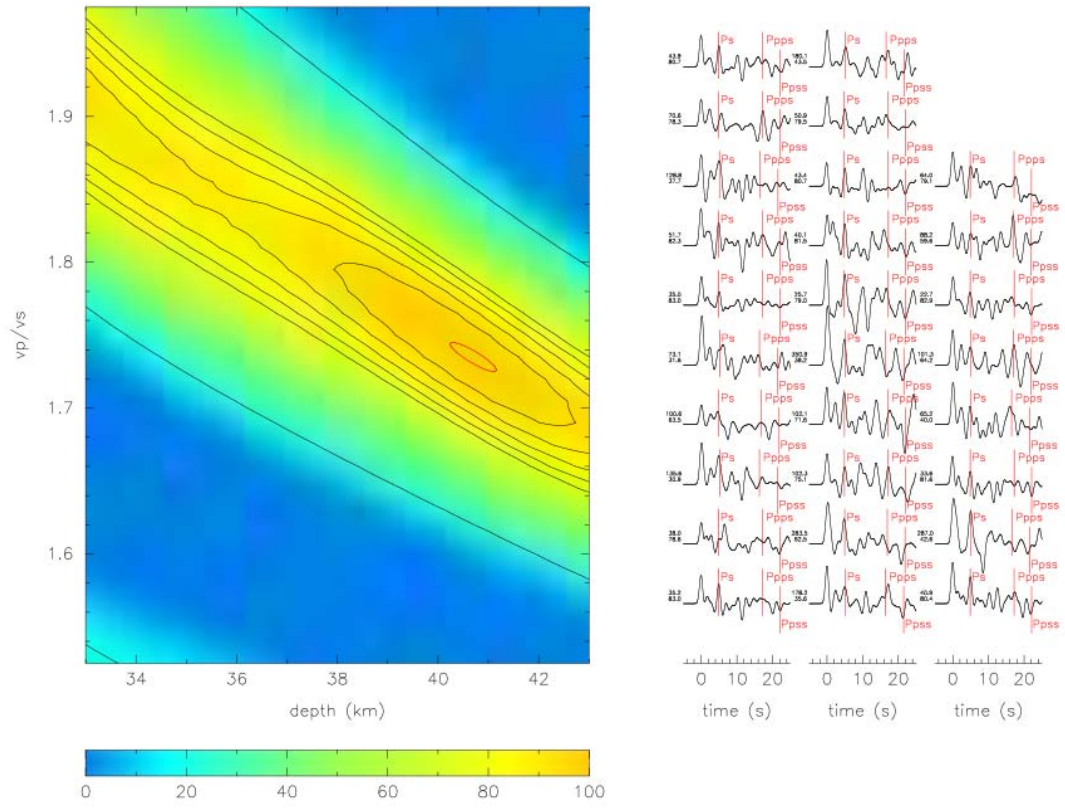

Figure 4.15. The $H-\kappa$ stacking result for SALD station.

($V_P = 6.3\,\mathrm{Km/s}$ $h = 40.7 \pm 0.9$ $V_P/V_S = 1.74 \pm 0.02$ $corr = -89.0\%$)

4.2.3. East – West profile: ÇELTİLCİ (CLTK) station

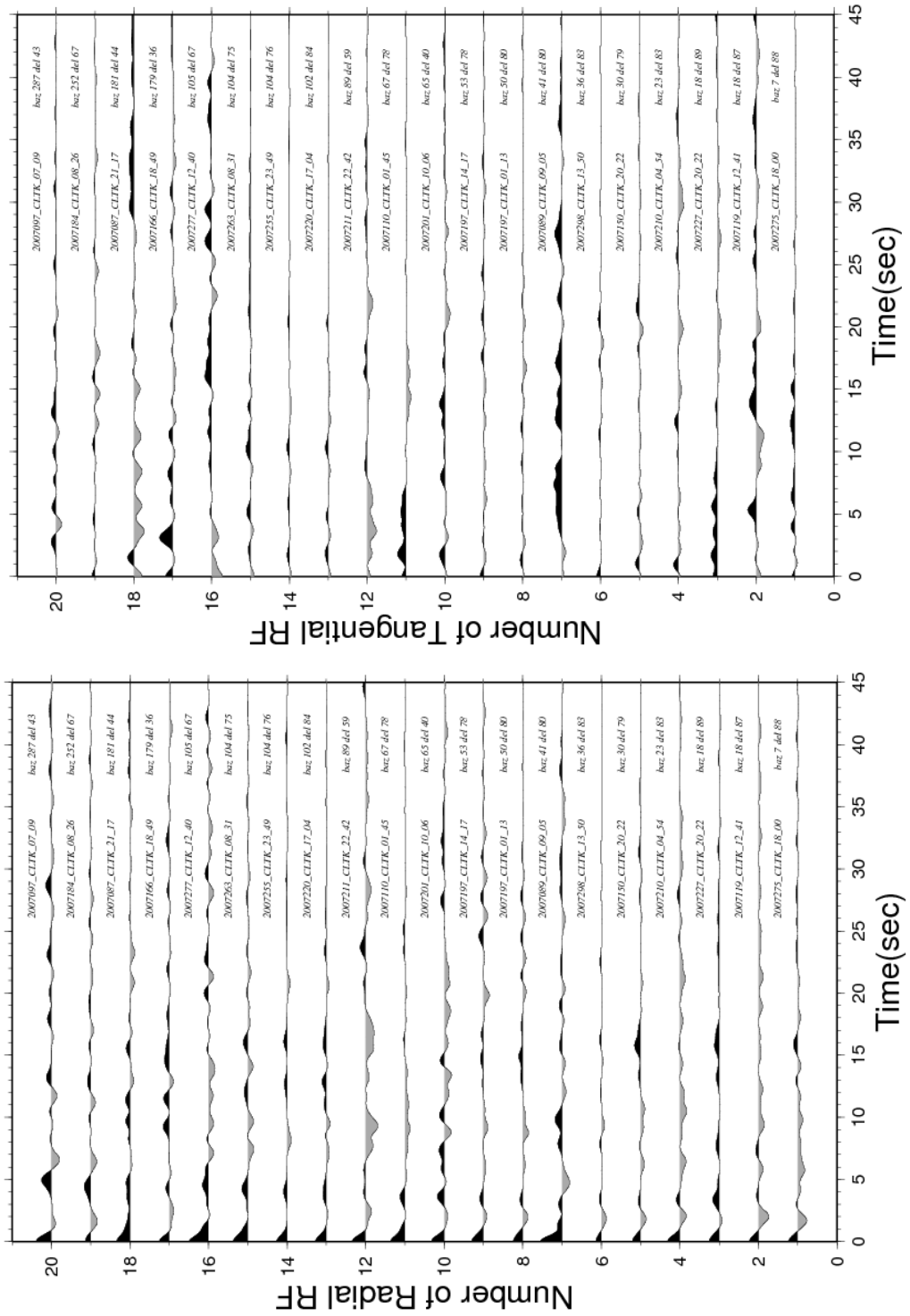

Figure 4.16. The radial and tangential RFs for CLTK station.

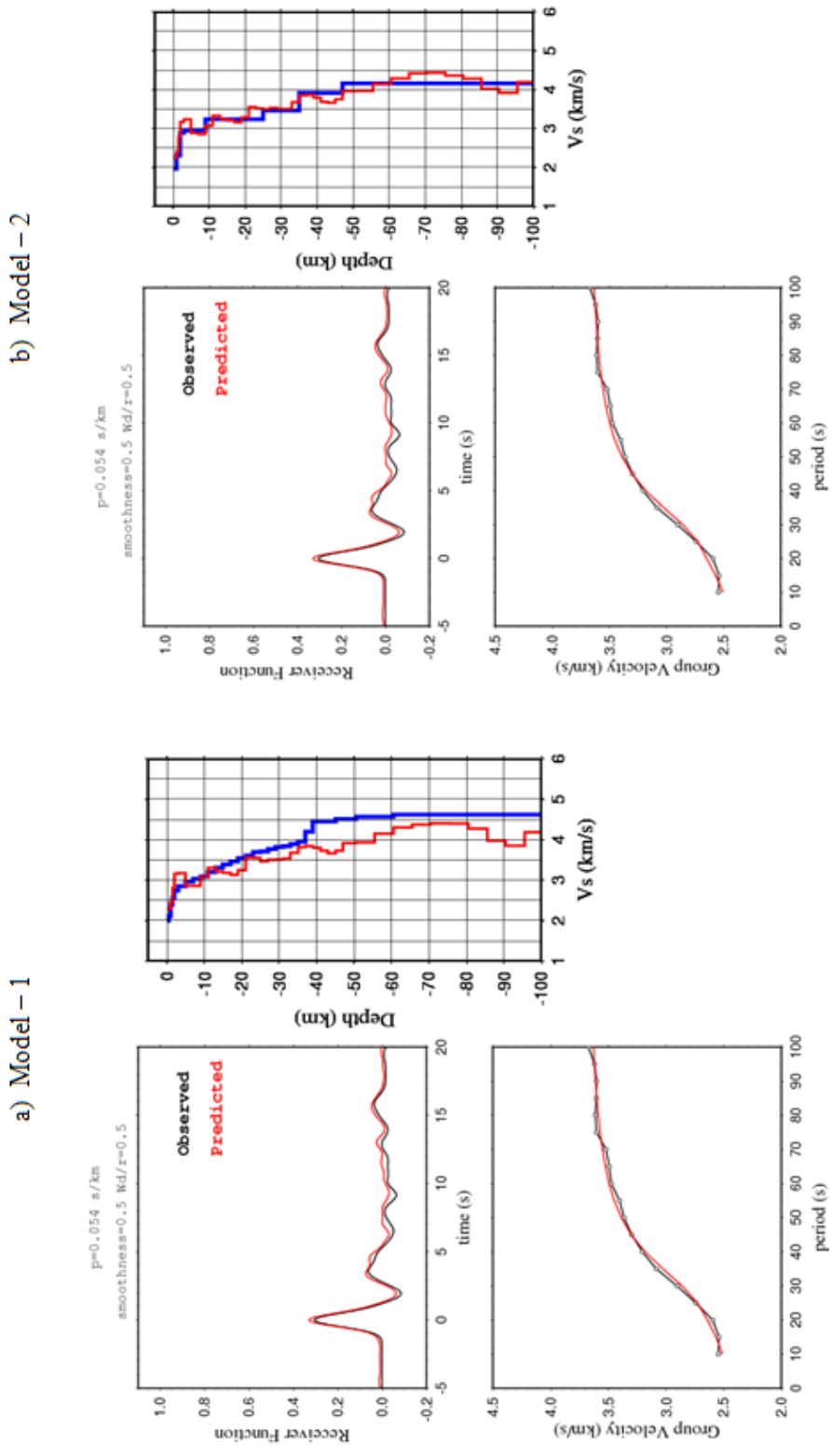

Figure 4.17. Joint inversion of RFs and surface waves with two different initial models beneath the CLTK station.

Table 4.5. Velocity structure beneath the CLTK station.

a) The average velocity results using Model – 1.

Layers	Thickness (km)	Vp (km/s)	Vs (km/s)	ρ (g/cm^3)
1	2,00	4,30	2,46	2,15
2	13,00	5,41	3,09	2,50
3	14,00	5,91	3,38	2,66
4	8,00	6,36	3,63	2,80
5	6,00	6,63	3,79	2,89
6	57,50	7,16	4,09	3,06

b) The average velocity results using Model – 2.

Layers	Thickness (km)	Vp (km/s)	Vs (km/s)	ρ (g/cm^3)
1	2,00	4,20	2,42	2,11
2	13,00	5,39	3,11	2,50
3	14,00	5,88	3,39	2,65
4	8,00	6,29	3,63	2,78
5	6,00	6,56	3,78	2,87
6	57,50	7,12	4,11	3,05

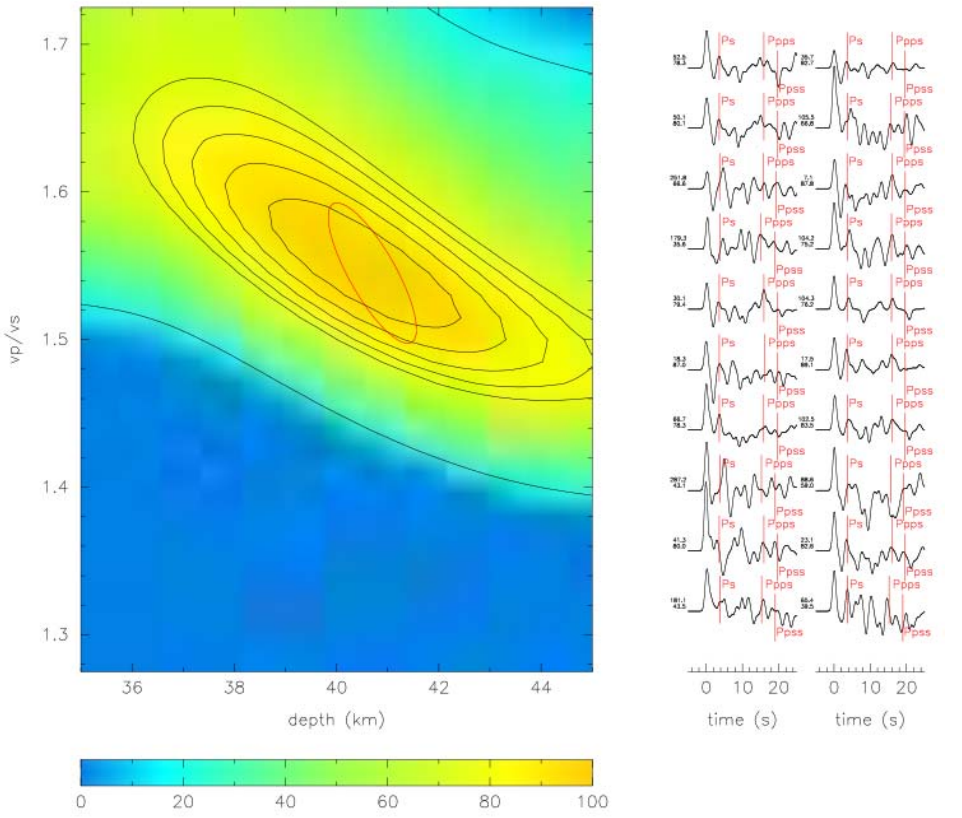

Figure 4.18. The $H-\kappa$ stacking result for CLTK station.

($V_P = 6.3$ Km/s $h = 40.7 \pm 1.7$ $V_P/V_S = 1.54 \pm 0.10$ $corr = -80.0\%$)

4.2.4. East – West profile: SÜTÇÜLER (SUTC) station

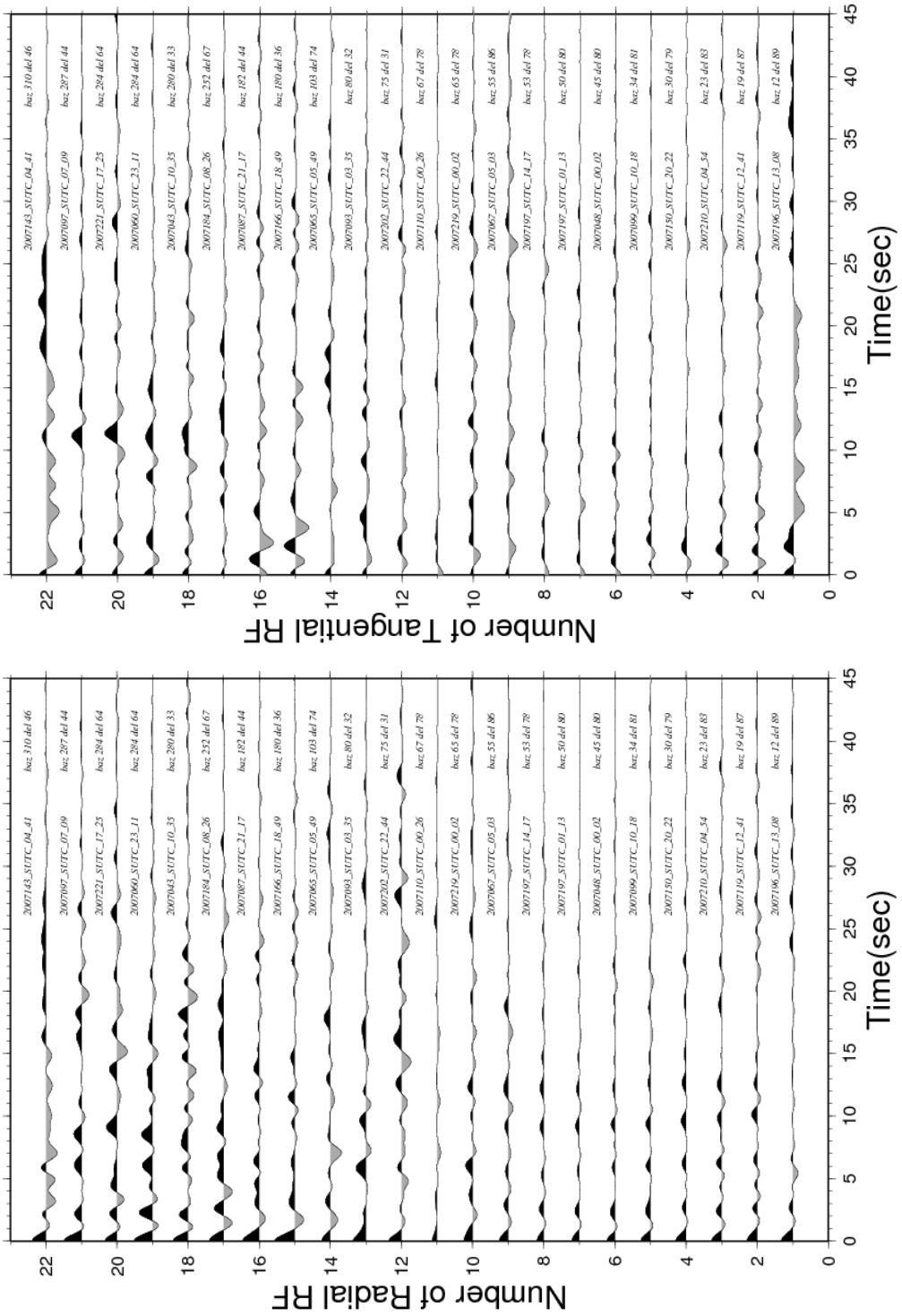

Figure 4.19. The radial and tangential RFs for SUTC station.

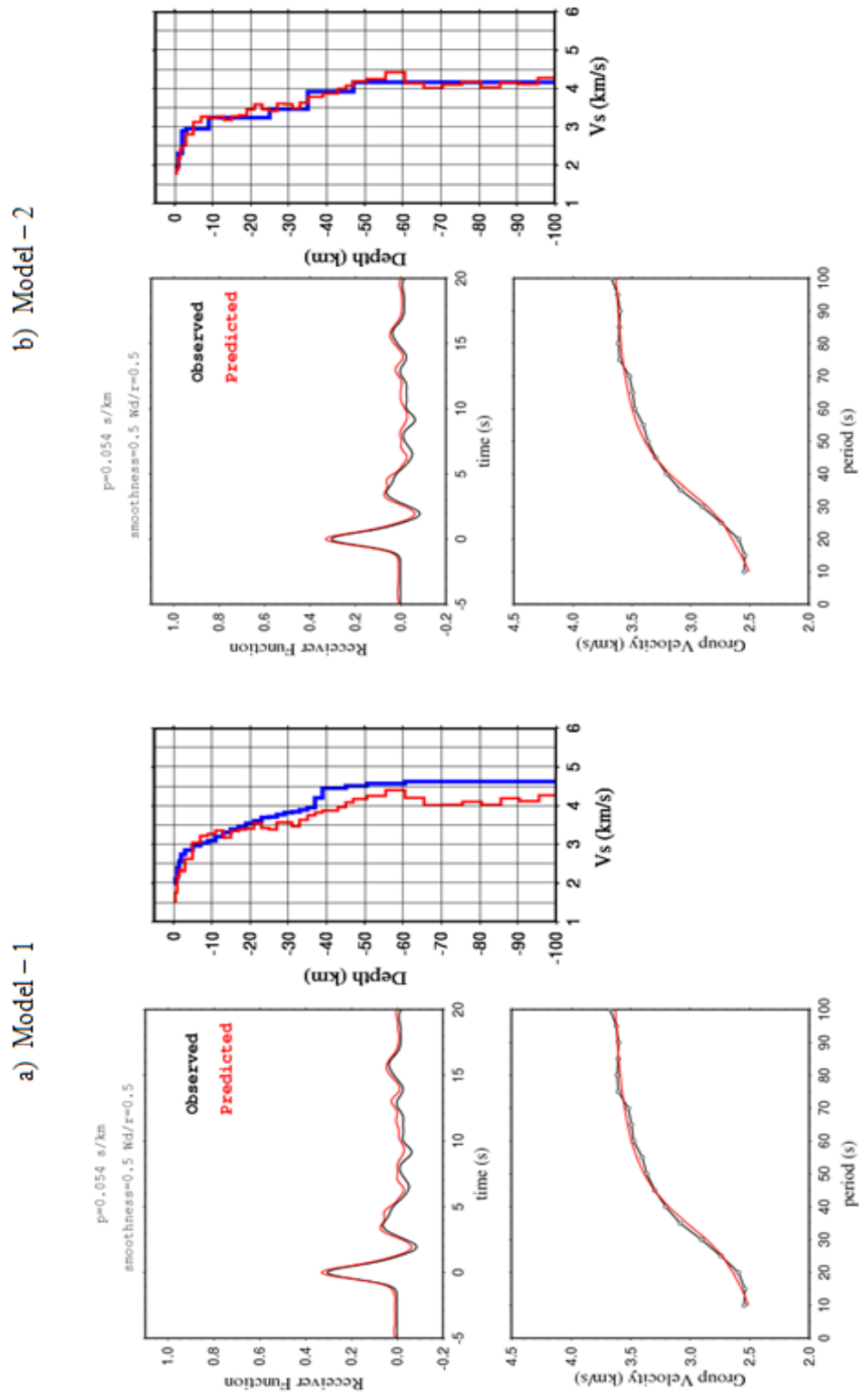

Figure 4.20. Joint inversion of RFs and surface waves with two different initial models beneath the SUTC station.

Table 4.6. Velocity structure beneath the SUTC station.

a) The average velocity results using Model – 1.

Layers	Thickness (km)	Vp (km/s)	Vs (km/s)	ρ (g/cm^3)
1	2,00	3,41	1,95	1,86
2	13,00	5,25	3,00	2,45
3	14,00	6,01	3,44	2,69
4	8,00	6,30	3,60	2,79
5	6,00	6,75	3,86	2,93
6	57,50	7,25	4,14	3,09

b) The average velocity results using Model – 2.

Layers	Thickness (km)	Vp (km/s)	Vs (km/s)	ρ (g/cm^3)
1	2,00	3,58	2,06	1,92
2	13,00	5,29	3,05	2,46
3	14,00	5,96	3,44	2,68
4	8,00	6,28	3,62	2,78
5	6,00	6,66	3,84	2,90
6	57,50	7,18	4,14	3,07

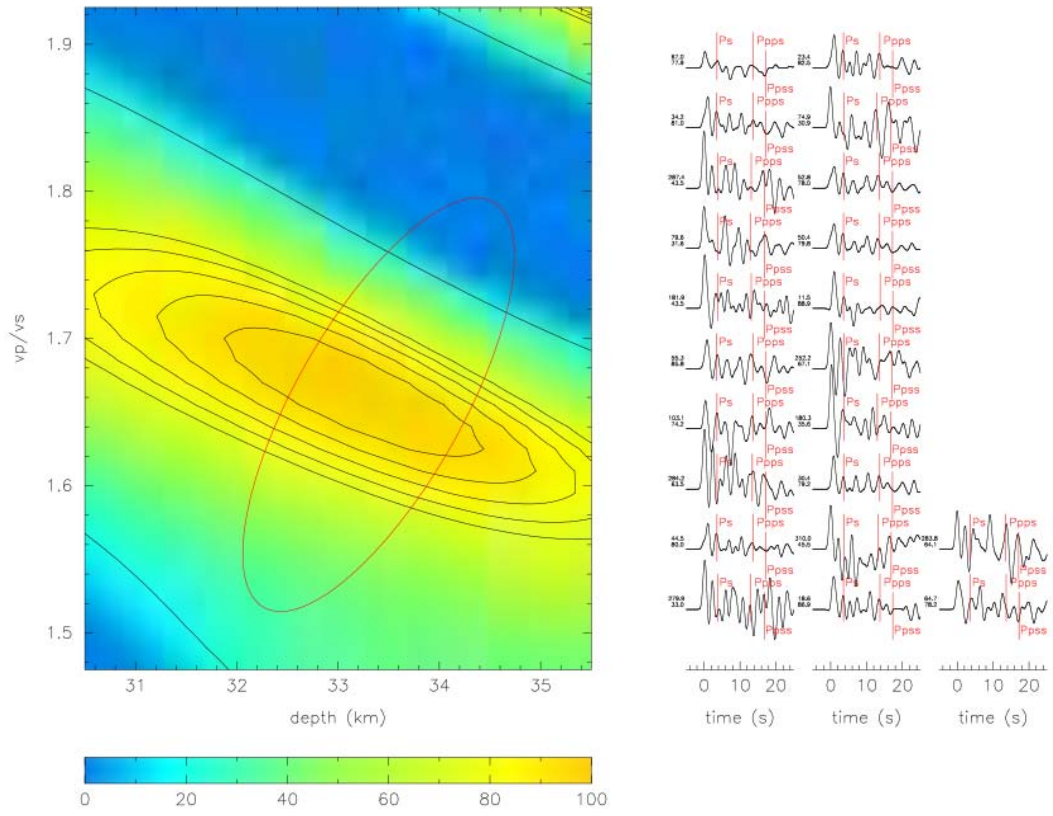

Figure 4.21. The $H-\kappa$ stacking result for SUTC station.

($V_P = 6.3\,\mathrm{Km/s}$ $h = 33.4 \pm 2.7$ $V_P/V_S = 1.66 \pm 0.28$ $corr = 72.2\%$)

4.2.5. East – West profile: HUĞLU (HULU) station

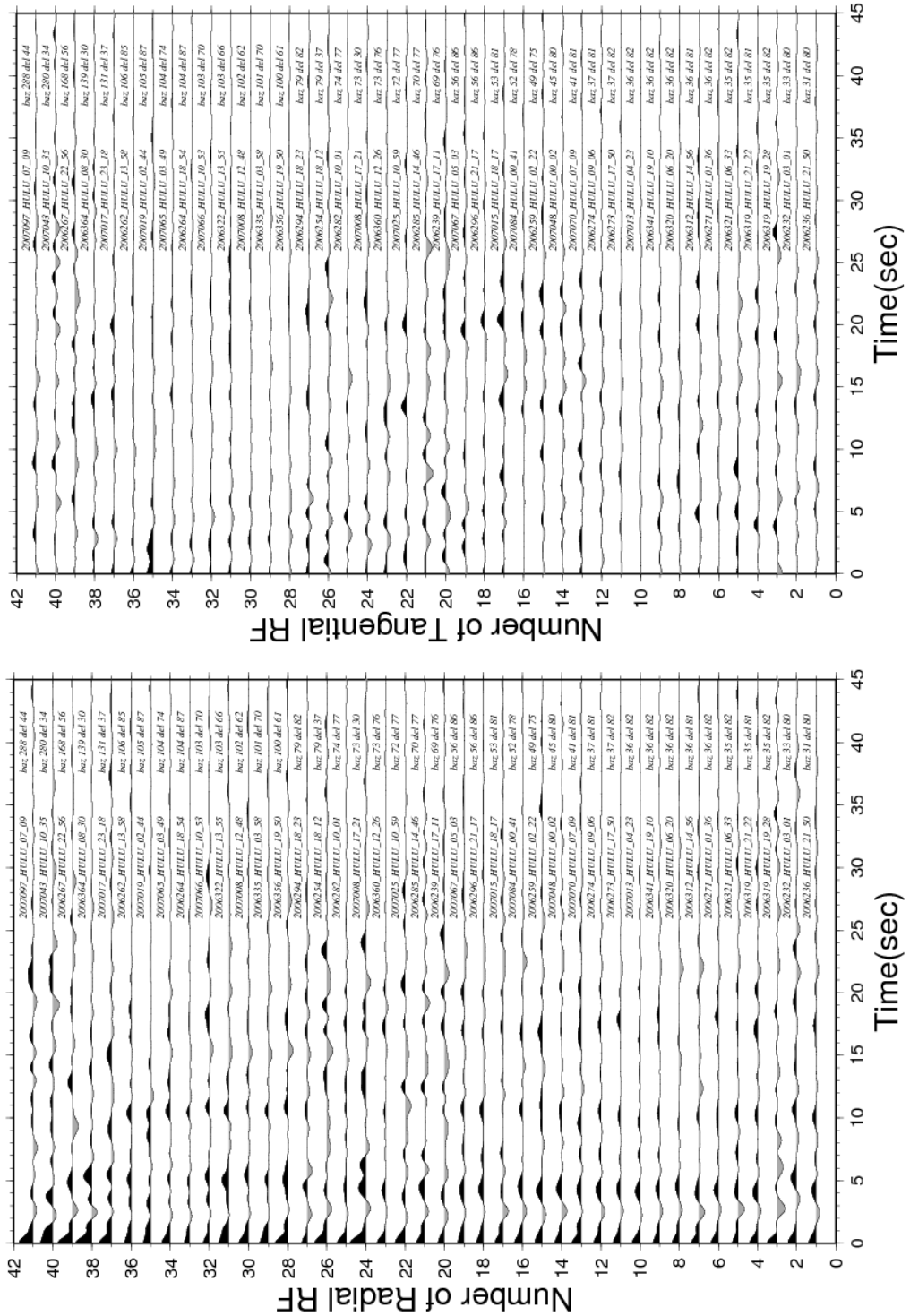

Figure 4.22. The radial and tangential RFs for HULU station.

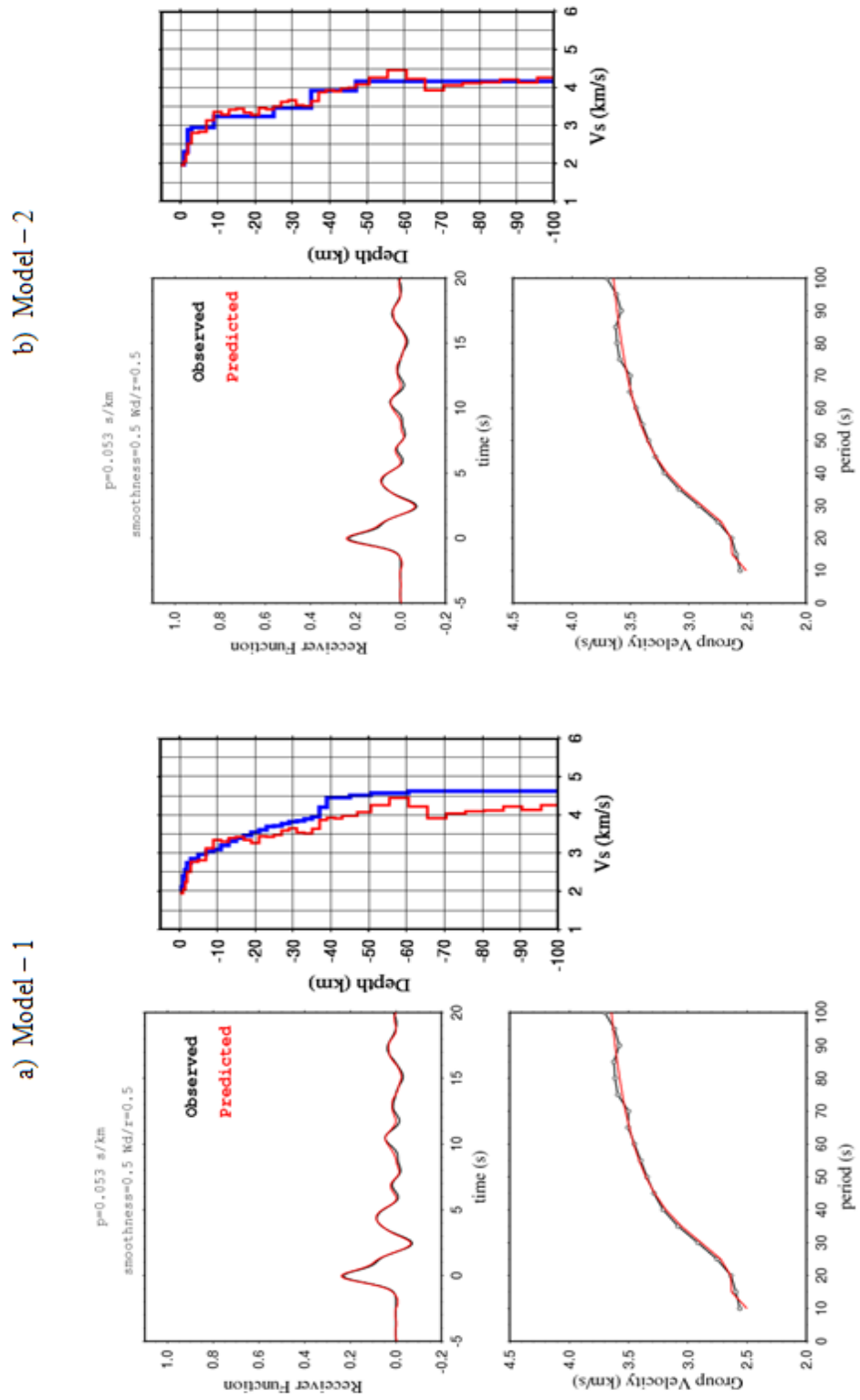

Figure 4.23. Joint inversion of RFs and surface waves with two different initial models beneath the HULU station.

Table 4.7. Velocity structure beneath the HULU station.

a) The average velocity results using Model – 1.

Layers	Thickness (km)	Vp (km/s)	Vs (km/s)	ρ (g/cm^3)
1	2,00	3,58	2,04	1,91
2	13,00	5,31	3,03	2,47
3	14,00	5,99	3,42	2,69
4	8,00	6,26	3,58	2,77
5	6,00	6,82	3,90	2,95
6	57,50	7,23	4,13	3,08

b) The average velocity results using Model – 2.

Layers	Thickness (km)	Vp (km/s)	Vs (km/s)	ρ (g/cm^3)
1	2,00	3,55	2,05	1,91
2	13,00	5,29	3,05	2,46
3	14,00	5,95	3,43	2,67
4	8,00	6,22	3,59	2,76
5	6,00	6,76	3,89	2,93
6	57,50	7,18	4,14	3,07

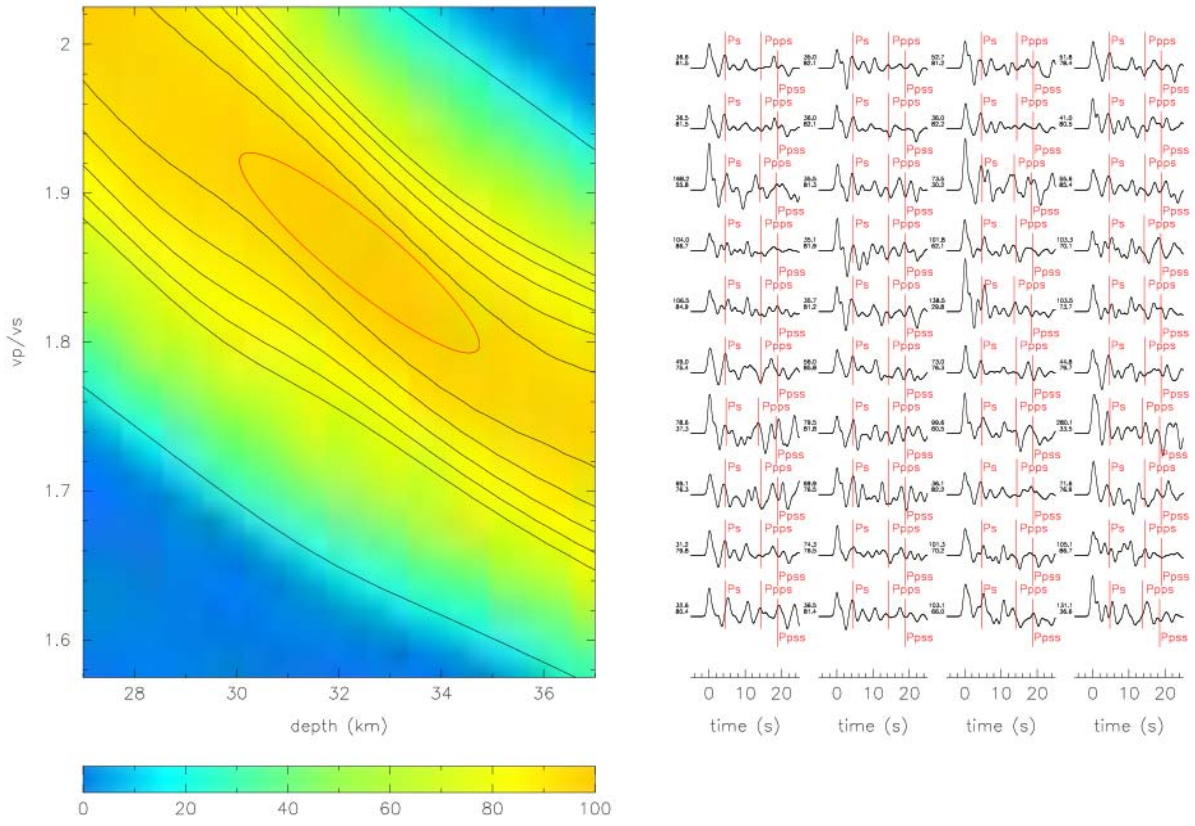

Figure 4.24. The $H-\kappa$ stacking result for HULU station.

($V_P = 6.3$ Km/s $h = 32.4 \pm 4.7$ $V_P/V_S = 1.86 \pm 0.13$ $corr = -91.4\%$)

4.2.6. East – West profile: AKÖREN (AKRN) station

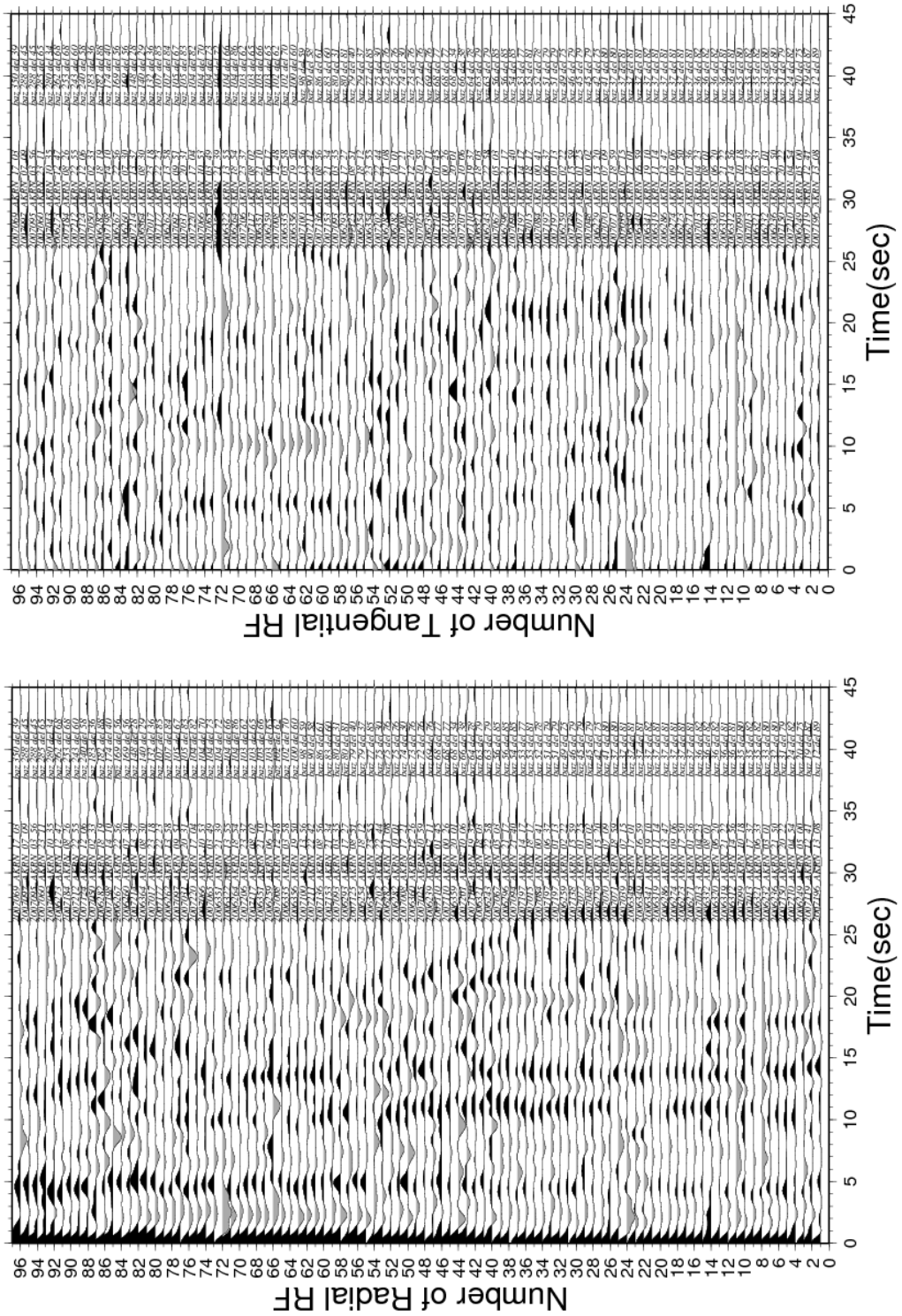

Figure 4.25. The radial and tangential RFs for AKRN station.

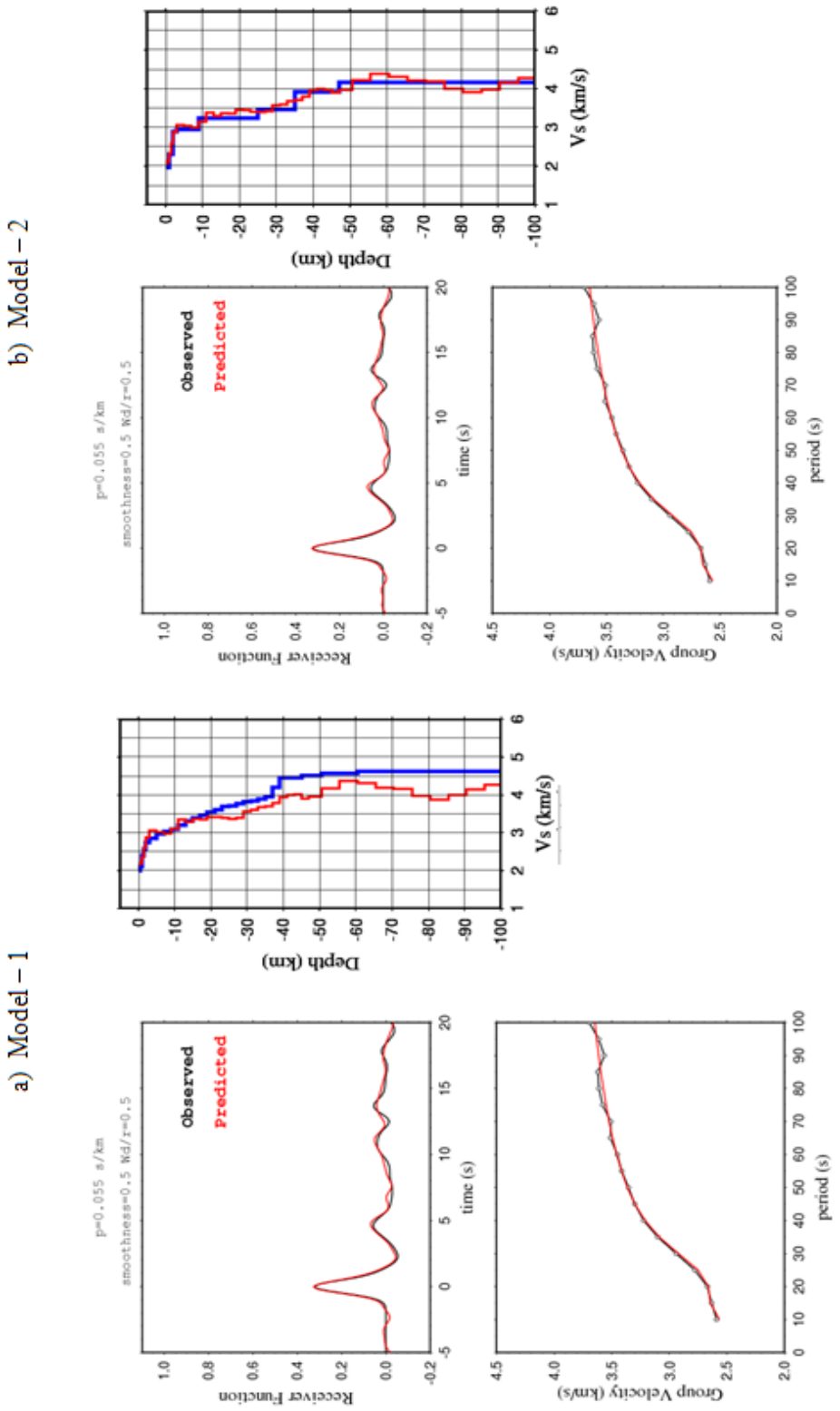

Figure 4.26. Joint inversion of RFs and surface waves with two different initial models beneath the AKRN station.

Table 4.8. Velocity structure beneath the AKRN station.

a) The average velocity results using Model – 1.

Layers	Thickness (km)	Vp (km/s)	Vs (km/s)	ρ (g/cm^3)
1	2,00	4,08	2,33	2,07
2	13,00	5,42	3,09	2,50
3	14,00	5,92	3,39	2,67
4	8,00	6,36	3,63	2,80
5	6,00	6,84	3,91	2,96
6	57,50	7,18	4,10	3,07

b) The average velocity results using Model – 2.

Layers	Thickness (km)	Vp (km/s)	Vs (km/s)	ρ (g/cm^3)
1	2,00	3,96	2,28	2,04
2	13,00	5,39	3,11	2,50
3	14,00	5,90	3,40	2,66
4	8,00	6,30	3,63	2,79
5	6,00	6,79	3,91	2,94
6	57,50	7,12	4,11	3,05

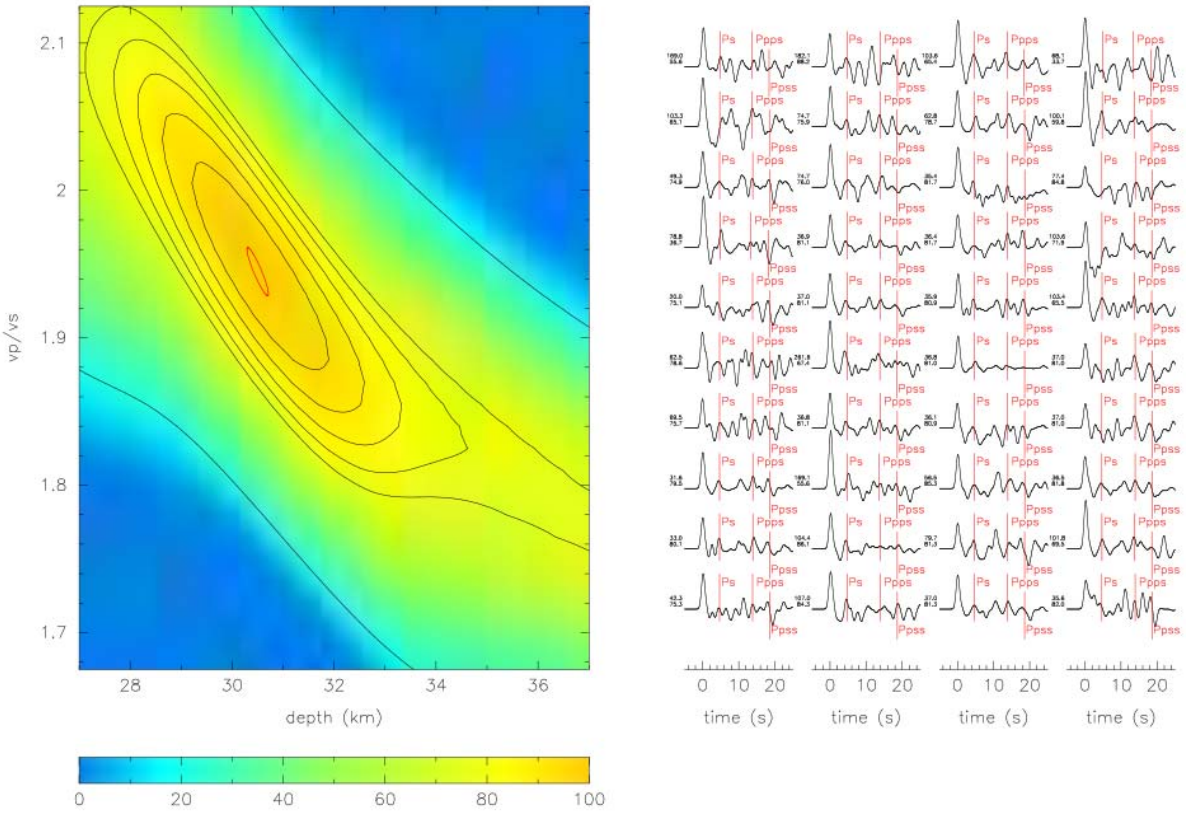

Figure 4.27. The $H-\kappa$ stacking result for AKRN station.

($V_P = 6.3$ Km/s $h = 30.5 \pm 0.4$ $V_P / V_S = 1.94 \pm 0.03$ $corr = -92.0\%$)

4.2.7. North – South profile: AFYON (AFYN) station

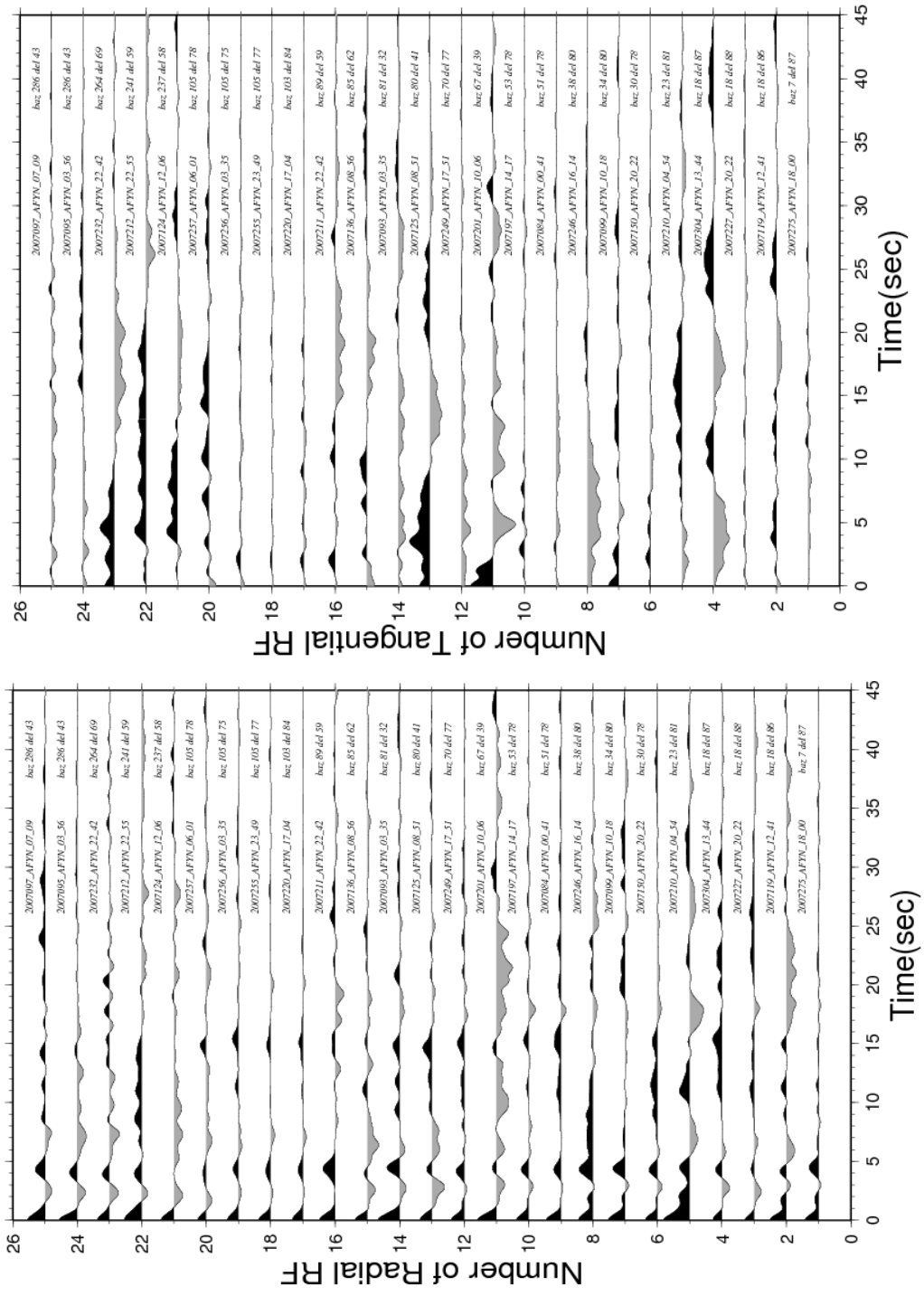

Figure 4.28. The radial and tangential RFs for AFYN station.

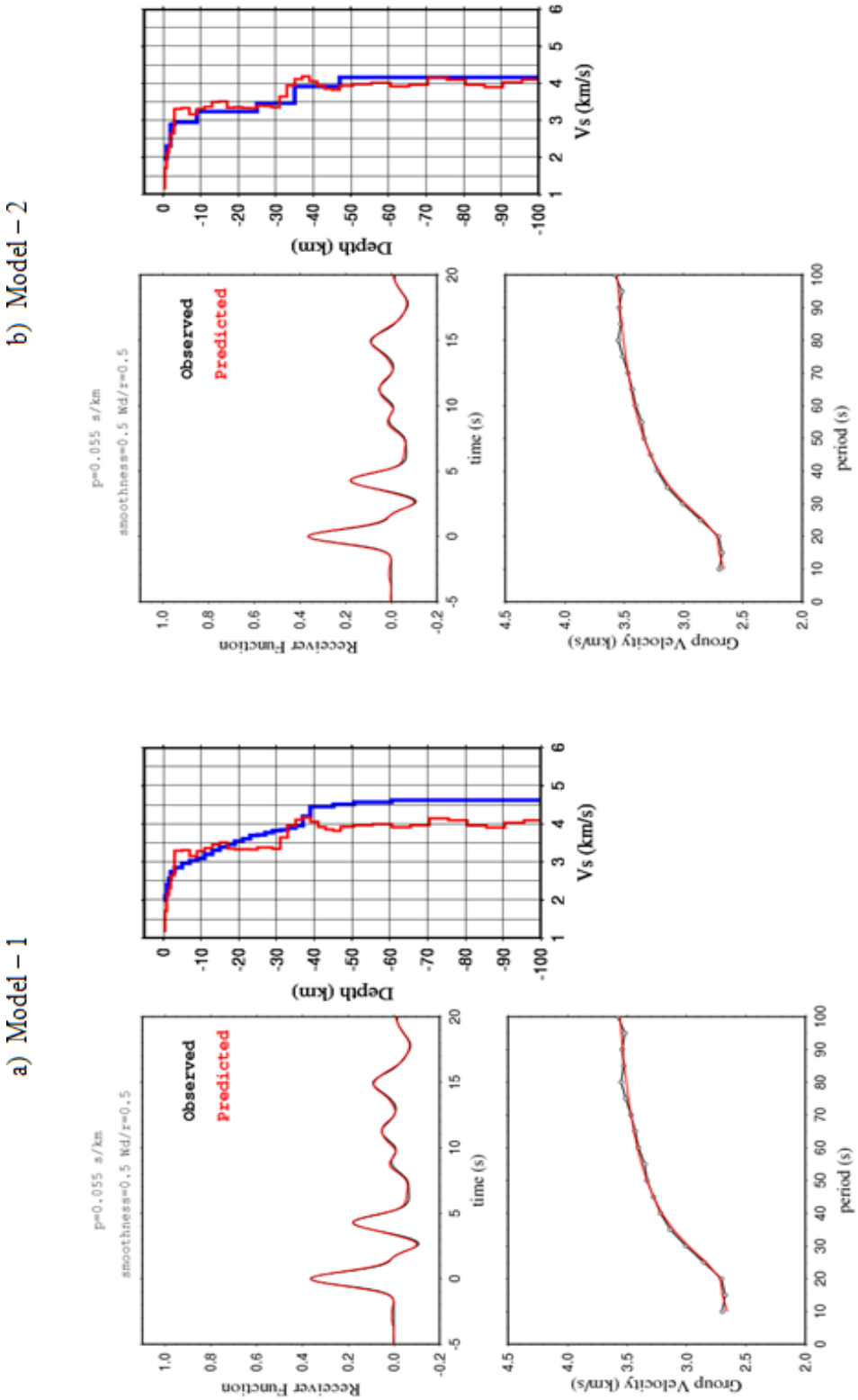

Figure 4.29. Joint inversion of RFs and surface waves with two different initial models beneath the AFYN station.

Table 4.9. Velocity structure beneath the AFYN station.

a) The average velocity results using Model – 1.

Layers	Thickness (km)	Vp (km/s)	Vs (km/s)	ρ (g/cm^3)
1	2,00	3,21	1,83	1,80
2	13,00	5,63	3,21	2,57
3	14,00	5,90	3,37	2,66
4	8,00	6,58	3,76	2,88
5	6,00	7,08	4,05	3,04
6	57,50	6,95	3,97	3,00

b) The average velocity results using Model – 2.

Layers	Thickness (km)	Vp (km/s)	Vs (km/s)	ρ (g/cm^3)
1	2,00	3,15	1,82	1,78
2	13,00	5,60	3,23	2,56
3	14,00	5,86	3,38	2,64
4	8,00	6,52	3,76	2,86
5	6,00	7,04	4,06	3,02
6	57,50	6,90	3,98	2,98

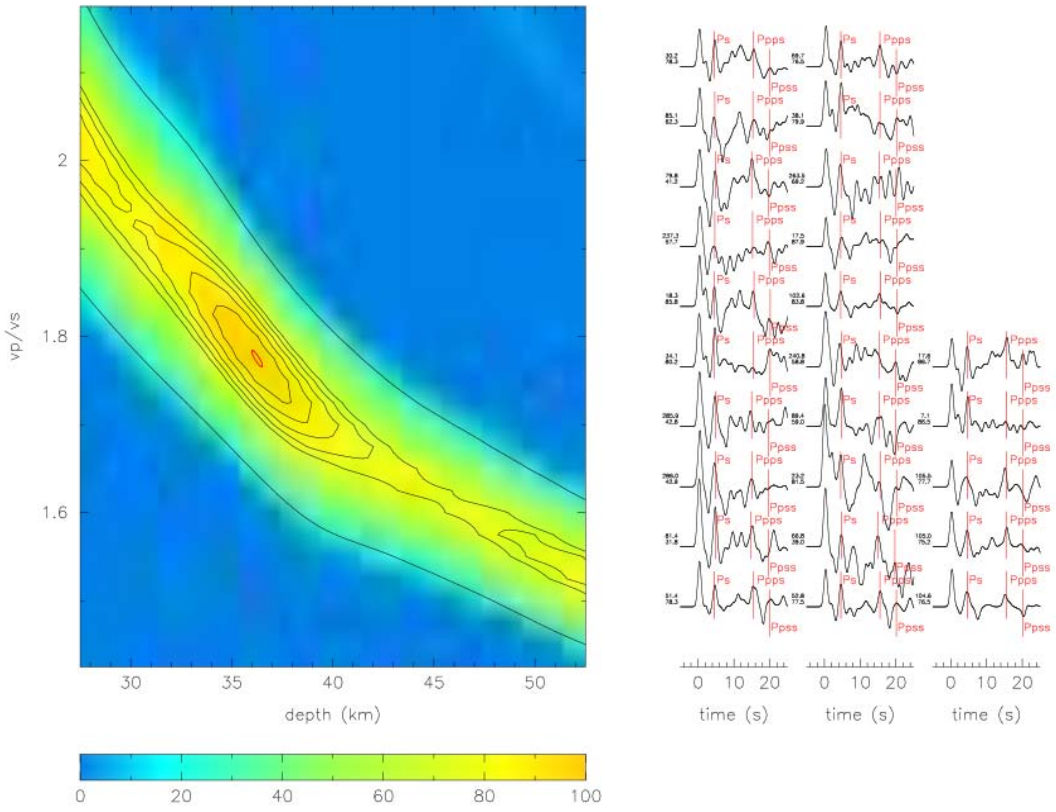

Figure 4.30. The $H-\kappa$ stacking result for AFYN station.

($V_P = 6.3\,\mathrm{Km/s}$ $h = 36.2 \pm 0.5$ $V_P/V_S = 1.77 \pm 0.02$ $corr = -87.9\%$)

4.2.8. North – South profile: ŞUHUT (SHUT) station

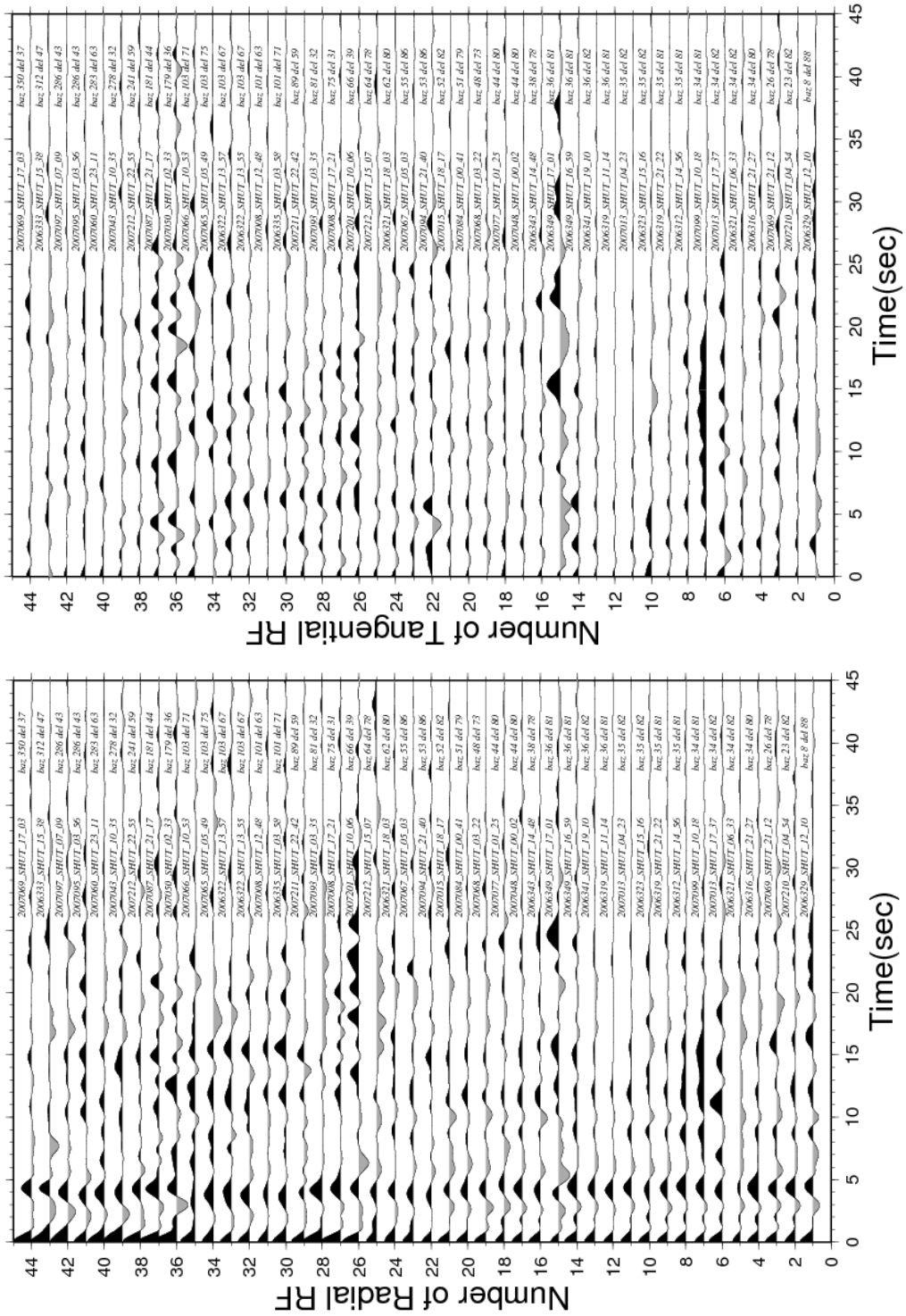

Figure 4.31. The radial and tangential RFs for SHUT station.

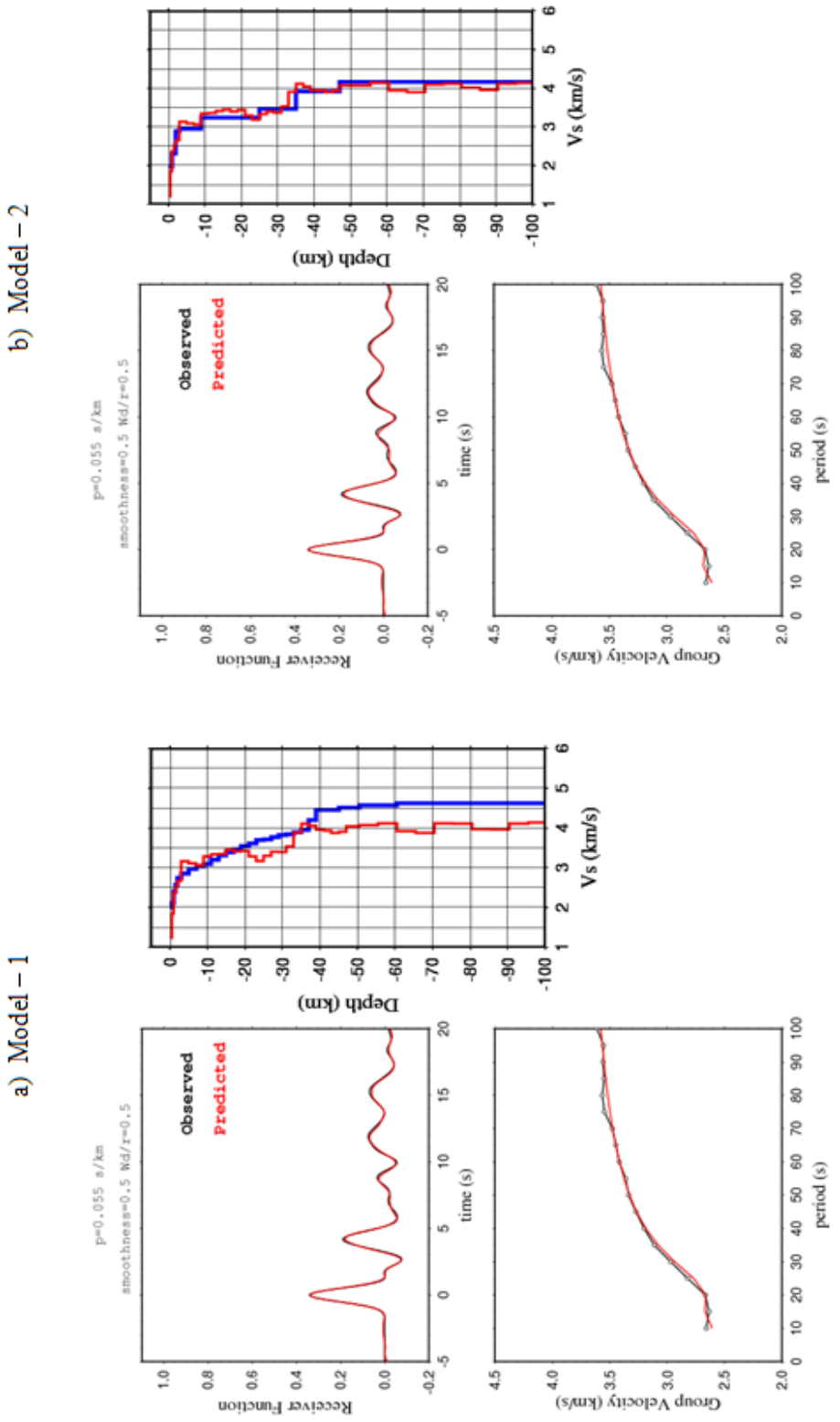

Figure 4.32. Joint inversion of RFs and surface waves with two different initial models beneath the SHUT station.

Table 4.10. Velocity structure beneath the SHUT station.

a) The average velocity results using Model – 1.

Layers	Thickness (km)	Vp (km/s)	Vs (km/s)	ρ (g/cm^3)
1	2,00	3,49	1,99	1,89
2	13,00	5,49	3,14	2,53
3	14,00	5,86	3,35	2,64
4	8,00	6,52	3,73	2,86
5	6,00	6,96	3,98	3,00
6	57,50	7,04	4,02	3,02

b) The average velocity results using Model – 2.

Layers	Thickness (km)	Vp (km/s)	Vs (km/s)	ρ (g/cm^3)
1	2,00	3,45	1,99	1,87
2	13,00	5,46	3,15	2,52
3	14,00	5,81	3,35	2,63
4	8,00	6,46	3,73	2,84
5	6,00	6,89	3,97	2,98
6	57,50	6,98	4,03	3,00

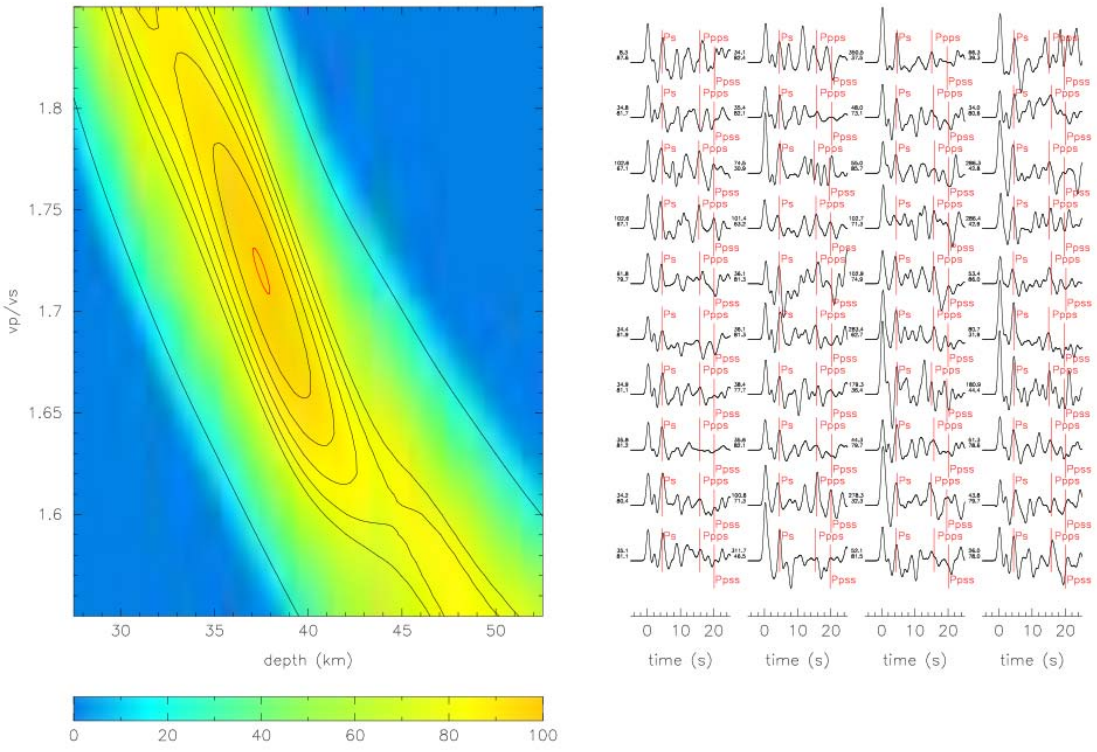

Figure 4.33. The result of $H-\kappa$ stacking result for SHUT station.

($V_P = 6.3\,\mathrm{Km/s}$ $h = 37.5 \pm 0.9$ $V_P / V_S = 1.72 \pm 0.02$ $corr = -87.9\%$)

4.2.9. North – South profile: HAYDARLI (HYDR) station

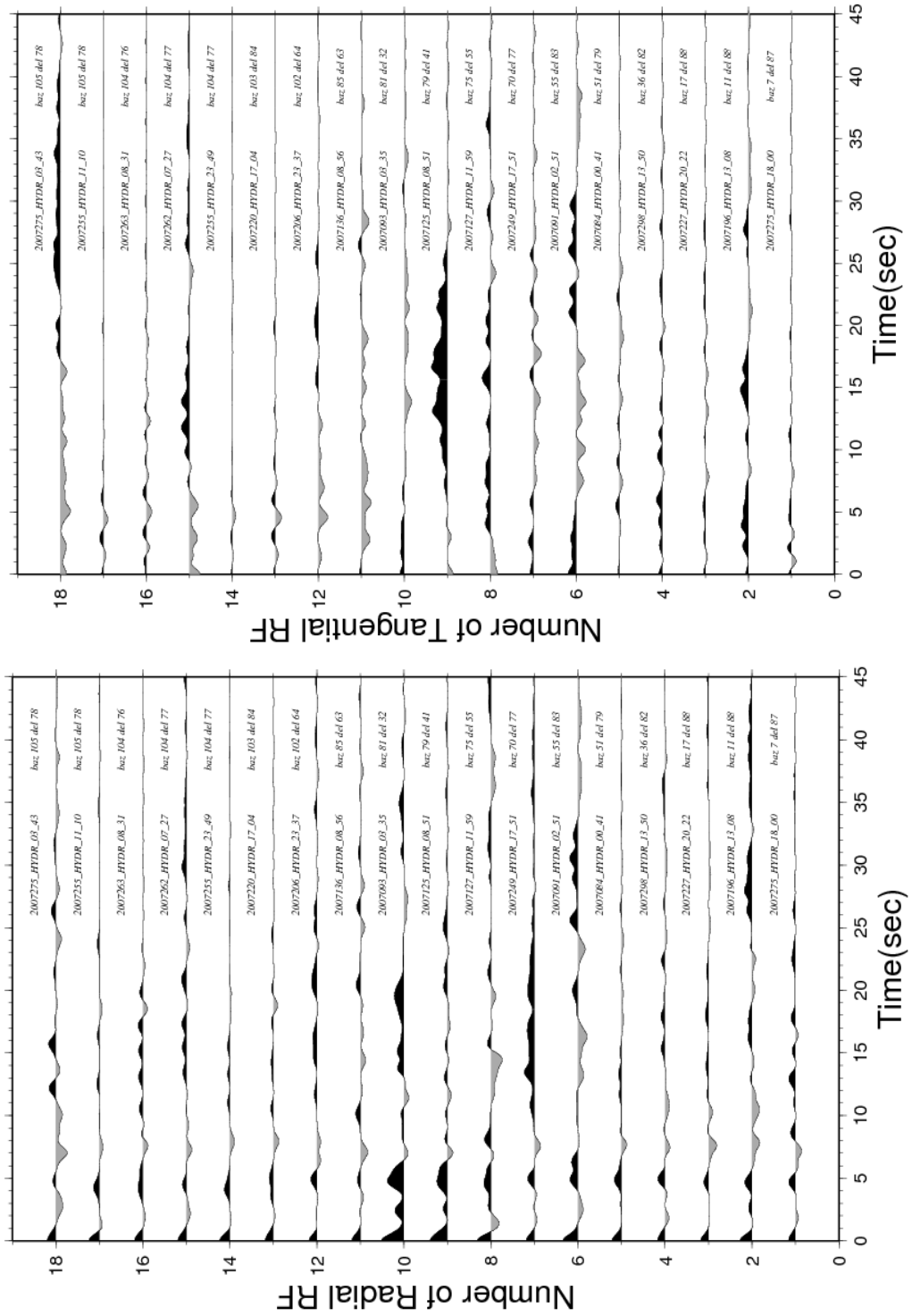

Figure 4.34. The radial and tangential RFs for HYDR station.

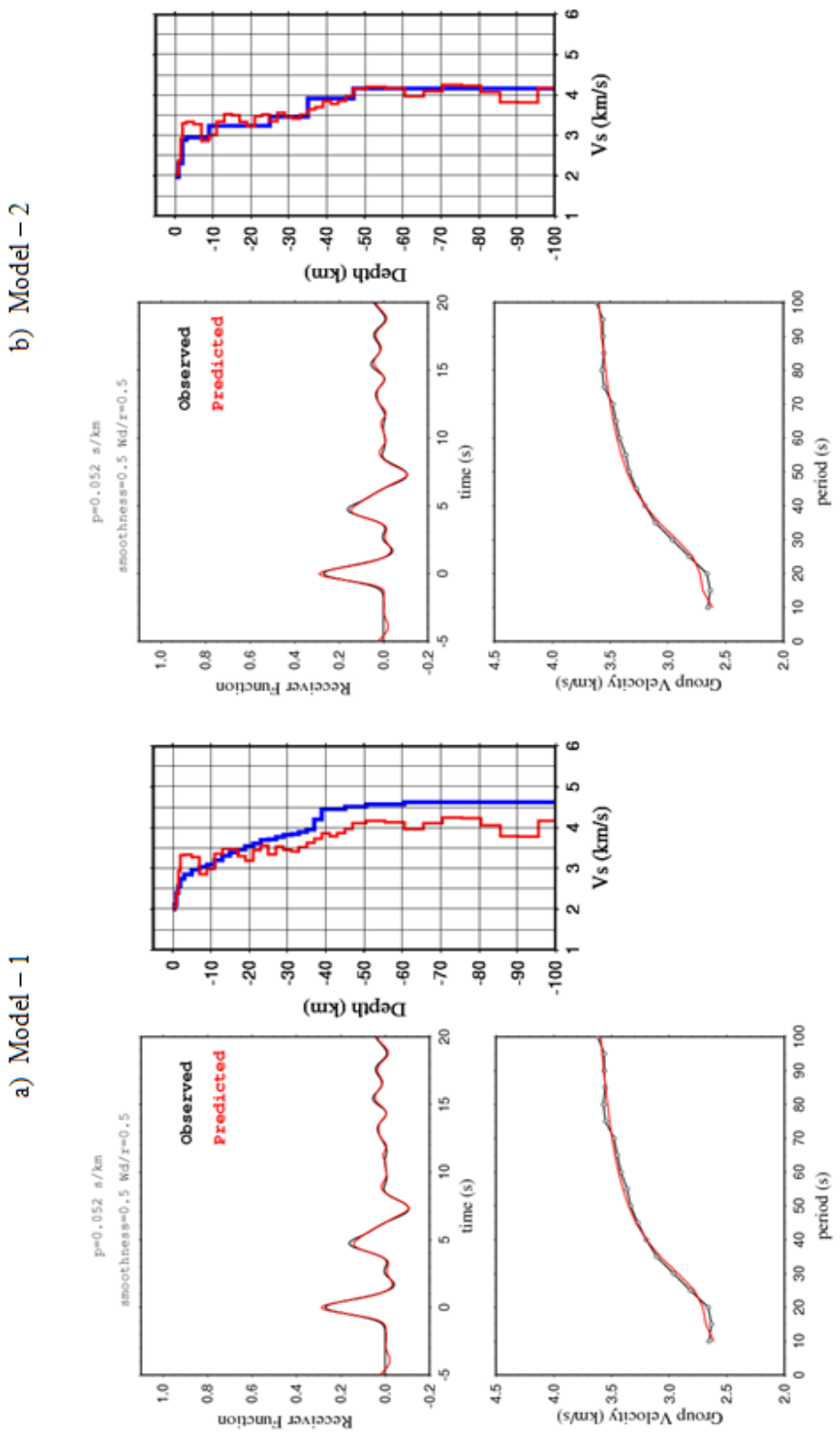

Figure 4.35. Joint inversion of RFs and surface waves with two different initial models beneath the HYDR station.

Table 4.11. Velocity structure beneath the HYDR station.

a) The average velocity results using Model – 1.

Layers	Thickness (km)	Vp (km/s)	Vs (km/s)	ρ (g/cm^3)
1	2,00	4,12	2,35	2,09
2	13,00	5,65	3,23	2,58
3	14,00	5,96	3,40	2,68
4	8,00	6,13	3,50	2,73
5	6,00	6,62	3,79	2,89
6	57,50	7,08	4,04	3,04

b) The average velocity results using Model – 2.

Layers	Thickness (km)	Vp (km/s)	Vs (km/s)	ρ (g/cm^3)
1	2,00	4,06	2,33	2,07
2	13,00	5,61	3,24	2,57
3	14,00	5,93	3,42	2,67
4	8,00	6,09	3,51	2,72
5	6,00	6,55	3,77	2,86
6	57,50	7,04	4,06	3,02

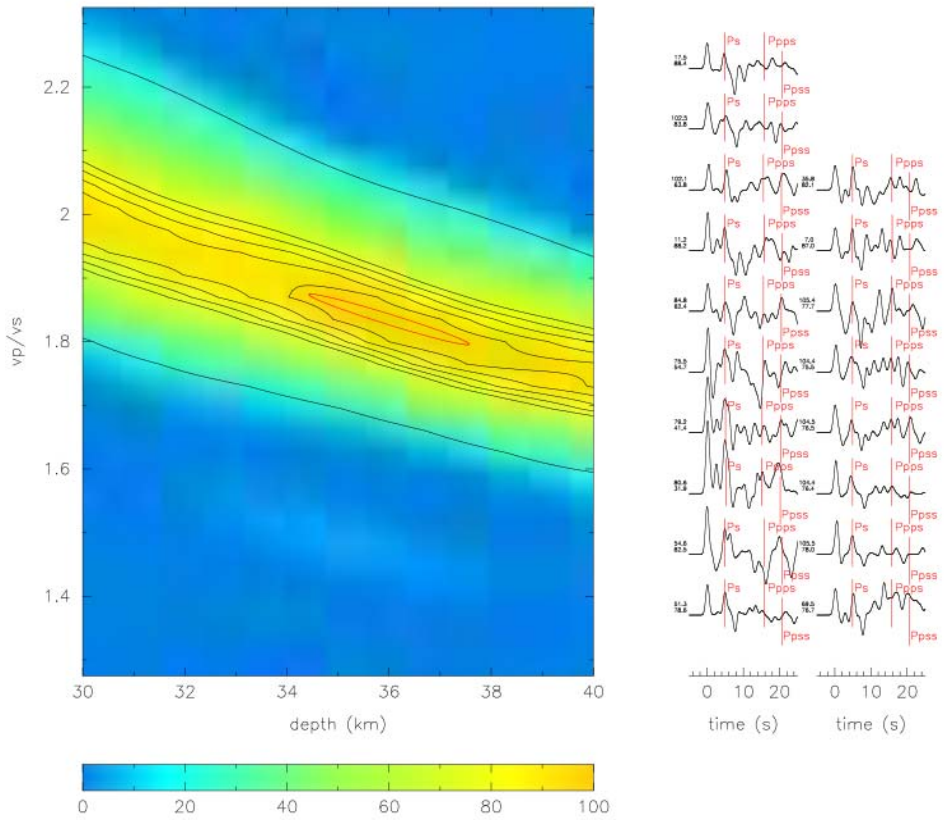

Figure 4.36. The $H-\kappa$ stacking result for HYDR station.

($V_P = 6.3$ Km/s $h = 36.0 \pm 3.1$ $V_P / V_S = 1.83 \pm 0.08$ $corr = -97.6\%$)

4.2.10. North – South profile: ULUBORLU (ULUB) station

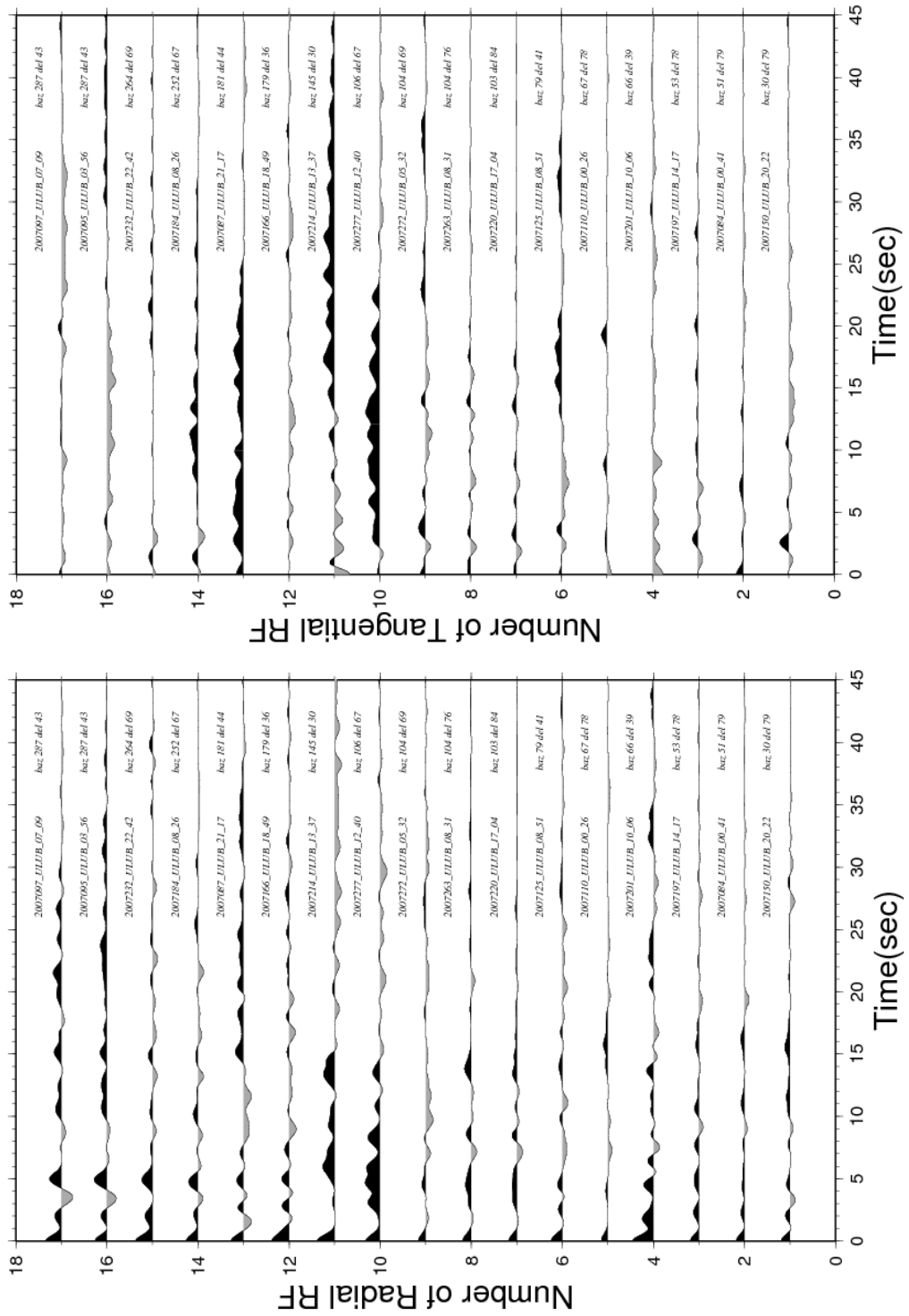

Figure 4.37. The radial and tangential RFs for ULUB station.

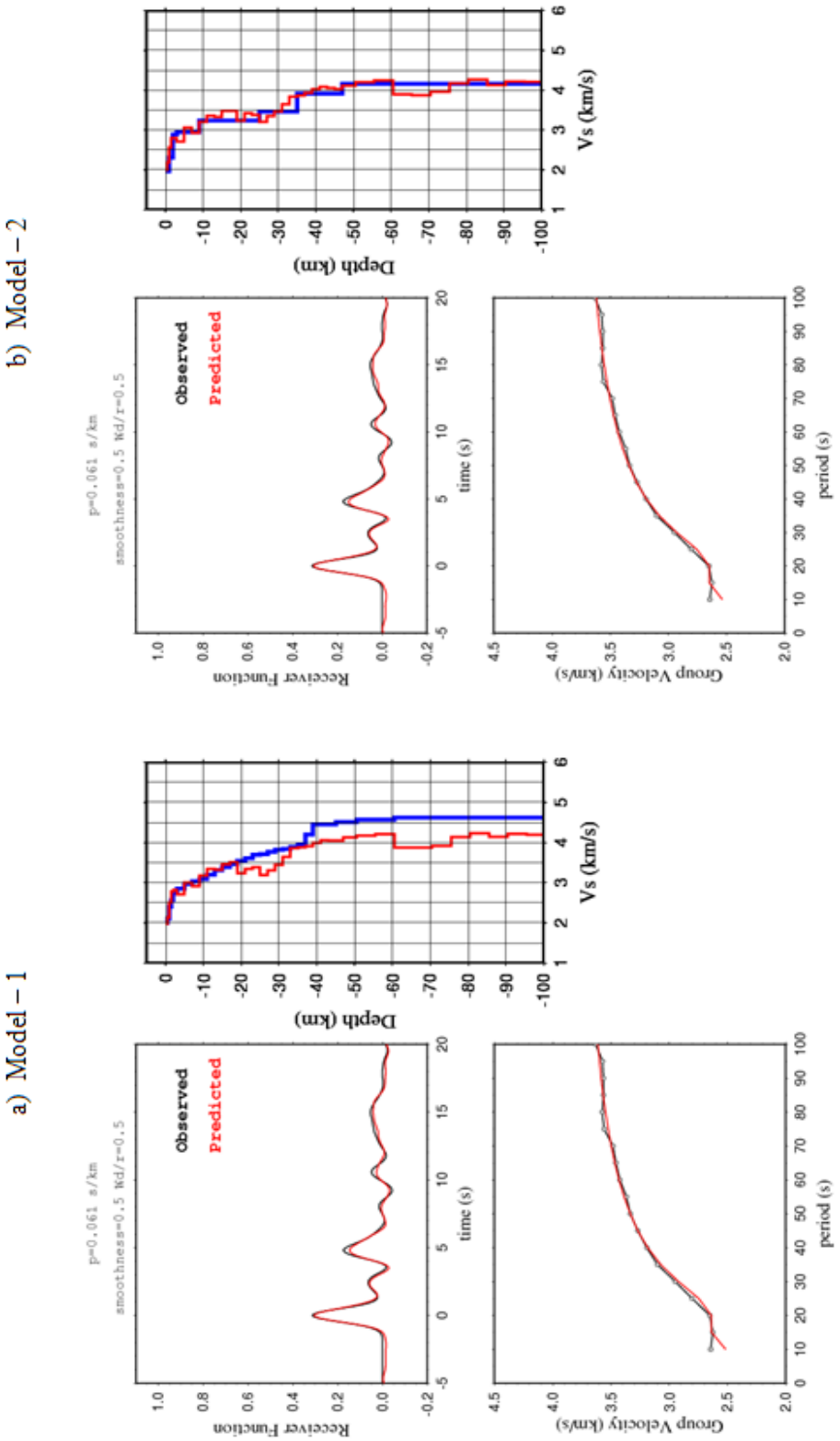

Figure 4.38. Joint inversion of RFs and surface waves with two different initial models beneath the ULUB station.

Table 4.12. Velocity structure beneath the ULUB station.

a) The average velocity results using Model – 1.

Layers	Thickness (km)	Vp (km/s)	Vs (km/s)	ρ (g/cm^3)
1	2,00	4,11	2,35	2,09
2	13,00	5,32	3,04	2,47
3	14,00	5,86	3,35	2,64
4	8,00	6,49	3,71	2,85
5	6,00	6,97	3,99	3,00
6	57,50	7,17	4,09	3,06

b) The average velocity results using Model – 2.

Layers	Thickness (km)	Vp (km/s)	Vs (km/s)	ρ (g/cm^3)
1	2,00	4,14	2,38	2,09
2	13,00	5,29	3,05	2,46
3	14,00	5,84	3,37	2,64
4	8,00	6,42	3,70	2,83
5	6,00	6,96	4,01	3,00
6	57,50	7,12	4,10	3,05

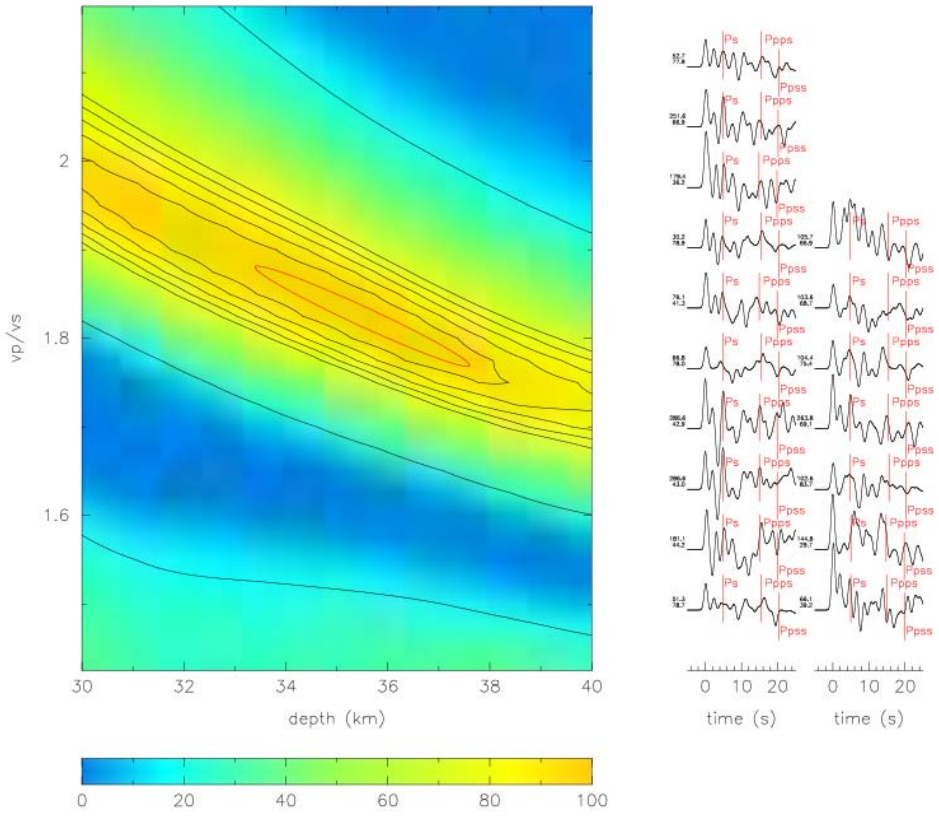

Figure 4.39. The of $H-\kappa$ stacking result for ULUB station.

($V_P = 6.3\,\mathrm{Km/s}$ $h = 35.5 \pm 4.2$ $V_P / V_S = 1.82 \pm 0.11$ $corr = -97.7\%$)

4.2.11. North – South profile: ISPARTA (ISP) station

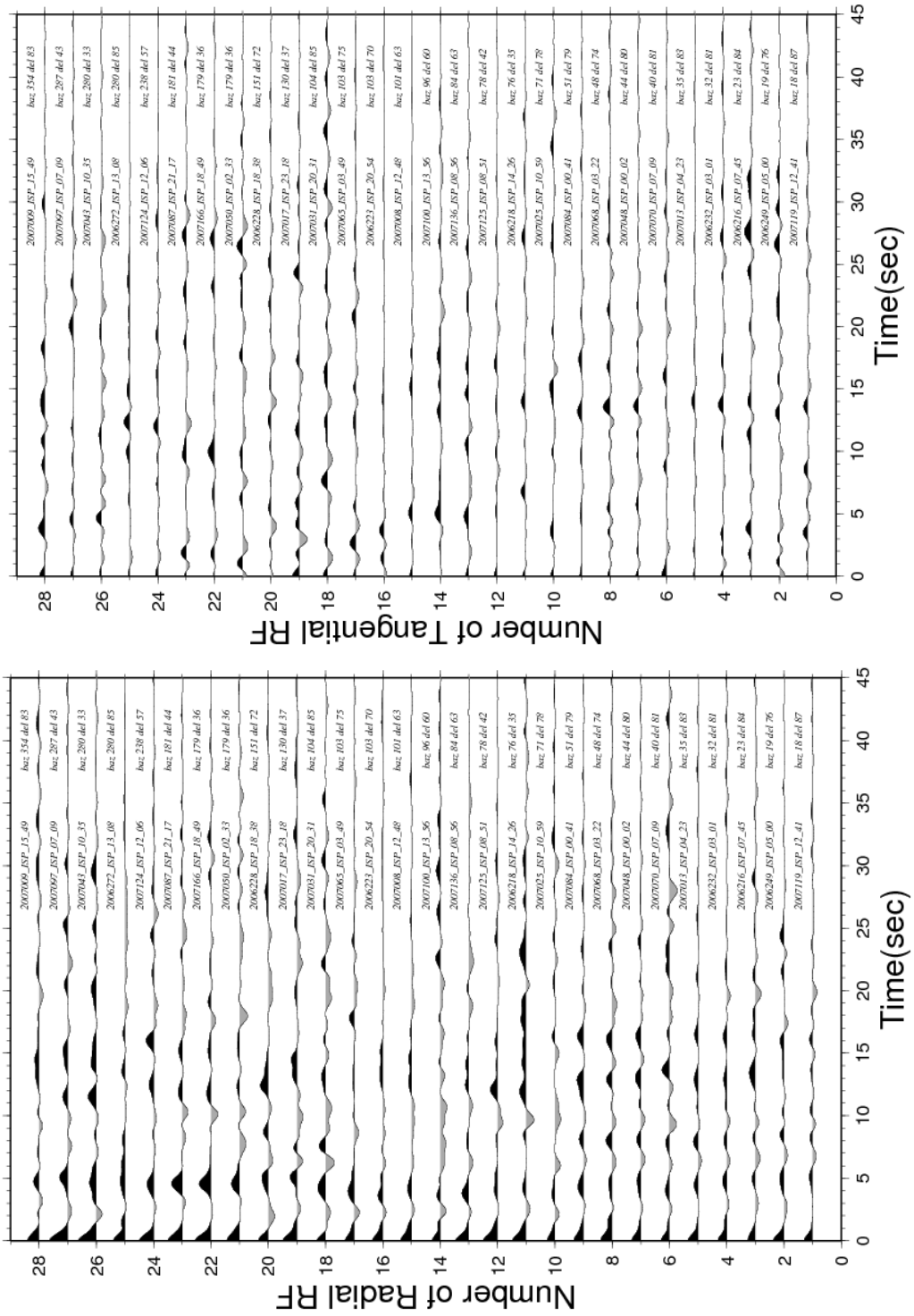

Figure 4.40. The radial and tangential RFs for ISP station.

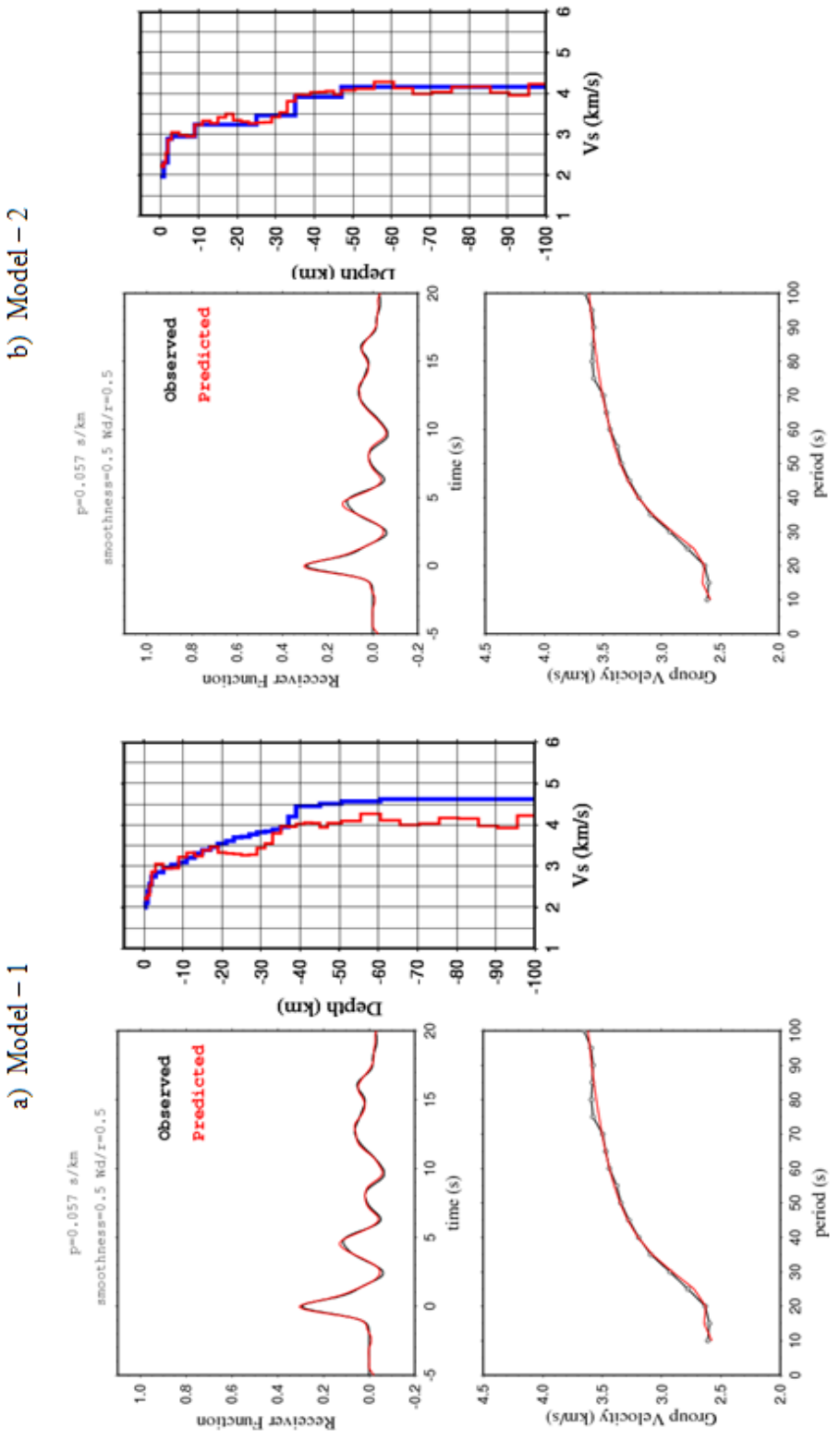

Figure 4.41. Joint inversion of RFs and surface waves with two different initial models beneath the ISP station.

Table 4.13. Velocity structure beneath the ISP station.

a) The average velocity results using Model – 1.

Layers	Thickness (km)	Vp (km/s)	Vs (km/s)	ρ (g/cm^3)
1	2,00	4,05	2,31	2,07
2	13,00	5,40	3,08	2,50
3	14,00	5,83	3,33	2,64
4	8,00	6,44	3,68	2,83
5	6,00	7,00	4,00	3,01
6	57,50	7,14	4,07	3,05

b) The average velocity results using Model – 2.

Layers	Thickness (km)	Vp (km/s)	Vs (km/s)	ρ (g/cm^3)
1	2,00	4,03	2,32	2,06
2	13,00	5,36	3,09	2,49
3	14,00	5,79	3,34	2,62
4	8,00	6,39	3,69	2,82
5	6,00	6,95	4,01	3,00
6	57,50	7,09	4,09	3,04

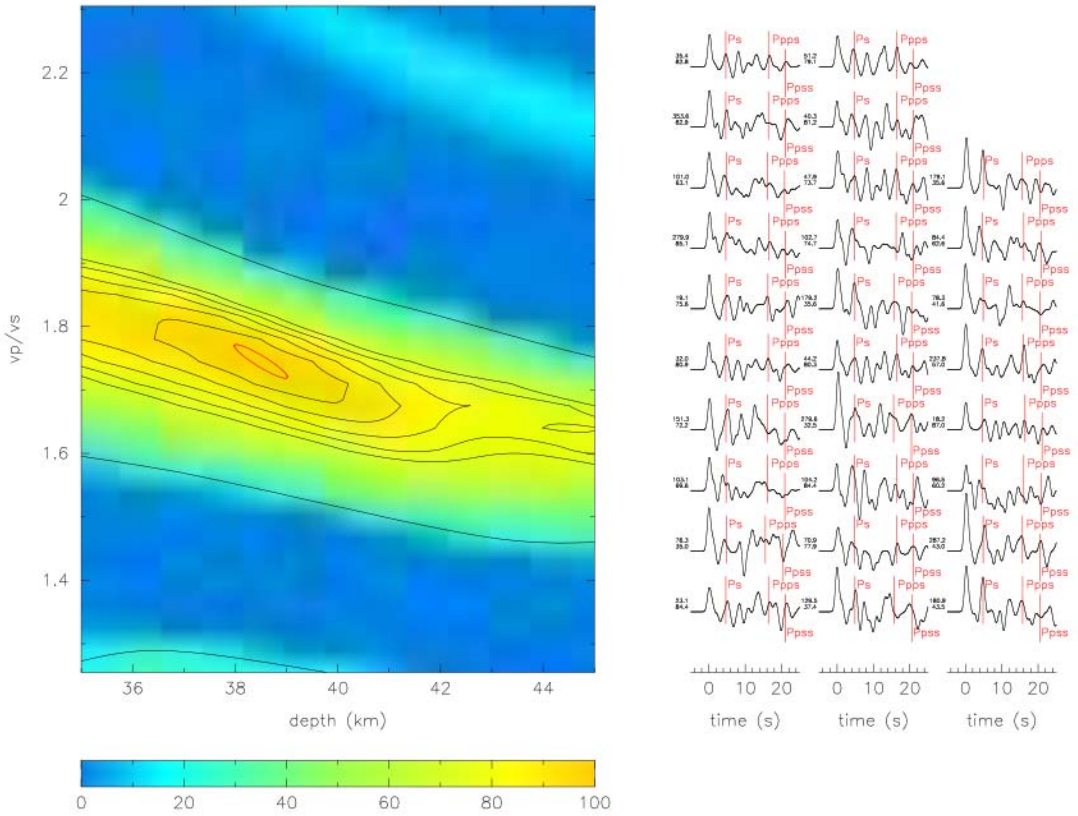

Figure 4.42. The $H-\kappa$ stacking result for ISP station.

($V_P = 6.3$ Km/s $h = 35.8 \pm 1.0$ $V_P / V_S = 1.75 \pm 0.05$ $corr = -92.3\%$)

4.2.12. North – South profile: KIZILKAYA (KZLK) station

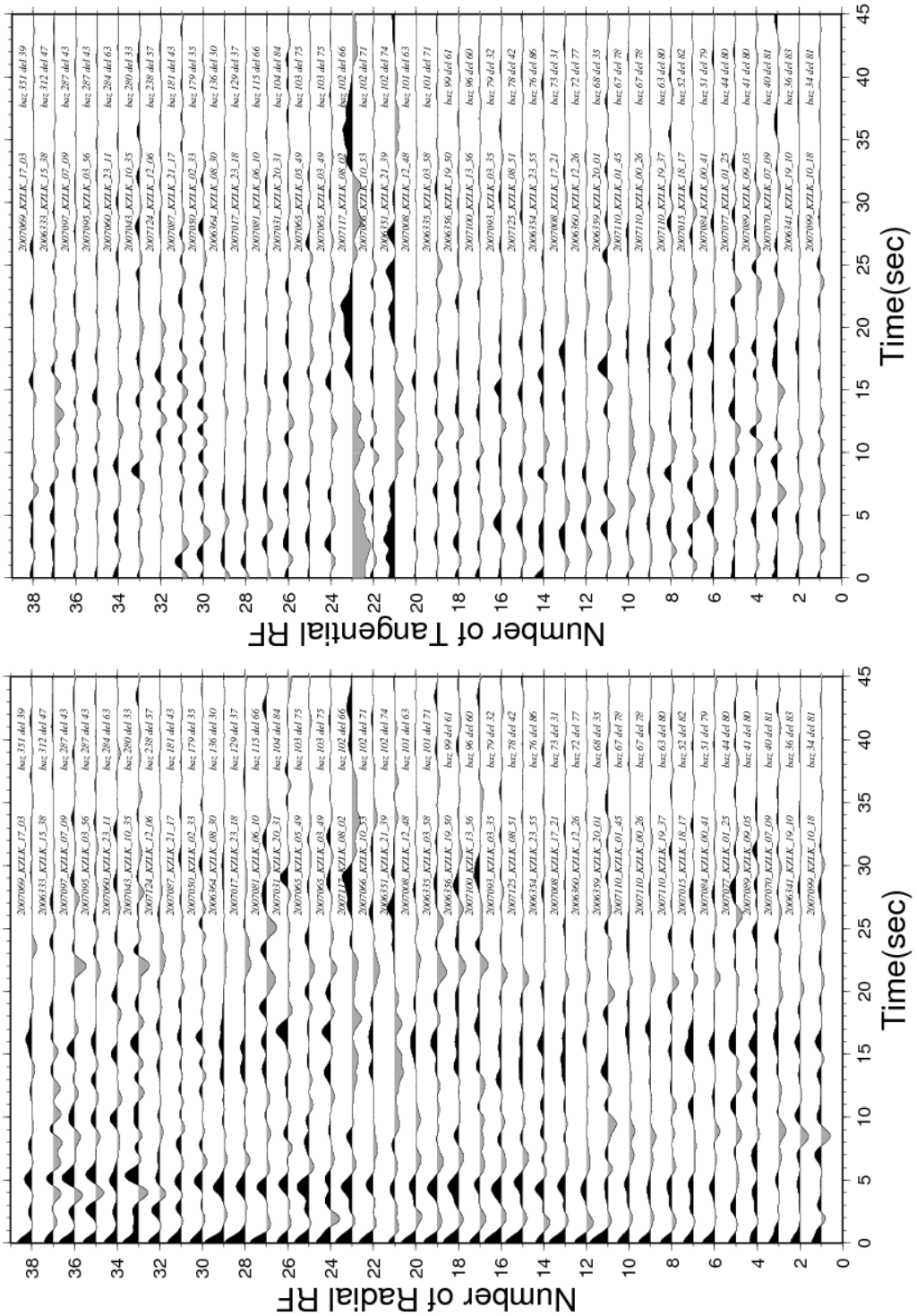

Figure 4.43. The radial and tangential RFs for KZLK station.

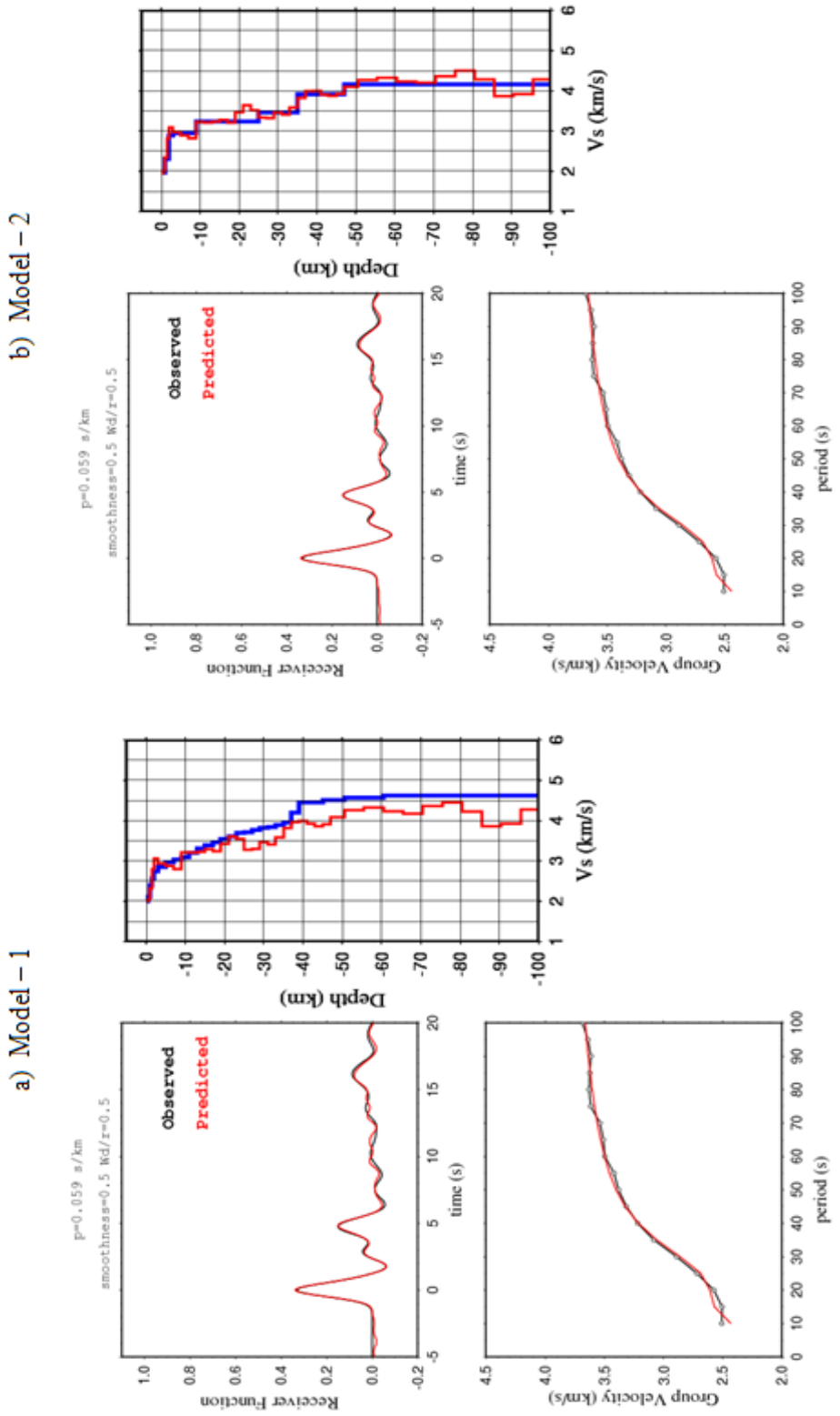

Figure 4.44. Joint inversion of RFs and surface waves with two different initial models beneath the KZLK station.

Table 4.14. Velocity structure beneath the KZLK station.

a) The average velocity results using Model – 1.

Layers	Thickness (km)	Vp (km/s)	Vs (km/s)	ρ (g/cm^3)
1	2,00	4,00	2,28	2,05
2	13,00	5,33	3,04	2,47
3	14,00	5,92	3,38	2,66
4	8,00	6,24	3,57	2,77
5	6,00	6,93	3,96	2,99
6	57,50	7,27	4,15	3,10

b) The average velocity results using Model – 2.

Layers	Thickness (km)	Vp (km/s)	Vs (km/s)	ρ (g/cm^3)
1	2,00	3,94	2,27	2,03
2	13,00	5,31	3,06	2,47
3	14,00	5,89	3,39	2,65
4	8,00	6,19	3,57	2,75
5	6,00	6,88	3,97	2,97
6	57,50	7,22	4,16	3,08

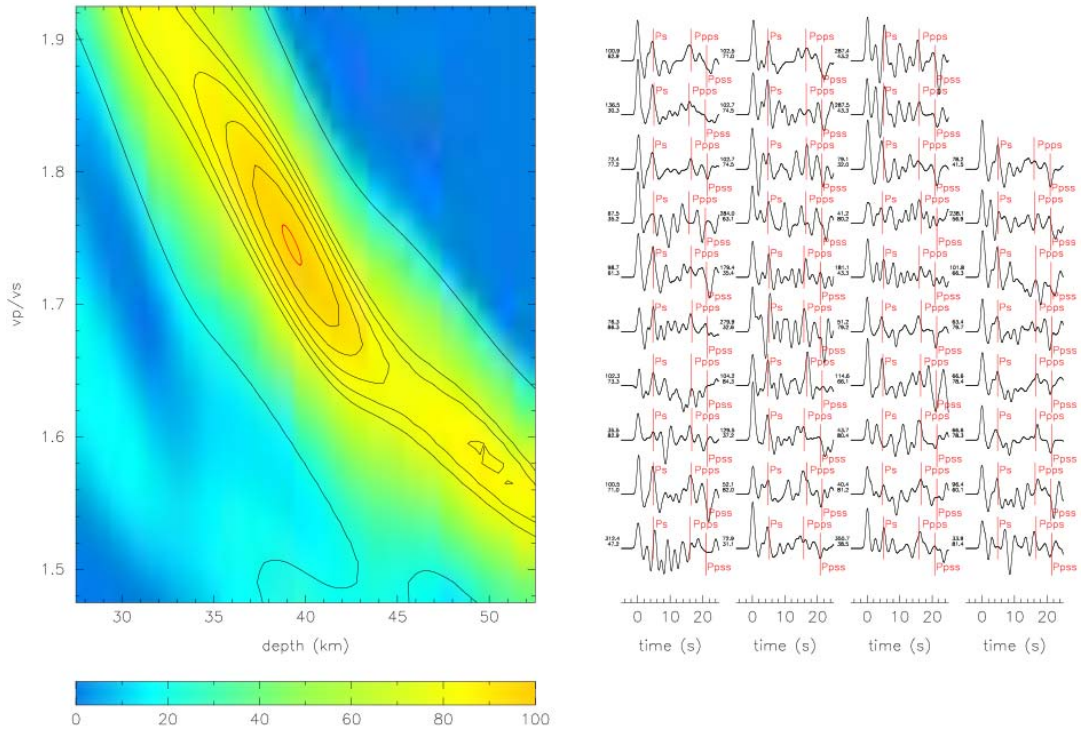

Figure 4.45. The $H-\kappa$ stacking result for KZLK station.

($V_P = 6.3$ Km/s $h = 39.2 \pm 1.1$ $V_P / V_S = 1.75 \pm 0.05$ $corr = -85.9\%$)

4.2.13. North – South profile: DÖŞEMEALTI (DSMA) station

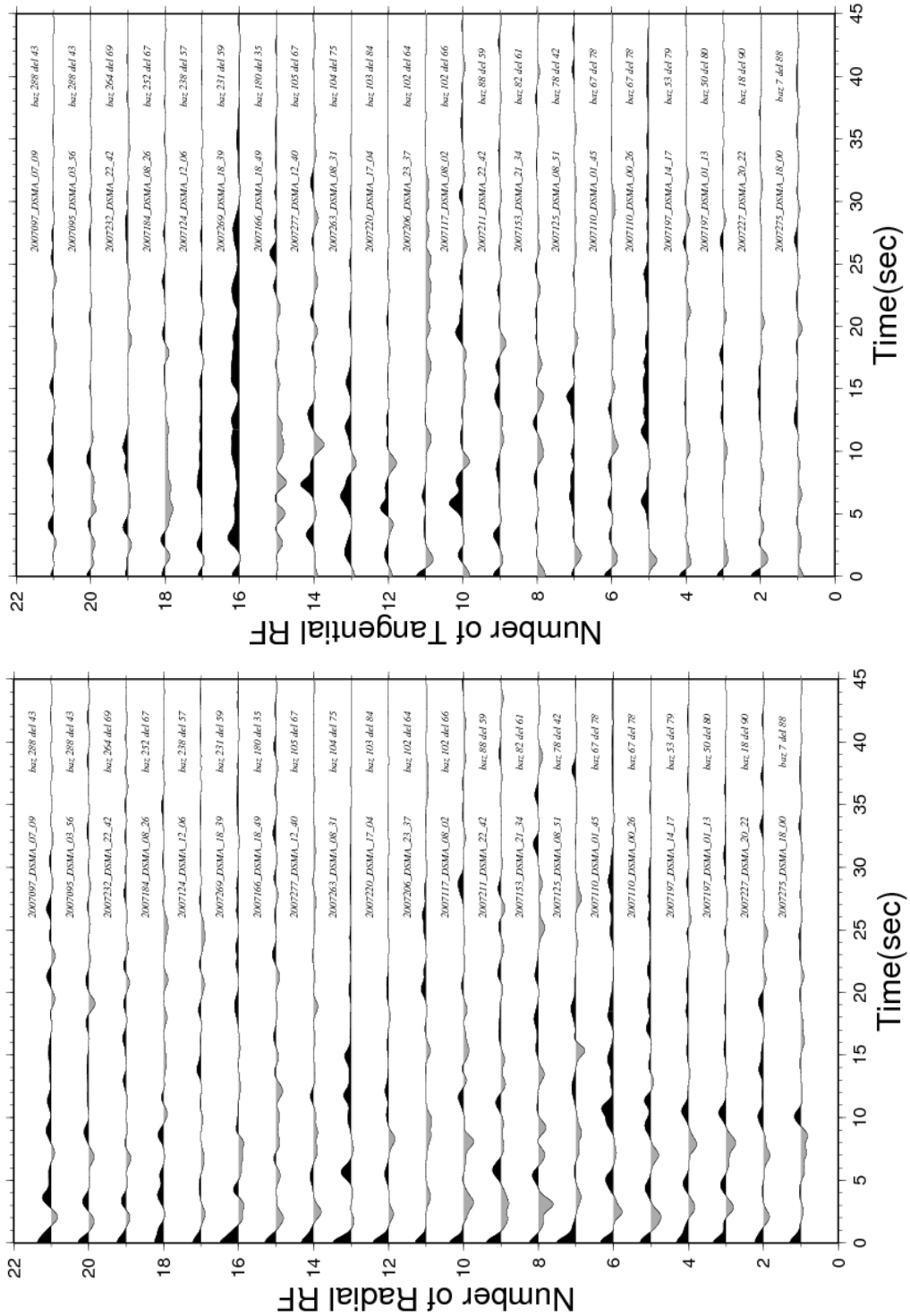

Figure 4.46. The radial and tangential RFs for DSMA station.

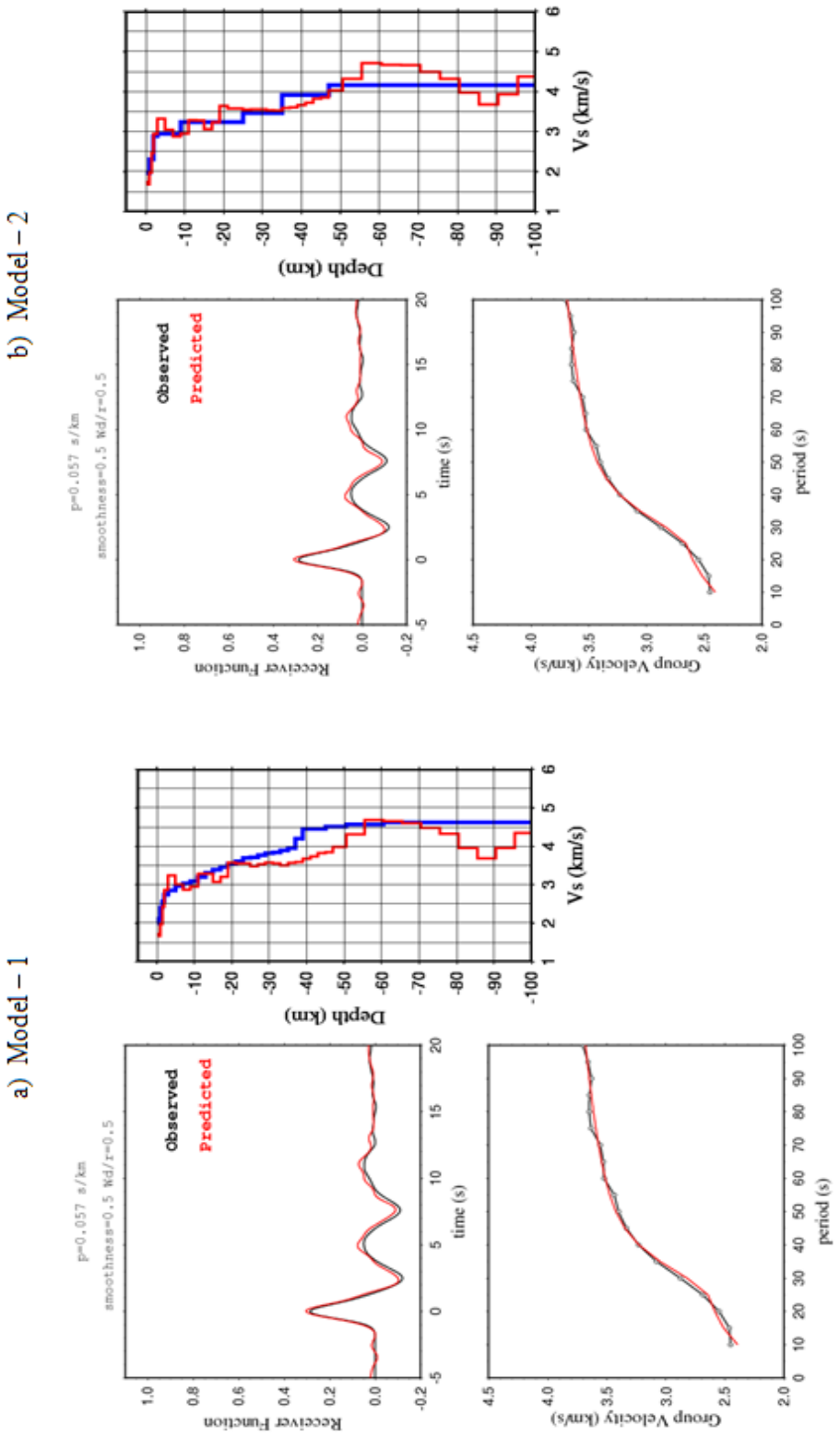

Figure 4.47. Joint inversion of RFs and surface waves with two different initial models beneath the DSMA station.

Table 4.15. Velocity structure beneath the DSMA station.

a) The average velocity results using Model – 1.

Layers	Thickness (km)	Vp (km/s)	Vs (km/s)	ρ (g/cm^3)
1	2,00	3,40	1,94	1,86
2	13,00	5,37	3,07	2,49
3	14,00	5,99	3,42	2,69
4	8,00	6,20	3,55	2,76
5	6,00	6,41	3,67	2,82
6	57,50	7,36	4,20	3,13

b) The average velocity results using Model – 2.

Layers	Thickness (km)	Vp (km/s)	Vs (km/s)	ρ (g/cm^3)
1	2,00	3,41	1,96	1,86
2	13,00	5,37	3,10	2,49
3	14,00	5,99	3,45	2,69
4	8,00	6,16	3,55	2,74
5	6,00	6,35	3,66	2,80
6	57,50	7,31	4,22	3,11

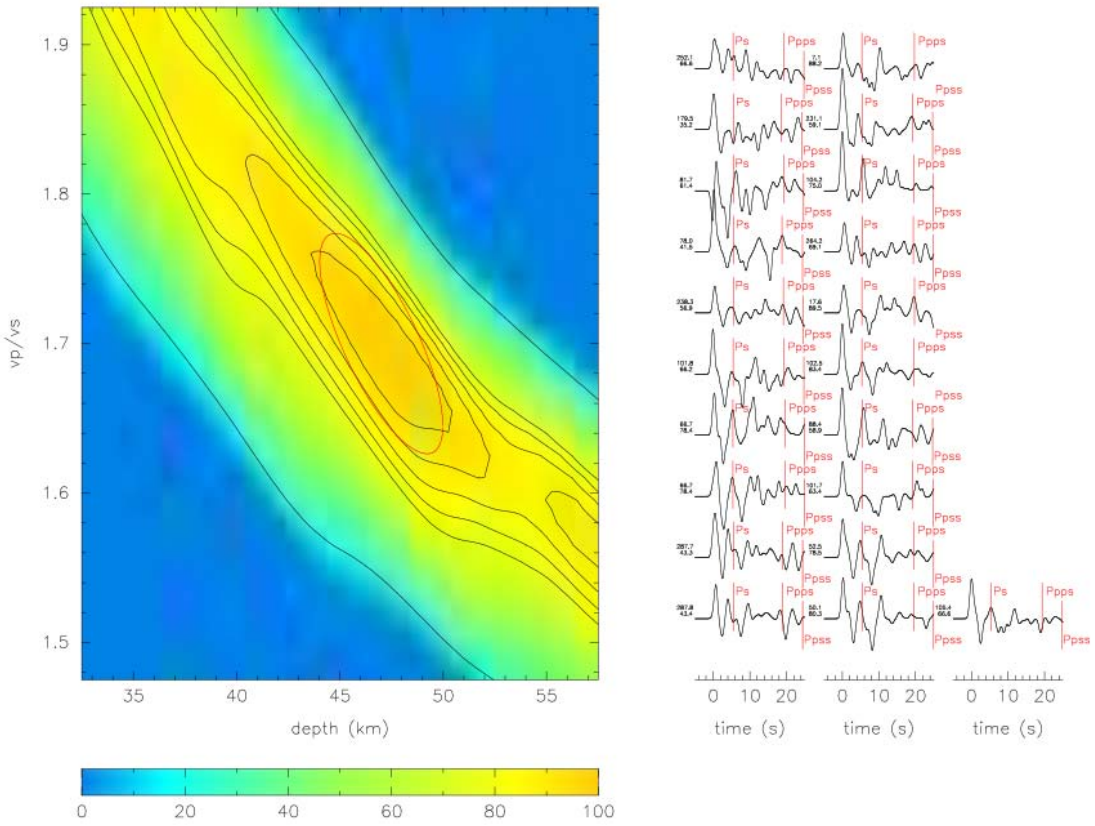

Figure 4.48. The $H-\kappa$ stacking result for DSMA station.

($V_P = 6.3\,\mathrm{Km/s}$ $h = 47.0 \pm 6.0$ $V_P / V_S = 1.70 \pm 0.15$ $corr = -74.5\%$)

4.2.14. North – South profile: ANTALYA (ANTB) station

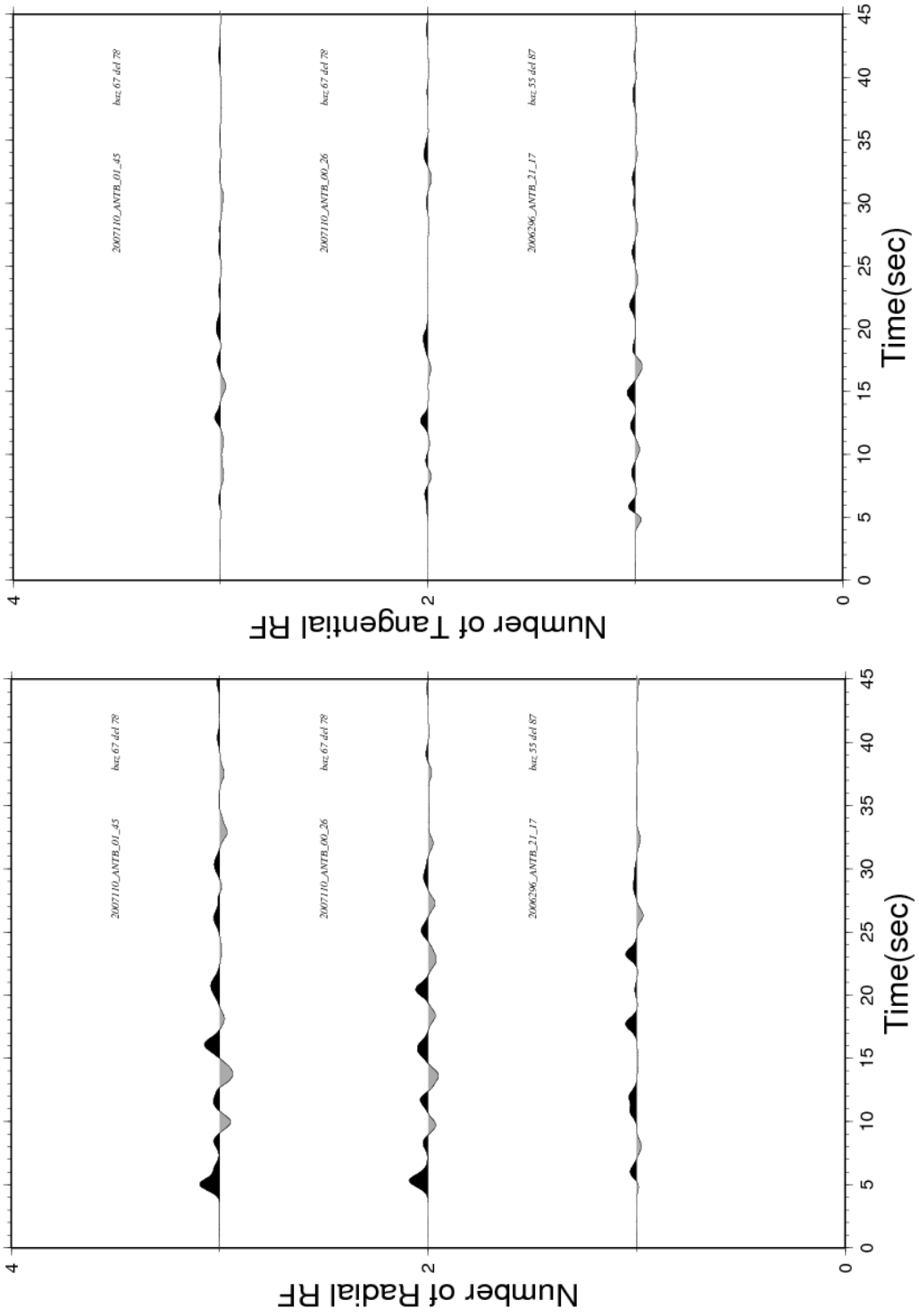

Figure 4.49. The radial and tangential RFs for ANTB station.

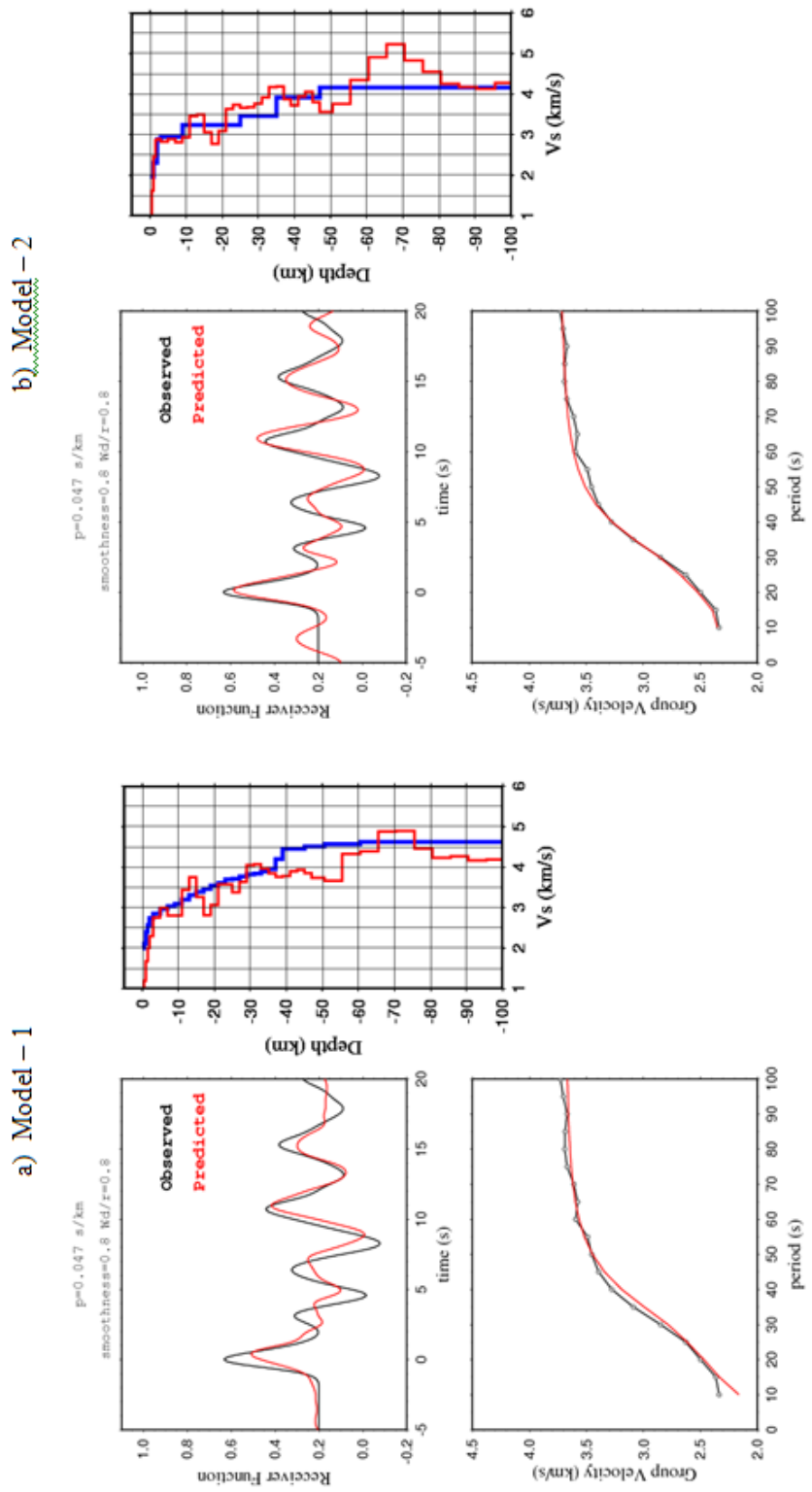

Figure 4.50. Joint inversion of RFs and surface waves with two different initial models beneath the ANTB station.

Table 4.16. Velocity structure beneath the ANTB station.

a) The average velocity results using Model – 1.

Layers	Thickness (km)	Vp (km/s)	Vs (km/s)	ρ (g/cm^3)
1	2,00	2,47	1,41	1,56
2	13,00	5,21	2,97	2,44
3	14,00	5,82	3,33	2,63
4	8,00	6,96	3,98	3,00
5	6,00	6,66	3,81	2,90
6	57,50	7,41	4,23	3,14

b) The average velocity results using Model – 2.

Layers	Thickness (km)	Vp (km/s)	Vs (km/s)	ρ (g/cm^3)
1	2,00	3,37	1,94	1,85
2	13,00	5,28	3,04	2,46
3	14,00	5,85	3,37	2,64
4	8,00	6,96	4,01	3,00
5	6,00	6,67	3,85	2,91
6	57,50	7,45	4,30	3,15

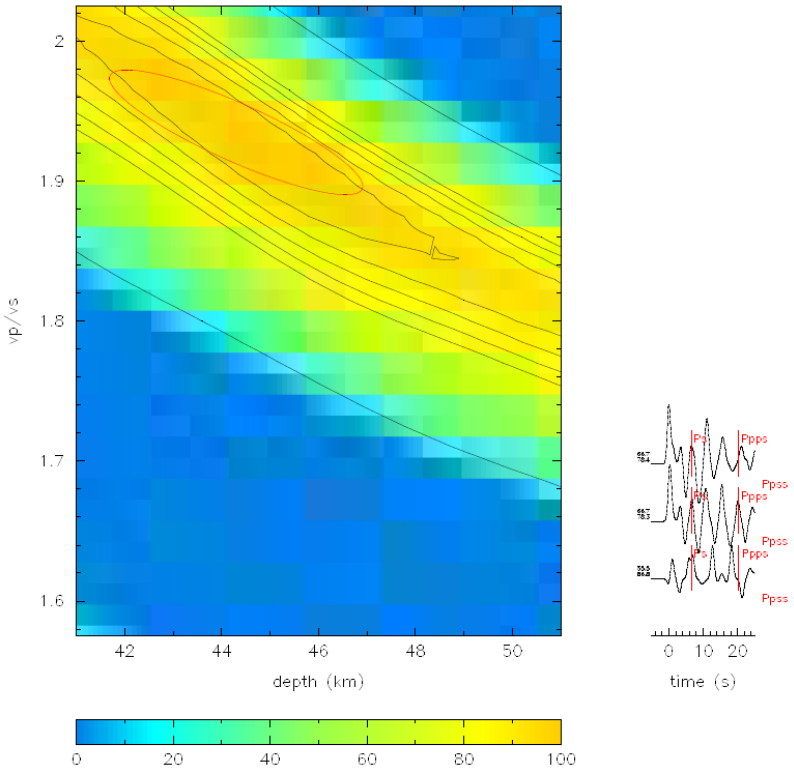

Figure 4.51. The $H-\kappa$ stacking result for ANTB station.

($V_P = 6.3\,\mathrm{Km/s}$ $h = 44.3 \pm 5.2$ $V_P / V_S = 1.93 \pm 0.09$ $corr = -86.4\%$)

4.3. The Results of Data Analysis

We applied the joint inversion technique and H-K stacking technique to fourteen stations in the region. Basically we used two different initial model during the inversion. The initial models consist of layer thickness ranging from 2 to 5 km down to 100.5 km. The thinner layers were chosen for the upper crust and increased down to thicker layer at the deepest parts of the model as the study of Gök *et al.,* (2007). We used two different references while creating the initial models as explained in section 4.1. H-K stacking technique applied as a secondary method.

According to result of joint inversion, the shear velocities are slower depth to the 0 – 2 km beneath eastern stations (SUTC, HULU and AKRN) compared to western stations (ACPY, SALD and CLTK) as shown in Table 4.17. Mid crustal velocities are compatible with all stations in the east – west profile for both initial models. The upper mantle velocities are very low on this profile.

Table 4.17. The average velocities in the east – west profile.

Model – 1

		Western Stations		Eastern Stations	
Layers	Thickness (km)	Vp (km/s)	Vs (km/s)	Vp (km/s)	Vs (km/s)
1	2,00	4,26	2,43	3,69	2,11
2	13,00	5,33	3,04	5,32	3,04
3	14,00	5,88	3,36	5,98	3,41
4	8,00	6,39	3,65	6,31	3,61
5	6,00	6,82	3,90	6,80	3,89
6	57,50	7,19	4,10	7,22	4,12

Model – 2

		Western Stations		Eastern Stations	
Layers	Thickness (km)	Vp (km/s)	Vs (km/s)	Vp (km/s)	Vs (km/s)
1	2,00	4,17	2,40	3,70	2,13
2	13,00	5,30	3,06	5,32	3,07
3	14,00	5,86	3,38	5,94	3,42
4	8,00	6,33	3,65	6,27	3,61
5	6,00	6,76	3,90	6,73	3,88
6	57,50	7,14	4,12	7,16	4,13

The average velocities in the north – south profile indicate that the shear velocities are slower in southern stations (CLTK, KZLK, DSMA and ANTB) with respect to northern stations (AFYN, SHUT, HYDR, ULUB and ISP) for shallow depth range (0 – 2 km). The shear wave variation is very small for mid crustal dept range (2 – 37 km) as shown in Table 4.18. However, there is a clear velocity decreasing dept range of 37 – 43 km from north to south. After 43 km, seismic velocities start to increase depth to 100.5 km from north to south.

Table 4.18. The average velocities in the north – south profile.

Model – 1

Layers	Thickness (km)	Northern Stations Vp (km/s)	Northern Stations Vs (km/s)	Southern Stations Vp (km/s)	Southern Stations Vs (km/s)
1	2,00	3,80	2,17	3,54	2,02
2	13,00	5,50	3,14	5,33	3,04
3	14,00	5,88	3,36	5,91	3,38
4	8,00	6,43	3,68	6,44	3,68
5	6,00	6,93	3,96	6,66	3,81
6	57,50	7,08	4,04	7,30	4,17

Model – 2

Layers	Thickness (km)	Northern Stations Vp (km/s)	Northern Stations Vs (km/s)	Southern Stations Vp (km/s)	Southern Stations Vs (km/s)
1	2,00	3,77	2,17	3,71	2,13
2	13,00	5,47	3,15	5,40	3,11
3	14,00	5,85	3,37	5,92	3,41
4	8,00	6,38	3,68	6,36	3,66
5	6,00	6,88	3,97	6,63	3,81
6	57,50	7,02	4,05	7,26	4,18

On the other hand, Moho depth was figured out by applying H-K stacking technique as shown in Table 4.19.

Table 4.19. Shows the details that belogs to H-K stacking method.
W1, W2 and W3 are the coefficients of H-K stagking method.

Station name	Initial Vp (km/s)	H (depth) km	Vp/Vs	Correlation (%)	W1	W2	W3	Number of RFs	
ACPY	6.3	35.2 +/-3.5	1.70 +/-0.17	-97.7	0.7	0.1	0.1	21	East-West Profile
SALD	6.3	40.7 +/-0.9	1.74 +/-0.02	-89.0	0.7	0.2	0.1	28	
CLTK	6.3	40.7 +/-1.7	1.54 +/-0.10	-80.0	0.7	0.2	0.0	20	
SUTC	6.3	33.5 +/-2.7	1.66 +/-0.28	72.2	0.7	0.2	0.1	22	
HULU	6.3	32.4 +/-4.7	1.86 +/-0.13	-91.4	0.8	0.1	0.1	41	
AKRN	6.3	30.5 +/-0.4	1.94 +/-0.03	-92.0	0.7	0.2	0.0	96	
AFYN	6.3	36.2 +/-0.5	1.77 +/-0.02	-87.9	0.7	0.2	0.0	25	North-South Profile
SHUT	6.3	37.5 +/-0.9	1.72 +/-0.02	-87.9	0.7	0.2	0.1	44	
HYDR	6.3	36.0 +/-3.1	1.83 +/-0.08	-97.6	0.7	0.2	0.0	18	
ULUB	6.3	35.5 +/-4.2	1.82 +/-0.11	-97.7	0.7	0.2	0.1	17	
ISP	6.3	35.8 +/-1.0	1.75 +/-0.05	-93.2	0.8	0.2	0.0	28	
CLTK	6.3	40.7 +/-1.7	1.54 +/-0.10	-80.0	0.7	0.2	0.0	20	
KZLK	6.3	39.2 +/-1.1	1.75 +/-0.05	-85.9	0.7	0.2	0.1	38	
DSMA	6.3	47.0 +/-6.0	1.70 +/-0.15	-74.5	0.7	0.1	0.1	21	
ANTB	6.3	44.3 +/-5.2	1.93 +/-0.09	-86.4	0.9	0.1	0.0	3	

Figure 4.52 shows the contour map using the result of H-K stacking method to illustrate the variation of the Moho topography across the study area. The Moho depths were fitted by adjustable tension continuous curvature surface gridding algorithm in GMT package (Wessel and Smith, 1998).

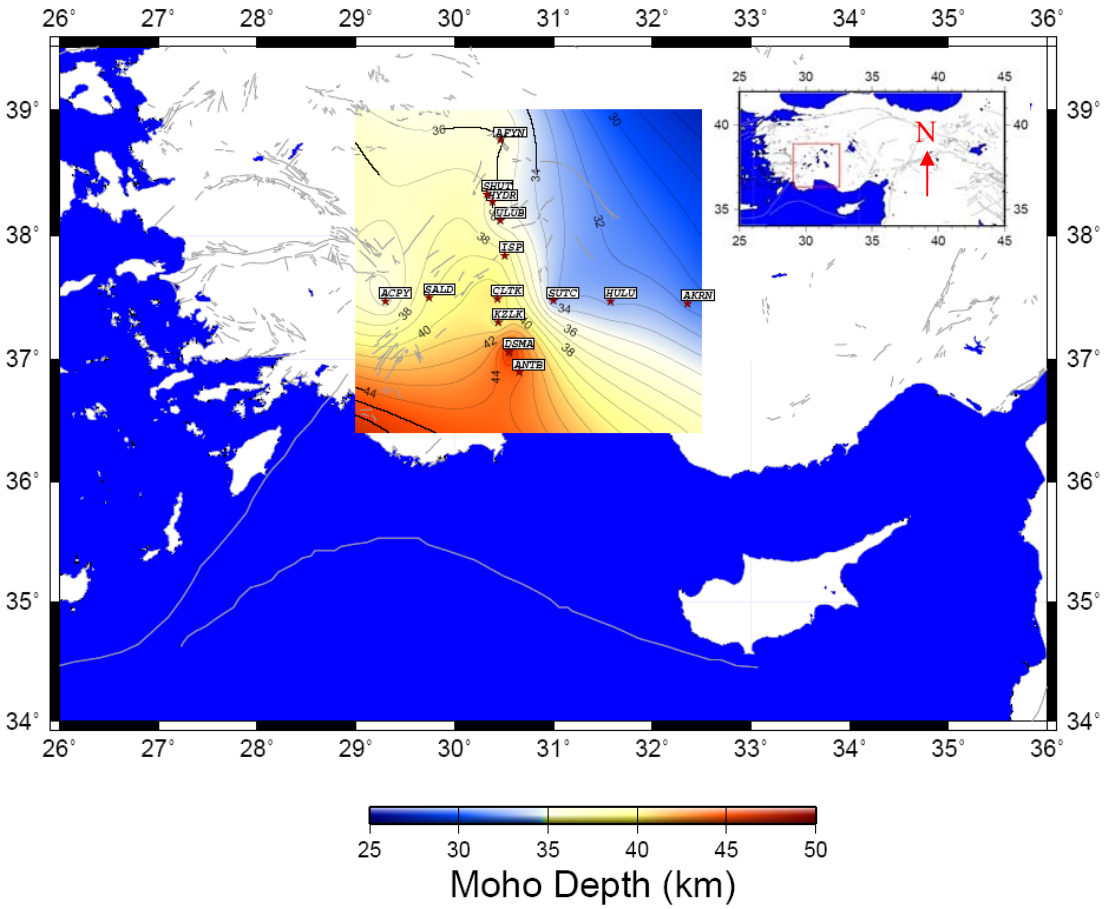

Figure 4.52. Shows the depth map of Moho

Moho depth is thicker beneath western and southern stations with respect to eastern and northern stations.

5. DISCUSSION AND CONCLUSION

We have obtained the shear wave velocity model for the Isparta Angle down to about 100.5 km by joint inversion of stacked receiver functions and surface wave group velocities as well as, Moho depth was calculated using the same receiver functions by applying H-K stacking technique beneath each station on east – west and north – south profiles.

We found that upper and mid crustal shear velocities are higher beneath ACPY, SALD and CLTK stations in the west compared to SUTC, HULU and AKRN stations in the east for two different initial models. The average shear velocities for both initial model are close to each other which are between 3.17 – 3.33 km/s and 3.20 - 3.33 km/s for model – 1 and model – 2, respectively. These upper and mid crustal velocities are relatively slower than the other geophysical studies that were done by Karagianni *et al.,* (2005) who found 3.50 km/s and Erduran *et al.,* (2007) who found 3.55 km/s shear wave velocity. On the other hand, we have estimated very low seismic velocities upper mantle depths which are varying 7.16 – 7.25 km/s P velocity for model – 1 and 7.12 – 7.18 km/s P velocity for model – 2. Pn tomographic imaging study of Al-Lazki, (2004), also, indicates that Pn velocities are slower than 7.8 km/s for the Isparta Angle. The very low Pn velocity could be related to a very thin to absent mantle lid, where Pn propation is actually sampling asthenospheric rather than lithospheric mantle (Al-Lazki, 2004).

We have observed that Moho depth is thicker beneath again ACPY, SALD and CLTK stations with respect to SUTC, HULU and AKRN stations. The average Moho depth is 38.8 km in the west whereas 32.1 km in the east. Moho depth variation may be explained by the dip angle of subducting slab along the Cyprus arc is relatively lower than the slab being subducted along the Hellenic arc (Kempler and Ben-Avram, 1987; Wortel and Spakman, 1992) which may lead shallow Moho depth structure in the east conversely the high dip angle of slab in the west may be the reason of thicker crust.

We have estimated the upper crustal and mid crustal velocities for two initial models along north – south profiles which indicated there is no clear shear velocity change

between stations. The average shear velocity is varying 3.10 – 3.29 km/s and 3.14 – 3.30 km/s for model -1 and model – 2, respectively. The difference was observed for upper mantle velocities which increase from north to south. The upper mantle P velocity beneath AFYN station, the northern most station, is 6.95 km/s for model – 1 and 6.90 km/s for model – 2, it is increases to 7.12 – 7.16 km/s until CLTK station. After this station, the upper mantle P velocities for southern stations are relatively higher than northern stations which are 7.22 – 7.27 km/s for KZLK, 7.31 – 7.36 km/s for DSMA and lastly 7.41 – 7.45 km/s for ANTB station. The upper mantle P velocities are very slower as in the east – west profile except southern increasing. The reason of these low P velocities could be related to the presence of partial melt which lowers normal lithospheric mantle velocities by at least 5-6 percent (Sato *et al.,* 1989). In addition to this, Horasan *et al.,* (2002) support this idea that Pn velocity variation is interpreted as due to the thinning of the lithosphere toward the active Aegean arc in the south, where a volatile fluxed, partially melted upper-mantle zone exist just above the northward dipping subduction slab. Also, regional wave propagation study of Gök, (2000) imply that throughout central Anatolia, Lg is partially attenuated indicating the presence of either strong scattering or crustal incrisic attenuation, in south western Turkey, Lg is weak or blocked along the Taurus mountains. These studies support the very low seismic velocities in the region.

There is small Moho depth variation beneath northern stations (AFYN, SHUT, HYDR, ULUB and ISP) which is between 35.5 – 37.5 km. The other receiver function studies using ISP station show similar Moho depth which Kalyoncuoglu *et al.,* (2003) found 31 km, Yelkenci, (2006) calculated 39.1 km, Horasan *et al.,* (2002) estimated 33 km average crustal thickness for Aegean region. The southern stations (CLTK, KZLK, DSMA and ANTB) have thicker Moho depth according to northern stations which is 40.7 km for CLTK, 39.2 km KZLK, 47.0 km DSMA and lastly 44.3 km ANTB station. Moho depth is getting thicker from north to south.

In conclusion, mid crustal velocities is in agreement with other geophysical studies however upper mantle velocities are found very low with respect to studies that were done in the same region. Moho depth is varying from west to east and north to south. The difference of this study from the other ones is that this is the first study to examine extraordinary settings of Isparta Angle using fourteen broad-band sensors compared to

studies that were done in the same region. The results reflect the unusual properties of Isparta Angle. The result of the other studies obtained by one station or limited number of station in the region for now on. In addition to this, regional studies were done for western Turkey but not specifically Isparta Angle. This is obviously separate this study from the others.

Although we figure out the crustal velocities and crustal thickness in the region, this study can be extended with including the other stations in the region. By applying earthquake location studies, local and regional tomography, wave propagation studies and S-receiver function, we will have a clear picture of subducting slab geometry, idea of slab-tearing, location of slab-tearing and source of low upper mantle seismic velocities in the region.

APPENDIX A: LIST OF EVENTS USED IN THE ANALYSIS

Event number	Event name	Latitute	Longitute	Depth (km)	Magnitude (Mb)
1	2006216074547.7	52.120	171.040	10	5.5
2	2006218142619.3	37.370	74.730	11	5.6
3	2006223205414.4	2.400	96.350	22	6.2
4	2006224183917.2	28.790	130.020	22	5.6
5	2006226001309.3	19.020	-64.640	21	5.5
6	2006227122617.4	51.090	179.260	19	5.7
7	2006228183859.3	-28.820	61.740	7	5.9
8	2006229111135.5	55.620	161.690	55	6.1
9	2006229152035.0	46.540	141.910	14	6.0
10	2006232030102.4	49.820	156.410	26	6.0
11	2006233222049.5	33.630	135.820	411	5.5
12	2006236215036.7	51.150	157.520	43	6.5
13	2006238234039.5	51.330	-179.570	35	5.8
14	2006238234618.5	51.380	-179.540	35	5.7
15	2006239171117.5	24.950	122.940	146	5.5
16	2006242161339.7	-17.650	65.940	10	5.7
17	2006243225825.8	28.800	130.030	33	5.6
18	2006244102517.1	53.260	159.700	51	5.7
19	2006244120422.2	53.970	-166.390	75	5.9
20	2006249050028.0	61.630	168.640	7	5.5
21	2006254181222.3	35.470	78.220	14	5.5
22	2006255155630.8	8.280	126.490	36	5.5
23	2006259022250.6	41.360	135.700	367	5.9
24	2006259061746.9	5.120	94.780	49	5.6
25	2006260073011.1	-17.690	41.830	10	5.5
26	2006261034556.9	51.600	-173.960	18	5.8
27	2006262135856.9	-9.900	107.350	12	5.9
28	2006264185450.0	-9.050	110.360	25	6.0
29	2006267225621.1	-17.740	41.810	6	5.7
30	2006271013648.3	46.460	153.360	11	5.9
31	2006272130826.2	10.880	-61.760	53	6.1
32	2006272182305.9	10.810	-61.760	52	5.5
33	2006273124722.9	7.280	-34.660	10	5.6
34	2006273175023.0	46.350	153.170	11	6.6
35	2006273175616.1	46.190	153.170	10	6.0
36	2006273183338.0	46.330	153.260	10	5.5
37	2006274090602.3	46.470	153.240	19	6.5
38	2006282100147.4	20.650	120.020	14	6.3
39	2006282110828.1	20.710	119.980	10	5.9
40	2006282181933.7	-51.030	29.020	10	5.7
41	2006283002358.0	37.200	142.660	9	6.0
42	2006284064353.8	20.710	120.080	10	5.7

Event number	Event name	Latitute	Longitute	Depth (km)	Magnitude (Mb)
43	2006285053035.4	4.940	95.010	30	5.5
44	2006285144629.9	24.150	122.630	35	5.7
45	2006286134739.2	46.240	153.280	4	5.9
46	2006293143100.2	13.430	121.470	22	5.8
47	2006293172703.2	13.490	121.530	25	5.8
48	2006293220927.3	13.420	121.550	10	5.6
49	2006294182321.0	13.370	121.380	18	5.9
50	2006296211720.0	29.350	140.270	11	6.4
51	2006302083144.6	29.370	140.200	10	5.6
52	2006312145652.2	47.170	153.960	10	5.6
53	2006316212742.4	48.280	154.250	36	6.1
54	2006319111413.6	46.590	153.270	10	8.3
55	2006319112306.9	46.300	154.610	10	5.6
56	2006319112429.9	46.270	154.520	10	5.6
57	2006319112457.5	47.770	153.180	10	5.5
58	2006319001125.1	47.520	152.650	10	6.0
59	2006319112838.5	46.090	154.100	10	6.0
60	2006319112922.8	46.370	154.480	10	6.2
61	2006319113323.8	46.860	153.730	10	5.5
62	2006319113458.1	46.650	155.300	10	6.4
63	2006319114055.0	46.480	154.730	10	6.7
64	2006319114804.2	44.100	154.700	10	5.5
65	2006319121605.5	47.110	154.420	10	5.7
66	2006319121644.1	46.190	154.670	10	5.9
67	2006319122615.8	47.420	153.860	10	5.7
68	2006319122821.3	47.060	155.530	10	5.5
69	2006319192526.0	47.010	154.980	10	6.0
70	2006319192806.4	47.080	155.170	10	5.5
71	2006319211708.2	46.870	155.000	10	5.5
72	2006319212221.5	47.280	154.150	12	6.0
73	2006319212522.5	47.140	153.510	10	5.7
74	2006319213124.3	47.380	154.160	13	5.5
75	2006319213509.6	47.670	154.550	10	5.6
76	2006319214008.5	46.720	153.300	10	5.5
77	2006320062020.8	46.360	154.470	9	6.0
78	2006321063349.4	47.020	155.530	10	5.6
79	2006321180312.3	28.590	129.900	22	6.2
80	2006322135521.2	4.750	94.780	32	5.9
81	2006322135753.8	4.740	94.770	29	5.9
82	2006323151652.2	46.900	154.890	10	5.6
83	2006326111509.6	44.150	146.780	79	5.6
84	2006327200446.6	47.540	154.200	10	5.7
85	2006328153410.2	46.760	153.770	11	5.7
86	2006329121022.0	53.590	-163.750	13	5.5
87	2006332080151.8	46.690	155.530	10	5.6

Event number	Event name	Latitute	Longitute	Depth (km)	Magnitude (Mb)
88	2006333153844.5	53.740	-35.440	10	5.6
89	2006335035821.6	3.390	99.080	204	6.3
90	2006337081951.3	-0.540	-19.740	10	5.6
91	2006341191021.8	46.150	154.390	16	6.4
92	2006343092446.8	5.080	94.750	30	5.5
93	2006343144854.2	47.440	147.050	396	5.8
94	2006344152809.3	29.760	130.520	35	5.7
95	2006349165902.4	46.410	153.040	10	5.7
96	2006349170109.6	46.390	153.060	10	5.5
97	2006351211021.9	4.820	95.020	36	5.8
98	2006351213917.5	0.630	99.860	30	5.8
99	2006354235555.9	13.270	125.810	24	5.6
100	2006356195044.6	10.650	92.360	24	6.2
101	2006357225940.5	-6.780	105.640	30	5.5
102	2006359200100.5	42.160	76.160	11	5.8
103	2006360122621.1	21.800	120.550	10	7.3
104	2006360123413.8	21.970	120.490	10	7.1
105	2006360124021.7	21.640	120.850	10	5.5
106	2006360151945.2	48.320	154.840	10	6.0
107	2006360154144.8	22.070	120.410	22	5.5
108	2006361023036.5	22.000	120.480	10	5.6
109	2006364083049.8	13.310	51.370	15	6.6
110	2007005165222.4	55.760	-156.060	18	5.8
111	2007008124840.5	8.080	92.440	11	6.2
112	2007008172149.9	39.800	70.310	16	6.1
113	2007009154933.5	59.420	-137.120	10	5.8
114	2007011203447.3	43.470	147.080	10	5.5
115	2007013042321.2	46.240	154.520	10	8.2
116	2007013043707.7	46.330	155.170	10	5.5
117	2007013091831.7	45.570	153.760	10	5.8
118	2007013173706.3	46.910	156.280	10	6.0
119	2007013193732.7	47.050	155.530	10	5.6
120	2007015181759.2	34.890	138.640	170	5.9
121	2007017231849.8	10.120	58.710	8	6.2
122	2007018152718.3	-5.490	101.450	17	5.9
123	2007019024423.4	-9.990	109.670	25	5.9
124	2007023041607.4	-43.140	41.650	10	5.5
125	2007025105917.6	22.560	121.930	36	6.0
126	2007031203134.8	-7.820	107.190	51	5.6
127	2007032001426.1	-37.650	78.070	10	5.5
128	2007035033319.4	35.340	-35.940	10	5.6
129	2007039071504.7	46.480	153.240	10	5.5
130	2007042104735.0	6.180	94.400	67	5.6
131	2007043103522.8	35.800	-10.310	20	6.2
132	2007045194958.7	0.430	97.310	16	5.7

Event number	Event name	Latitute	Longitute	Depth (km)	Magnitude (Mb)
133	2007045204631.9	0.640	97.230	4	5.6
134	2007048000256.8	41.790	143.550	31	6.0
135	2007050023343.0	1.750	30.760	19	5.6
136	2007057234953.7	-44.770	35.490	10	5.7
137	2007060000201.1	3.780	96.340	74	5.6
138	2007060231152.1	26.580	-44.590	10	6.0
139	2007063112612.0	33.790	-38.470	10	5.6
140	2007065034938.9	-0.490	100.500	19	6.4
141	2007065054925.4	-0.490	100.530	11	6.3
142	2007066105337.6	1.960	97.910	35	5.9
143	2007066230124.5	3.020	-31.820	10	5.5
144	2007067050332.3	29.910	140.200	139	6.1
145	2007068032242.8	43.220	133.530	441	6.1
146	2007068072731.2	-11.430	66.250	10	5.8
147	2007069170337.9	74.260	8.710	10	5.7
148	2007069211257.5	55.210	161.860	31	5.9
149	2007070070926.7	43.990	147.890	52	6.0
150	2007071185925.2	46.900	151.770	144	5.6
151	2007077012524.1	42.160	144.000	35	5.6
152	2007079031030.5	9.190	126.120	35	5.5
153	2007081061043.1	-3.390	86.780	21	5.9
154	2007084004157.8	37.340	136.590	8	6.8
155	2007086121359.5	48.250	154.200	30	5.5
156	2007087211710.7	-6.270	29.670	8	5.8
157	2007089090505.7	44.140	146.010	100	5.5
158	2007091025105.3	32.350	137.610	378	5.7
159	2007093033507.3	36.450	70.690	222	6.2
160	2007094195803.8	-17.230	66.790	10	5.9
161	2007094214018.8	30.930	141.670	9	5.7
162	2007095035650.5	37.310	-24.620	14	6.3
163	2007097052049.6	-39.790	46.180	10	5.9
164	2007097070925.4	37.310	-24.490	8	6.1
165	2007097095151.6	2.920	95.700	30	6.1
166	2007099101804.6	48.300	154.700	36	5.8
167	2007100135653.9	12.990	92.530	30	5.5
168	2007105041230.2	47.000	153.430	34	5.6
169	2007108150731.6	42.660	141.860	119	5.5
170	2007110002640.6	25.720	125.090	10	6.1
171	2007110003060.0	25.730	125.150	10	5.7
172	2007110014556.1	25.710	125.110	9	6.3
173	2007110022334.0	25.620	125.040	11	5.9
174	2007110052311.3	25.680	125.240	10	5.5
175	2007110193758.2	27.470	128.380	42	5.9
176	2007111003224.9	21.140	122.130	10	5.5
177	2007117080249.6	5.360	94.640	38	6.3

Event number	Event name	Latitute	Longitute	Depth (km)	Magnitude (Mb)
178	2007119124157.4	52.010	-179.970	117	6.2
179	2007124120652.2	-1.410	-14.910	10	6.2
180	2007125085139.1	34.250	81.970	9	6.0
181	2007127115947.6	31.350	97.790	12	5.6
182	2007134093143.1	1.250	97.250	30	5.5
183	2007136085616.5	20.500	100.750	23	6.4
184	2007136101745.1	48.860	154.770	10	5.5
185	2007138155958.5	41.600	141.990	58	5.5
186	2007143044146.5	52.350	-31.810	10	5.7
187	2007150202212.7	52.140	157.290	116	6.4
188	2007153213457.8	23.030	101.050	5	6.3
189	2007165144954.1	10.380	125.310	10	5.5
190	2007166184953.4	1.720	30.830	24	5.9
191	2007174081719.9	21.470	99.780	22	5.6
192	2007177222303.0	-10.490	108.150	10	6.0
193	2007182041207.8	43.660	144.730	130	5.8
194	2007184082600.8	0.710	-30.270	10	6.3
195	2007189185400.2	46.840	155.480	10	5.5
196	2007194215443.1	51.840	-176.280	35	6.0
197	2007196130800.8	52.480	-168.050	10	6.1
198	2007196132615.2	52.360	-168.010	10	5.8
199	2007197011322.4	37.530	138.450	12	6.6
200	2007197063740.4	37.500	138.470	15	5.7
201	2007197141737.3	36.810	134.850	350	6.8
202	2007198141042.5	-2.730	36.360	8	5.9
203	2007201100652.0	42.910	82.380	10	5.6
204	2007202224413.6	38.940	70.490	10	5.6
205	2007204134002.2	23.670	121.630	40	5.6
206	2007206233731.5	7.160	92.520	15	6.1
207	2007210045436.7	53.640	169.700	25	6.0
208	2007211224205.6	19.310	95.610	14	6.0
209	2007212150735.3	27.340	126.900	10	5.9
210	2007212225531.1	-0.160	-17.800	11	6.2
211	2007213081600.2	33.900	136.610	370	5.5
212	2007214023742.4	47.120	141.800	5	6.2
213	2007214032142.8	51.310	-179.970	21	6.7
214	2007214052217.7	46.710	141.720	10	5.8
215	2007214103731.6	46.630	141.770	10	5.5
216	2007214133729.2	12.510	47.460	10	5.7
217	2007219000224.2	27.290	126.840	18	5.9
218	2007220170457.8	-5.930	107.680	291	6.1
219	2007220170504.9	-5.860	107.420	280	7.5
220	2007221005552.3	22.580	121.100	21	5.7
221	2007221172505.2	25.920	-45.000	10	5.6
222	2007225222304.5	-30.990	-13.410	10	5.5

Event number	Event name	Latitute	Longitute	Depth (km)	Magnitude (Mb)
223	2007226041334.4	46.880	141.750	10	5.5
224	2007227202211.1	50.320	-177.550	9	6.4
225	2007228040303.5	50.240	-177.570	14	5.8
226	2007228141824.6	-3.520	-12.150	10	5.5
227	2007232123706.7	-0.260	-18.170	10	5.7
228	2007232224229.2	8.040	-39.250	10	6.5
229	2007240011604.6	49.690	154.290	115	5.6
230	2007241030018.0	21.780	121.430	24	5.7
231	2007246161453.6	45.840	150.060	94	6.3
232	2007249175126.2	24.340	122.220	53	6.2
233	2007255111026.8	-4.440	101.370	34	8.5
234	2007255114001.8	-2.840	100.220	35	5.5
235	2007255130207.4	-2.930	101.380	35	5.6
236	2007255144005.7	-3.160	101.460	35	5.9
237	2007255163703.9	-3.140	101.400	35	5.8
238	2007255234903.7	-2.620	100.840	35	8.1
239	2007256012634.4	-1.900	99.820	16	5.7
240	2007256023003.3	-1.690	99.670	28	5.9
241	2007256033528.7	-2.130	99.630	22	7.2
242	2007256052323.2	-1.720	99.640	32	5.5
243	2007256131014.4	-2.750	100.970	17	5.5
244	2007256150854.7	-4.300	101.270	24	5.5
245	2007256160916.4	-3.160	101.530	48	6.1
246	2007256165924.9	-2.230	99.950	30	5.5
247	2007257010205.3	-3.780	101.830	26	5.7
248	2007257060132.3	-4.070	101.170	23	6.3
249	2007257060316.5	-4.420	100.950	25	5.8
250	2007258144529.2	-2.790	101.190	35	5.6
251	2007259113744.0	-2.830	101.200	35	5.5
252	2007261084132.8	-3.260	101.350	35	5.6
253	2007262072750.7	-2.750	100.890	35	6.0
254	2007263083114.5	-2.000	100.140	30	6.8
255	2007266141343.9	-2.130	99.930	28	5.5
256	2007267081527.7	-3.160	100.380	35	5.6
257	2007267122631.0	-4.390	101.460	35	5.5
258	2007268082704.5	-1.770	100.460	35	5.5
259	2007269154301.4	-1.790	99.490	26	6.1
260	2007269183934.8	-7.070	-11.710	10	5.6
261	2007272053244.2	2.920	95.540	35	5.7
262	2007272053707.3	2.900	95.520	35	5.8
263	2007275034340.3	-4.240	101.220	31	5.9
264	2007275180006.9	54.510	-161.710	32	6.3
265	2007275180355.0	54.420	-161.700	47	5.6
266	2007277124031.1	2.540	92.900	35	6.2
267	2007281171037.9	43.540	146.740	63	5.8

Event number	Event name	Latitute	Longitute	Depth (km)	Magnitude (Mb)
268	2007283001916.8	-1.740	99.480	27	6.0
269	2007285003132.2	-3.250	100.530	35	5.6
270	2007291161314.1	30.130	-42.590	10	5.7
271	2007292071954.8	28.650	66.290	35	5.5
272	2007294142420.1	-3.590	100.800	35	5.5
273	2007294162535.0	-3.590	100.860	27	5.6
274	2007296195647.4	-2.000	99.900	30	5.8
275	2007297210250.5	-3.900	101.020	20	6.9
276	2007298052533.6	-3.540	100.790	29	5.5
277	2007298135002.6	46.010	154.230	10	6.1
278	2007299152330.0	54.520	-161.710	43	5.5
279	2007304134419.8	51.420	-178.380	28	6.0
280	2007326103856.6	51.170	-179.790	46	5.6
281	2007326230213.0	4.740	95.060	49	5.9
282	2007329025157.2	-2.810	101.160	55	6.0
283	2007329135347.9	29.670	69.540	39	5.8
284	2007329174137.9	-2.230	100.380	30	6.0
285	2007330135139.5	37.380	141.590	39	5.9
286	2007331042700.6	16.090	119.850	52	5.9
287	2007331101349.7	-1.350	-13.270	10	5.7
288	2007333190019.4	14.970	-61.240	146	7.4
289	2007335014431.9	1.990	97.900	44	5.9
290	2007340171203.2	22.690	-45.100	10	5.8
291	2007340214347.3	12.280	125.430	38	5.9
292	2007341004736.6	29.920	141.040	74	5.9
293	2007342195520.2	-7.520	37.550	10	5.6
294	2007346234000.3	52.190	-131.410	10	5.7
295	2007353093030.8	51.460	-179.470	56	7.1
296	2007353102435.3	51.500	-179.490	39	5.5
297	2007355072337.1	51.290	-178.950	41	5.9
298	2007355072435.6	51.350	-178.980	35	6.1
299	2007356122618.8	2.100	96.840	32	5.8

REFERENCES

Alcicek, M.C., J.H. Ten Veen, and M. Ozkul, 2006, "Neotectonic development of the Cameli basin, southwestern Anatolia, Turkey". In: Robertson, A.,Mountrakis, D., Brun, J.-P. (Eds.), "Tectonic Development of the Eastern Mediterranean Region", vol. 260. *Geophysical society special publication,* pp. 591–611.

Al-Lazki, I. A., E. Sandvol, D. Seber, M. Barazangi, N. Turkelli, and R. Mohamad, 2004, "Pn tomographic imaging of mantle lid velocity and anisotrapy at the junction of the Arabian, Eurasian and African plates". *Geophys J. Int.* (2004) 158, 1024-1040.

Ammon, C.J., G.E. Randall, and G. Zandt, 1990, "On the non-uniqueness of receiver function inversions", *J. Geophys. Res.,* 95, 15,303–15,318.

Ammon, C.J., 1991, "The isolation of Receiver Effects from Teleseismic P Waveforms", *Bull. Seism. Soc. Am*., 81, 2504-2510.

Ammon, C.J., and G. Zandt., 1993, "Receiver Structure beneath the Southern Mojave Block, California", *Bull. Seism. Soc. Am.* 83, 737-755.

Ammon, C.J., "http://eqseis.geosc.psu.edu/~cammon/HTML/RftnDocs/seq01 .html"

Barka, A., and R. Reilinger, 1997, "Active tectonics of the eastern Mediterranean region: deduced from GPS, neotectonic and seismicity data", *Annalli di Geofisica,* 40, 587-610.

Bijwaard, H., W. Spakman, and E. R. Engdahl, 1998, "Closing the gap between regional and global travel time tomography", *J. Geophys. Res.* 103, 30055.

Burdick, L.J., and C.A. Langston, 1977, "Modelling crust-structure through the use of converted phases in teleseismic body-wave-forms", *Bull. Seism. Soc. Am.* 67, 677-691.

Cassidy, J. F., 1992, "Numerical experiments in broadband receiver function analysis", *Bull. Seismol. Soc. Am.,* 82, 1453– 1474.

Cemen, I., M.C. Goncuoglu, and K. Dirik, 1999, "Structural evolution of the Tuzgolu Basin in central Anatolia, Turkey". *Journal of Geology* 107, 693–706.

Davies, J.H., and F. Von Blanckenburg, 1995, "Slab break off a model of lithosphere detachment and its test in the magmatism and deformation of collisional orogens". *Earth and Planetary Science Letters* 129, 85–102.

DeMets, C., R.G. Gordon, D.F. Argus, and S. Stein, 1990, "Current plate motions", *Geophy. J. Int.,* 101, 425-478.

DeMets, C., R.G. Gordon, D.F. Argus, and S. Stein, 1994, "Effects of recent revisions to the geomagnetic reversal time scale on estimates of current plate motions", *Geophy. Res. Lett.,* 21, 2191-2194.

Dey-Sarkar, S.K., and, R.A. Wiggins, 1976b, "Source deconvolution of teleseismic P wave arrivals between 14° and 40°", *J. Geophys. Res*., 81, 3633-3641.

Dugda, M. T., A Andrew, A. Nyblade, and J. Julia, 2007, "Thin lithosphere beneath the Ethopian plateu revealed by a joint inversion of rayleigh wave group velocities and receiver functions", *J. Geophys. Res*., 112, B08305, doi: 10.1029/2006JB004918.

Eaton, D, W., S. Dineva, and R. Mereu, 2006, "Crustal thickness and Vp/Vs variations in the Grenville orogen (Ontario, Canada) from analysis of teleseismic receiver functions", *Tectonophysics,* 420 (2006) 223–238.

Erduran M., Ö. Çakır, T. Tezel, Ş. Şahin, and Ö. Alptekin, 2007, "Anatolian surface wave evaluated at GEOFON Station ISP Isparta, Turkey", *Tectonophysics,* 434 (2007) 39–54i

Glover, C.P., and A.H.F. Robertson, 1998, "Neotectonic intersection of the Aegean and Cyprus tectonic arcs: extensional and strike-slip faulting in the Isparta Angle, SW Turkey". *Tectonophysics* 298, 103–132.

Gök, R., N. Türkelli, , E. Sandvol, D. Seber, and M. Barazangi, 2000, "Regional wave propagation in Turkey and surrounding regions", *Geophys. Res. Lett.* 27, 429–432.

Gök, R., E. M. Pasyanos, and E. Zor, 2007, "Lithospheric structure of the continent-continent collision zone: eastern Turkey". *Geophys. J. Int.* (2007) doi: 10.1111/j.1365-246X.2006.03288.x.

Gök, R., H. Mahdi, H. Al-Shukri, and A. J Rodgers., 2007, "Crustal structure of Iraq from receiver functions and surface wave dispersion: implications for understanding the deformation history of the Arabian–Eurasian collision". *Geophys. J. Int.* (2007) doi: 10.1111/j.1365-246X.2007.03670.x.

Helmberger, D.V., and R.A. Wiggins, 1971, "Upper mantle structureof mid-western United States", *J. Geophys. Res*., 76, 3229-3245.

Horasan, G., L. Gülen, A. Pınar, D. Kalafat, N. Özel, S. H. Kuleli, and A. M. Işıkara, 2002., "Lithospheric structure of the Marmara and Aegean regions, western Turkey", *Bull. Seism. Soc. Am.,*92, 322-329.

Jackson. D.D., 1972, "Interpretation of inaccurate, insufficient and inconsistent data", *Geophys. J. R. astr. Soc.,* 28, 97-109.

Julia, J., C.J. Ammon, R.B. Herrmann, and A.M. Correig, 2000, "Joint inversion of receiver functions and surface-wave dispersion observations", *Geophys, J. Int.,* 143, 99–112.

Julia, J., and J. Mejia, 2004, "Thickness and Vp/Vs ratio variation in the Iberian crust", *Geophys. J. Int.,* 156, 59– 72.

Julia, J., C.J. Ammon, and R.B. Herrmann, 2003, "Lithospheric structure of the Arabian Shield from the joint inversion of receiver functions and surface wave group velocities", *Tectonophysics,* 371**,** 1–21.

Julia,J., C. J. Ammon, and A. A. Nyblade, 2005, "Evidence for mafic lower crust in Tanzania, East Africa, from joint inversion of receiver functions and Rayleigh wave dispersion velocities", *Geophys. J. Int.* (2005) 162**,** 555–569.

Kalafat, D., C. Gürbüz, and B. Üçer, 1987, "Batı Türkiye' de Kabuk ve Üst Manto yapısının araştırılması", *DAEB*, 59, 43-64.

Kalyoncuoğlu, Ü.Y., and M.F. Özer, 2003, "Determination of the crustal structure beneath the Isparta seismograph station". *Dokuz Eylül University. Bull. Sci. Eng.* 5, 111–127.

Karagianni, E.E., C.B. Papazachos, D.G. Panagiotopoulos, P. Suhadolc, , A. Vuan, G.F Panza, 2005, "Shear velocity structure in the Aegean area obtained by inversion of Rayleigh waves". *Geophys. J. Int.* 160, 127–143.

Kempler, D., and Z. Ben-Avraham, 1987, "The tectonic evoluation of the Cyprean arc", *Annales Tectonicae,* 1, 51-71.

Langston, C.A., 1979, "Structure under Mount Rainier,Washington, inferred from teleseismic body waves", *J. Geophys. Res.,* 84, 4749–4762.

Le Pichon, X., and J. Angelier, 1979, "The Hellenic Arc and Trench System: A Key to the Neotectonic Evolution of the Eastern Mediterranean Area", *Tectonophysics*, Vol. 60, pp. 1-42.

Le Pichon, X., and J. Angelier, 1981, "The Aegean sea", *Philos, Trans, R. Soc. London, Ser. A,* 300, 357-372.

Li, X., Kind, R., X. Yuan, I. Wölbern, and W. Hanka, 2004, "Rejuvenation of the lithosphere by the Hawaiian plume", *Nature,* 427, 827– 829.

Liggoria, J.P., 2000, "*An investigation of the mantle crust transition beneath North Amerial and Poisson's ratio of the North Ameriacan crust*", PhD, Thesis, p. 261, Saint Louis Univ., Saint Louis.

Liggoria, J.P., and C.J. Ammon, 1999, "Iterative deconvolution and receiver function estimation", *Bull. Seism. Soc. Am.,* 89, 1395– 1400.

McKenzie, D. P., "Active tectonics of the Mediterranean region", *Geophy. J. Roy. Astr. Soc.,* 30, 109-185, 1972

McKenzie, D. P., 1978, "Active Tectonics of the Alpine-Himalayan Belt: the Aegean Sea and Surrounding Regions", *Geophy. J. Roy. Astr. Soc.*, Vol.55, pp. 217-254.

Menke, W., 1984, "*Geophysical Data Analysis: Discrete Inverse Theory",* Academic Press, Orlando.

Mohorovičić, A., 1910a, Potres od 8. X 1909. "Godišnje izvješće Zagrebačkog meteorološkog opservatorija za godinu" 1909. 9/4, 1–56.

Nyst, M., and W. Thatcher, 2004, "New Constraints on the Active Tectonic Deformation of the Aegean", *J. Geophy. Res*, Vol.109, pp. 163 196.

Owens, T.J., G. Zandt, and S.R. Taylor, 1984, "Seismic evidence for an ancient rift beneath the Cumberland Plateau, Tennessee: A detailed analysis of broadband teleseismic P waveforms", *J. Geophys. Res.* 89, 7783-7795.

Özakın, Y., 2008, *Crustal structure of southwestern Anatolia using P wave receiver function,* M.S. Thesis, Boğaziçi University.

Özalaybey, S., M. K. Savage, A. F. Sheehan, J. N. Louie, and J. N. Brune, 1997, "Shear-wave velocity structure in the northern Basin and Range Province from the combined analysis of receiver functions and surface waves", *Bull. Seism. Soc. Am.*, 87, 183–199.

Pasyanos, M.E., 2005, "A variable resolution surface wave dispersion study of Eurasia, North Africa, and surrounding regions", *J. Geophys. Res.,* 110, B12301, doi:10.1029/2005JB003749.

Phinney, R. A., 1964, "Structure of earths crust from spectral behavior of long-period body waves", *J. Geophys. Res.,* 69, 2997-3017.

Piromallo C., and A. Morelli, 1997, "Imaging the Mediterranean upper mantle by P-wave travel time tomography", *Ann. Geof.,* 40, 963-979, 1997.

Royden, L., 1993, "Evoluation of retreating subduction boundaries formed during continental collision", *Tectonic*s, 12, 303-325.

Sandvol, E., K. Al-Damegh, A. Calvert, D. Seber, M. Barazangi, R. Mohamad, R. Gok, N. Turkelli, and C. Gurbuz, 2001, "Tomographic Imaging of Lg and Sn Propagation in the Middle East". *Pure and Applied Geophysics* 158, 1121–1163.

Sandvol, E., N. Turkelli, E. Zor, R. Gok, T. Bekler, C. Gurbuz, D. Seber, and M. Barazangi, 2003, "Shear wave splitting in a young continent-continent collision: an example from Eastern Turkey". *Geophy. Res. Let.* 30, No. 24, 8041.

Sato, H., I.S Sacks, and T. Murase, 1989. "The use of laboratory data for estimating temperature and partial melt fraction in the low velocity zone: Comparison with heat flow and electrical conductivity studies", *J. Geophys. Res.,* 94, 5689-5704.

Scherbaum, F., and J. Johnson, 1992, **"**Programmable Interactive Toolbox for Seismological Analysis. IASPEI Software Library", Vol. 5, *Bull. Seism. Soc. Am.*, El Cerrito, CA, 269 pp., and 2 diskettes.

Yelkenci, S., 2006, *The crustal structure of the central Anatolia using receiver function analysis,* M.S. Thesis, Boğaziçi University.

Sodoudi, F., R. D. Kind, , K. Hatzfeld, W. Priestley, K. Hanka, G. Wylegalla, A. Stavrakakis, H. Vafidis, P. Harjes and M. Bohnhoff, 2006, "Lithospheric Structure of the Aegean Obtained from P and S Receiver Functions"*, Jour. Geophy. Res*, Vol.111, pp. 504-527.

Tarantola, A., 1987, "Inverse Problem Theory. Methods for Data Fitting and Model Parameter Estimation"*, Elseiver,* Amsterdam.

Wessel, P., and W.H.F. Smith, 1998, "New Improved Version of the Generic Mapping Tools Released", *EOS Trans. AGU* 79, pp. 579.

Wiggins, R.A., 1972, "The general linear inverse problem: implication of surface waves and free oscillations for earth structure", *Rev. Geophys. Space. Phys.,* 10, 251-285.

Wortel, M.J.R., and W. Spakman, 1992, "Structure and dynamics of subducted lithosphere in the Mediterranean region", *Proc. K. Ned. Akad. Wet.,* 95, 325-347.

Wortel, R., W. Spakman, 2000, "Subduction and slab detachment in the Mediterranean-Carpathian region". *Science* 290, 1910–1917.

Yuan, X., 2000, "New constraints on subduction and collision processes in the Central Andes from P-to-S converted seismic phases", *Nature,* 408, 958-961.

Zandt, G., and C.J. Ammon, 1995, "Continental crust composition constrained by measurements of crustal Poisson's ratio", *Nature,* 374, 152-154.

Zandt, G., S.C. Myers, and T.C. Wallace, 1995, "Crustal and mantle structure across the Basin and Range - Colorado Plateau boundary at 37°N latitude and implications for Cenozoic extensional mechanism", *J. Geophys. Res.* 100, 10529-10548.

Zhu, L., 1993, "Estimation of crustal thickness and Vp/Vs ratio beneath the Tibetan Plateau from teleseismic converted waves (abstract.)", *Eos Trans. AGU,* 74(16), Spring Meet. Suppl., 202.

Zhu, H., and H. Kanamori, 2000, "Moho depth variation in southern California from teleseismic receiver functions", *J. Geophys. Res.* 105, 2969-2980.

Zhu, L., B.J. Mitchell, N. Akyol, I. Cemen, and K. Kekovali, 2006, "Crustal thickness variations in the Aegean region and implications for the extension of continental crust", *J. Geophys. Res.,* 111, B01301, doi: 10.1029/2005JB003770.

Zor, E., 2002, *The shear wave velocity structure of the eastern Marmara Region by using receiver function analysis,* Ph.D. Thesis, Boğaziçi University.